

# SolarDynamics

## Final Technical Report

Drop C: The Drop-In, Ring-of-Power Heliostat



Prepared by:

Solar Dynamics, L.L.C. 1105 W. 11<sup>th</sup> Ct., Broomfield, CO, USA 80020

©2023 Solar Dynamics, LLC. The contents of this document and any equipment and/or software described may be protected by patents pending in the United States and other countries.

**Project Title:** Drop C: The Drop-In, Ring-of-Power Heliostat

**Project Period:** 10/01/2017 – 02/28/2022

**Submission Date:** 05/17/2023

**Recipient:** Solar Dynamics LLC

**Address:** 1105 W. 11<sup>th</sup> Ct.  
Broomfield, CO 80020

**Website:** [www.solardynllc.com](http://www.solardynllc.com)

**Award Number:** DE-EE0008024

**Project Team:** Solar Dynamics LLC

**Principal Investigator:** Kyle Kattke, Senior Engineer  
Email: [kyle.kattke@solardynllc.com](mailto:kyle.kattke@solardynllc.com)

**Business Contact:** Hank Price, Managing Director  
Email: [hank.price@solardynllc.com](mailto:hank.price@solardynllc.com)

**Technology Manager:** Matthew Bauer

**Project Officer:** Christine Bing

**Grant Specialist:** Stephanie Hodge

**Contracting Officer:** Diana Bobo

## Acknowledgement

This material is based upon work supported by the U.S. Department of Energy's Office of Energy Efficiency and Renewable Energy (EERE) under the Solar Energy Technology Office (SETO), Collects: Concentrating Optics for Lower Levelized Energy Costs award number DE-EE0008024.

## Disclaimer

This report was prepared as an account of work sponsored by an agency of the United States Government. Neither the United States Government nor any agency thereof, nor any of its employees, makes any warranty, express or implied, or assumes any legal liability or responsibility for the accuracy, completeness, or usefulness of any information, apparatus, product, or process disclosed, or represents that its use would not infringe privately owned rights. Reference herein to any specific commercial product, process, or service by trade name, trademark, manufacturer, or otherwise does not necessarily constitute or imply its endorsement, recommendation, or favoring by the United States Government or any agency thereof. The views and opinions of authors expressed herein do not necessarily state or reflect those of the United States Government or any agency thereof.

## Executive Summary

This report summarizes the work performed within the Drop-C: The Drop-In, Ring-of-Power Heliostat project. The Drop-C project aimed to develop a novel heliostat with an installed cost of \$50/m<sup>2</sup> (\$<sub>2015</sub>) which is a drastic cost reduction compared to the state-of-the-art. The resulting 27m<sup>2</sup> SunRing™ heliostat's relatively small size necessitates the parallel development of a wireless solar field network and a rapid calibration system. The SunRing heliostat is an evolution of the Ring-of-Power (ROP) design from Abengoa Solar LLC [5] which had a reported installed cost of \$114/m<sup>2</sup>. Cost savings relative to the ROP were sought by increasing the mirror area, improving the structural efficiency, a more accurate assessment of wind loads, and an improved assembly and installation procedure.

The project spanned three Budget Periods (BP) where a digital heliostat was developed in BP1 using wind tunnel testing to define load conditions. After component testing early in BP2 of the original friction azimuth drive, the azimuth drive design was pivoted to a geared azimuth drive design. The SunRing's geared azimuth drive is its most novel feature thus requiring robust testing. Lifetime test chambers were built in both BP2 and BP3 with a segment of the azimuth drive track to test wear and positional accuracy. In BP2, dust was circulated in the chamber to represent a worst-case outdoor environment, and in BP3 a clean chamber was used to isolate failure modes. A full 30-years of equivalent heliostat life was never achieved. Testing was stopped prematurely due to failures in the gearmotor to pinion coupling and failures in the pinion roller's plain bearings in BP2 and BP3, respectively. A commercial design change has been identified to remedy the bearing failures. Additional lifetime testing occurred on the elevation drive's linear actuator with 17 years of equivalent life accumulated before the actuator was used on the heliostat prototypes. Additionally, lifetime battery testing has led to selecting the Lithium Iron Phosphate (LiFePO<sub>4</sub>) chemistry with an estimated lifetime of 9.3 years on the heliostat.

Two full scale heliostat prototypes were built at the SolarTAC test facility in BP2. The first underwent structural load testing with no signs of failure. The second prototype was optically characterized indoors with close range photogrammetry measurements followed by outdoor tracking testing. Following calibration, the 2<sup>nd</sup> prototype surpassed tracking accuracy targets with 0.67 mrad (slope basis). A third full scale prototype was built in BP3 with design changes addressing the BP2 heliostats' poor optical performance due to overall facet rotations. However, mirror slope error remains higher than predicted with potential sources and remedies identified. This testing provided further merit to the predicted SunRing installed cost of \$96.3/m<sup>2</sup> (\$<sub>2019</sub>).

The solar field's wireless mesh network technology was field-tested with a 30-node network test within a heliostat field which defined the maximum 1-hop range. This was followed by a large 489-node network where measuring overall latency from a simulated emergency stow command was the main goal. The time required to broadcast the message and receive acknowledgement from all nodes was less than 48 sec, which is sufficient as a molten salt receiver's inlet vessel is typically sized to provide 60 sec of flow upon pump failure. Other testing showed the mesh network's ability to co-exist with

other 2.4 GHz networks, and a simulated LII controller failure led to a more robust LII layout design.

Lastly, the Rapid Calibration System (RCS) was developed initially with an analytical ray casting model. A set of four cameras surround the receiver looking back at the solar field. Based on the circumsolar radiation seen in each camera from a particular heliostat, a centroid algorithm calculates the heliostat image's centroid. The original algorithm was bench scale tested in BP1 and BP2 with accuracy of 2.0 mrad, far from the goal of 0.5 mrad. A new approach developed in BP3 yielded accuracy of 0.54 mrad and is a viable commercial pathway for the RCS.

## Table of Contents

Acknowledgement .....	3
Disclaimer .....	3
Executive Summary .....	4
Background .....	8
Project Objectives .....	8
Project Results and Discussion .....	9
1 SunRing Heliostat (Tasks 1,4, and 7) .....	10
1.1 Reference Tower Plant .....	14
1.2 Specifications .....	14
1.3 Overall Design Down Selection .....	18
1.4 Wind Tunnel Testing .....	20
1.5 FEA Analysis – methodology .....	22
1.6 Azimuth Drive Evolution .....	24
1.7 Foundation Evolution .....	31
1.8 Final Design .....	33
1.9 Assembly and Field Installation .....	45
1.10 Commercial Outreach .....	49
1.11 Azimuth Drive Lifetime Testing .....	52
1.12 Elevation Drive Lifetime Testing .....	58
1.13 Battery Testing .....	60
1.14 Full Scale Prototype Testing .....	61
2 Solar Field Communication and Control (Tasks 2,5, and 8) .....	75
2.1 Overall Architecture Introduction .....	77
2.2 Heliostat Local Controller .....	79
2.3 Wireless Mesh Network (L2-L3 communication) .....	80
2.4 FMEA of Solar Field Communication Network .....	88
2.5 Detailed Solar Field Communication Design .....	89
3 Rapid Calibration System (Tasks 3, 6, and 9) .....	95
3.1 Analytical Model .....	95
3.2 RCS overall design .....	95
3.3 Bench scale testing .....	97

3.4 Commercialization.....	98
Significant Accomplishments and Conclusions .....	99
Inventions, Patents, Publications, and Other Results.....	99
Path Forward.....	99
References.....	100

## Background

The heliostat field in a power tower Concentrating Solar Power (CSP) plant represents up to 40-50% of the installed plant cost. Thus, heliostat cost reductions are key to CSP becoming cost competitive. Recent commercial heliostats (i.e. deployment history at utility scale projects) are estimated to have an installed cost of \$120-140/m<sup>2</sup> with a relatively mature design resulting from 2-3 commercial scale deployments. Thus, it is unlikely to meet the SunShot programmatic goal of \$50/m<sup>2</sup> with evolutionary improvements to the status quo. The main commonality with all commercial heliostats is the use of a pedestal mount. Pedestal mounts support the mirror structure at a single location central to the mirrors and provide a single load path to the ground through the pedestal.

Pfahl [2] provides a comprehensive summary of heliostat designs: commercial heliostats deployed at utility scale, pre-commercial designs deployed at small scale demonstration solar fields, and heliostat R&D concepts. Most of the next-generation R&D concepts move away from the pedestal mount utilizing a ganged support structure, unique tracking axes, and/or novel actuators. Of the concepts presented, the lowest cost target design (\$80/m<sup>2</sup>) is a carousel heliostat in development by Pfahl [3] at DLR. This carousel heliostat shares similarities with the SunRing.

A wireless communication network is critical to making relatively small heliostats cost competitive. Mesh networks have been proposed by others for heliostat fields [18] and tested at experimental scale [4]. BrightSource's Ashalim project is the first utility scale heliostat field utilizing a wireless network, but the technology used is not public knowledge.

All commercial heliostat calibration systems to date utilize the traditional Beam Characterization System (BCS). In this BCS, individual heliostats move their image onto a target, and cameras in the field image the target to calculate the centroid. This is a slow process, requiring long commissioning periods and that heliostats maintain their accuracy between calibrations. The use of multiple look back cameras surrounding the receiver to image the solar field was first introduced by Kribus [1]. BrightSource presented a similar method with cameras imbedded within a central receiver [15]. Collins [14] has developed a grid of look back cameras on a target to calibrate multiple heliostats simultaneously. Lastly, Heliogen reported using look back cameras for closed loop control of its' heliostats. These developments provide confidence to the look back camera approach taken in the Drop-C project.

## Project Objectives

The final objectives of the project are to complete the pilot-scale system validation testing of a 27m<sup>2</sup> highly cost-efficient heliostat fulfilling the SunShot "disruptive off-map" solution criteria, along with advanced wireless control and rapid calibration technologies that will differentiate the heliostat product and improve its market appeal. The project has 3 x Key Performance Indicators (KPI) each covering a major thrust of the project, as



shown in Table 1. Each task’s milestones and final deliverables are presented in the Project Results and Discussion section below.

*Table 1 Key Performance Indicators*

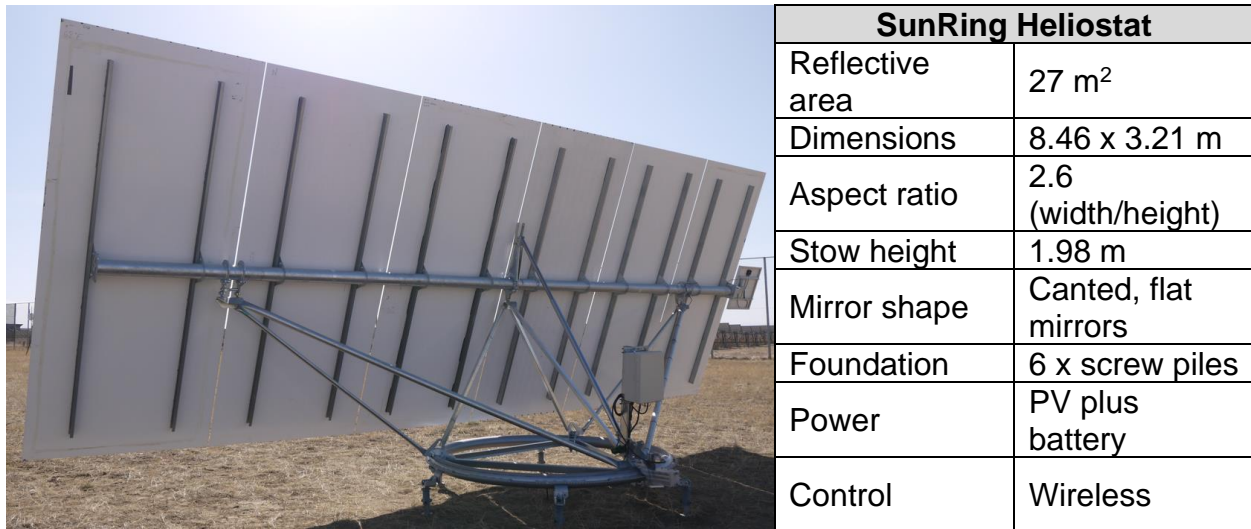
KPI-1 <i>heliostat</i>	<ul style="list-style-type: none"> <li>• \$50/m<sup>2</sup> installed cost</li> <li>• 4mrad calm / 5mrad windy optical beam RMS error</li> <li>• 35mph operational wind speed / 94 mph survivable wind speed</li> <li>• ≥ 30-year lifetime</li> </ul>
KPI-2 <i>solar field communication network</i>	<ul style="list-style-type: none"> <li>• command response of 90% of all controllers within ≤10s and all controllers within ≤30s</li> <li>• ability to wirelessly update controller parameters and firmware</li> <li>• wireless controller cost ≤\$150/unit</li> <li>• security fail-safes disallow unintended damage</li> </ul>
KPI-3 <i>Rapid Calibration System</i>	<ul style="list-style-type: none"> <li>• ≤ 0.5mrad error detection sensitivity</li> <li>• calibration rate ≥1000 heliostats/day</li> <li>• operable within required solar field layouts and heliostat orientations</li> <li>• validated to be compatible with surround-type receivers</li> </ul>

## Project Results and Discussion

The following details the project’s outcomes broken down into the three main thrusts: heliostat, solar field communication network, and rapid calibration system.

## 1 SunRing Heliostat (Tasks 1,4, and 7)

The SunRing™ heliostat was developed over the project’s three budget periods. Budget period 1 (BP1) focused on concept down-selection to arrive at a final digital prototype. A wind tunnel study was performed to define the governing wind loads used to size all structural members and drives. The 2<sup>nd</sup> budget period (BP2) focused on demonstrating the heliostat through both component level and full-scale SunRing prototype testing. Lessons learned from BP2 were used to update the design in budget period 3 (BP3) culminating in a final prototype SunRing. Figure 1 provides a high-level summary of the SunRing heliostat as a contextual reference for the following sections.



*Figure 1 Final SunRing outdoor prototype and key metrics*

Progress made toward achieving the heliostat milestones and final deliverables are presented in Table 2 through Table 6 below.

*Table 2 Budget Period 1 Milestones*

Milestone Number and Title	Metric	Success Value	Measured Value	Support Data
<b>M (ST-1.3)</b> Assembly cost reduction resulting from modular manufacturing concepts	$Cost_{\text{Assembly Infrastructure}} + Cost_{\text{Assembly Labor}}$	≤\$124 per heliostat @ 68% confidence	\$204 per heliostat (BP1) \$264 per heliostat (BP3)	Page 49
<b>M (ST-1.4)</b> Wind load reduction resulting from wind mitigation study	Absolute value, pitching moment about elevation axis $ M_{\text{elevation}} $	Success 20% / Reach 36% reduction relative to ROP design value, scaled to larger SunRing facet array	36% due to high speed stow plus interior heliostat load reduction	BP1 go/no-go report

*Table 3 Budget Period 2 Milestones*

Milestone Number and Title	Metric	Success Value	Measured Value	Support Data
<b>M (ST-4.1)</b> System Benefit with Advanced Receivers	System benefit: required adjustment in total heliostat cost (\$/m <sup>2</sup> ) required to equalize the LCOE of two different systems.	<b>Binary: Pass / Fail</b> <b>Constraint:</b> System benefit calculated for (focused and canted) and (flat and canted) SunRing variations as compared to baseline (flat and no-canting) for both cavity and surround Gen-3 receivers.	Not completed.	BP2 go/no-go report
<b>M (ST-4.3)</b> Civil Engineering Critical Review of Ballast Foundation	Foundation displacement in response to environmental loading sufficient for 30 year operation	<b>Binary: Pass / Fail</b> <b>Constraint:</b> For typical soil types found at CSP projects, quantify displacement and frequency of movement.	Pass	Page 31
<b>M (ST-4.5)</b> Feedback from commercial outreach	Receipt of commercial outreach feedback	≥ 3 commercial outreach survey forms completed by CSP developers	Merged with T2M milestone	Page 49
<b>M (ST-4.7.1)</b> Quantify ballast foundation resistance to overturning and sliding	static coefficient of friction and overturning moment required to lift foundation edge	KPI remain unchanged with updated measurement inputs.	NA with change to pile foundation.	NA
<b>M (ST-4.7.2)</b> Quantify ballast foundation movement in response to peak wind loads.	Relative displacement/rotation of the foundation	KPI remain unchanged with updated measurement inputs.	NA with change to pile foundation.	NA

*Table 4 Budget Period 2 Milestones continued*

Milestone Number and Title	Metric	Success Value	Measured Value	Support Data
<b>M (ST-4.7.3)</b> Azimuth drive lifetime assessment	Equivalent heliostat operating years	<b>&gt;= 30 years</b> or replacement cost within KPI metrics	-Geared track 6.5 years with no wear signs. -Drive pinion at 0.5 years with no pinion wear signs, but roller's plain bearings failed shutting down test, commercial design change identified.	Page 52
<b>M (ST-4.7.4)</b> Azimuth Drive Effect of Track Debris	Does debris interfere with azimuth drive operation.	<b>Binary</b> Heliostat is able to continue azimuth rotation in the presence of debris on the track.	- No issues with heliostat prototypes. - Larger debris testing TBD after project ends.	None
<b>M (ST-4.7.5)</b> Verify Azimuth Tracking and Misalignment Parameter Algorithm	Accuracy of azimuth drive. Accuracy = measured azimuth position - target azimuth position	Measured value $\leq 0.5$ mrad (relates to slope error at heliostat)	0.17 mrad using azimuth accuracy test fixture on heliostat in BP3	Page 40
<b>M (ST-4.7.6)</b> Elevation drive lifetime assessment	Backlash as f(operating years). AND Equivalent heliostat operating years until failure.	<b>Backlash:</b> KPI remain unchanged with updated measurement inputs. <b>Lifetime:</b> $\geq 30$ year lifetime or replacement cost within KPI metrics	Tested to 17 years of life with 0.023 inches average backlash which is acceptable. Testing unable to reach 30 years due to procurement delays in BP3.	Page 58
<b>M (ST-4.7.7)</b> Measure Facet Shape Error with Temperature Fluctuations	RMS slope error	Measured value $\leq 0.5$ mrad (relates to slope error at heliostat)	0.2 mrad from indoor PG testing on BP2 heliostat	Page 65
<b>M (ST-4.7.8)</b> Quantify Battery Lifetime	Capacity loss per operational year	KPI remain unchanged with updated measurement inputs.	9.3 year battery life with 2X replacements included in cost model	Page 60
<b>M (ST-4.9)</b> Advanced Drop-C Design and Cost Reduction Opportunities	Installed Cost Relative to the Baseline Drop-C	$\geq \$10/m^2$	Conceptual \$11.93/m <sup>2</sup> savings estimated in BP2	BP2 go/no-go report

- Note: purple shaded milestones were carried over into BP3

*Table 5 Budget Period 3 Milestones and Final Deliverables*

Milestone Number and Title	Metric	Success Value	Measured Value	Support Data
<b>M (ST-7.1)</b> Validate azimuth drive positional accuracy	Positional accuracy	$\leq 0.75$ mrad @ 68% confidence when sampled at increments no greater than $1^\circ$ along entire $360^\circ$ track	Not explicitly tested, but pin-to-pin error = 0.17mrad. And, heliostat tracking performance adds assurance to azimuth drive accuracy.	Page 40 & Page 72
<b>M (ST-7.2)</b> Validate canting accuracy	Canting error at $0^\circ$ elevation angle.	$\leq 0.5$ mrad (slope error basis)	0.14 mrad	Page 63
<b>FD-1</b> Product Documentation Package	Installed cost, per FOA defined categories	$\leq \$50/m^2$ @ 68% confidence	$\$96.3/m^2$	Page 44
	Optical error calm / windy	$\leq 4$ mrad / $\leq 5$ mrad  @ 68% confidence from 20 or more consecutive full testing days	3.3 / 3.8 – w/ FEA structural deflection  5.0 / 7.9 – w/ measured structural deflection	Page 45
	Max Wind Speed Operation / Survival	$\geq 35$ mph / $\geq 94$ mph	35mph / 94mph	Page 62
	Lifetime	$\geq 30$ years	30 year design	Page 40
<b>FD-2</b> Industrial Advisory Board review of Product Documentation Package	CSP industry response to:  Product Documentation Package summarizing technical status, cost, and commercial readiness testing of DROP-C project technologies	$\geq 3$ CSP developer responses AND $\geq 2$ prospective supplier responses for each critical hardware subsystem (including WMN hardware)	IAB review meeting occurred, feedback captured.	Page 51
<b>FD-3</b> Industrial Advisory Board review of Commercial Development Plan	CSP industry response to Commercial Development Plan outlining targeted next demonstration steps, potential further technological improvements, state of the market, and prospective first commercial applications			

Table 6 Tech 2 Market Milestones

Milestone Number and Title	Metric	Success Value	Measured Value	Support Data
<b>M (T2M-1)</b> Industrial Advisory Board review of Commercial Development Plan	CSP Industry Response to DROP-C	≥3 CSP developer responses AND ≥2 prospective supplier responses for each critical hardware subsystem (including WMN hardware)	Industrial Advisory Board review and email/phone confirmations from suppliers	Page 49
<b>M (T2M-2)</b> Industrial Advisory Board review of Commercial Development Plan	Heliostat, WMN, and RC System		Commercial discussions with potential investor in-leu of IAB review.	Page 50

### 1.1 Reference Tower Plant

The baseline power tower plant used in developing the SunRing is a 40,000 heliostat solar field located in the Harquahala Valley outside Phoenix, Arizona. The solar field can support a receiver with a design duty of 550 MWt. Figure 2 presents the solar field layout. Solar field construction is assumed to be completed in 11-month.

### 1.2 Specifications

Specifications were created for all major components along with the overall heliostat. The primary goal of the specifications is to clearly present functional requirements to all stake holders including Solar Dynamics team members, component vendors, and CSP project developers.

#### 1.2.1 Heliostat Specification

An overall specification for the SunRing was created defining design wind speeds, optical error budget, and operating modes. Table 7 presents the SunRing’s design wind speeds.

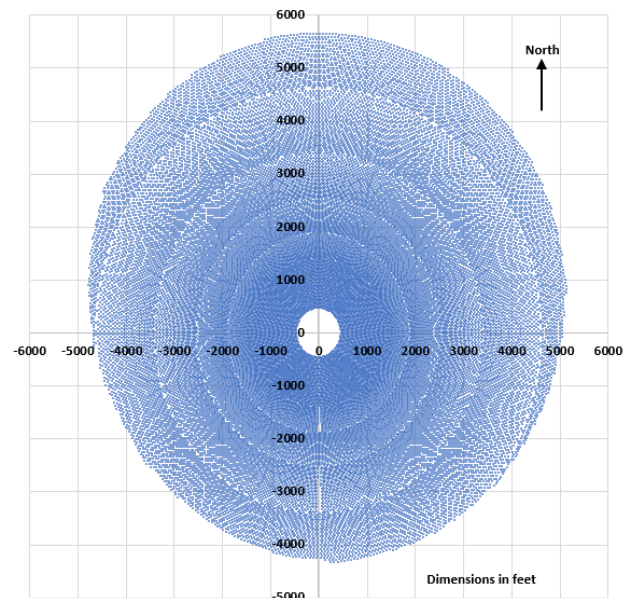


Figure 2 Baseline solar field layout

Table 7 SunRing design wind speeds

Case	Optical, calm	Optical, windy	Max tracking	Survival, any position	Survival, stow
Wind Speed <sup>1</sup>	5 m/s (11 mph)	12 m/s (27 mph)	16 m/s (35 mph)	18 m/s (40 mph)	42 m/s (94 mph) <sup>3</sup>
Optical Requirement <sup>2</sup>	≤ 4 mrad	≤ 5 mrad	None	None	None

<sup>1</sup> 3-sec gust measured at 10m above grade

<sup>2</sup> RMS total beam error, field average, using mean wind load

<sup>3</sup> ASCE 7-16: Risk Category I, Harquahala Valley Arizona site

### 1.2.2 Actuators

The SunRing rotates about an elevation and azimuth axis as shown in Figure 3. Both the elevation and azimuth actuators have two operating modes: tracking and slewing. During tracking, the heliostat operates with a move and hold strategy where 0.5 mrad (0.028°) movements are taken at the heliostat after the heliostat's image drifts 0.5 mrad from the aimpoint. During slewing, the heliostat will continuously rotate through a relatively large angle (90° in elevation and 360° in azimuth). Table 8 presents the wind load scenarios that define the actuators' load and speed requirements. Load and speed requirements during slewing ultimately drive the actuator selection. The elevation actuator is used to move to stow if a high wind alarm is triggered (gust ≥35mph); thus, it experiences the highest slewing loads with its speed governed by a 4 min stow target. The azimuth actuator requires a high slewing speed to minimize energy collection losses when the heliostat performs a large azimuth rotation to track the sun (occurs when heliostat elevation angle approaches 0°). A speed of 30°/min was found to have minimal impact on annual energy collection. The azimuth actuator's slewing wind speed was selected to ensure that the 30°/min speed could be achieved in most operating hours. Lastly, dynamic loading is defined by mean wind loads.

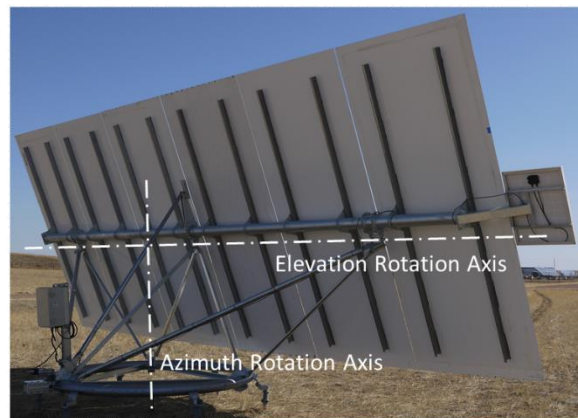


Figure 3 SunRing rotation axes

*Table 8 Actuator load and speed requirements*

	Tracking		Slewing		Static Load
	Dynamic Load	Heliostat Speed	Dynamic Load	Heliostat Speed	
Azimuth actuator	Mean wind load from 23 mph 1-hr average wind speed (equivalent to 35 mph 3-sec gust)	0.33°/min	Mean wind load at 16 mph 1-hr average wind speed (maximum from TMY)	30°/min	MAX(40 mph gust and any orientation , 94 mph gust in stow orientation) both 3-sec gusts
Elevation actuator		0.76°/min	Mean wind load from 29 mph 4-min average wind speed (equivalent to 40 mph 3-sec gust)	22.5°/min	

### 1.2.3 Elevation Actuator

Table 9 presents a condensed version of the elevation actuator specification.

*Table 9 Condensed elevation actuator specification*

	Parameter	Unit	Value
Dynamic Loading: Slewing Operation	Average Load	[lbf]	433
	Average Speed	[in/s]	0.192
	Duty Cycle	[--]	100% for 4 min
Dynamic Loading: Tracking Operation	Peak Load	[lbf]	502
	Speed	[in/s]	0.02
	Duty Cycle	[--]	25%
Static Loading	Peak Load	[lbf]	1,596
	Type	[--]	DC - brush or brushless
	Stroke Length	[in]	42-46
	Max Backlash - New/End of life	[in]	.012 / TBD
	Lifetime	[years]	30
	Lifetime - Total Travel Distance	[in]	1,037,863
	Lifetime - Equivalent # Cycles	[--]	15,338

### 1.2.4 Azimuth Drive

Table 10 presents a condensed version of the azimuth drive specification.



*Table 10 Condensed azimuth actuator specification*

Parameter		Unit	Value
Dynamic Loading: Slewing Operation	Average Torque	lbf-ft	57
	Average Speed	RPM	4.04
	Duty Cycle	[--]	100% for 12 minutes
Dynamic Loading: Tracking Operation	Torque	lbf-ft	71
	Speed	RPM	0.2
	Duty Cycle	[--]	19%
Static Loading	Peak Torque	lbf-ft	118
	Type	[--]	DC - brush or brushless
	Max Backlash	[mrad]	9.6
	Lifetime	[years]	30
	Lifetime - Total Output Shaft Rotations	[rev]	531,759

Due to the SunRing’s novel azimuth drive design, a 54:1 gear reduction is realized between the azimuth actuator output shaft and the heliostat. This allows for relatively large backlash in the azimuth actuator.

### 1.2.5 Foundation

Table 11 presents the main requirements of the pile foundations.

*Table 11 Foundation key requirements*

Parameter		Unit	Value
	Axial load capacity	[lbf]	1,677
	Lateral load capacity	[lbf]	1,675
Installation Tolerance	Height	[inch]	+/- 0.25
	Lateral location	[inch]	+/- 1
	Rotational twist	[--]	none
	Plumb	[deg]	+/- 1

### 1.2.6 Controller and Wireless Communication

The controller’s specification is presented on page 67 within the Solar Field Communication and Control section.

### 1.2.7 PV & Battery

Sizing of the battery and PV panel is dependent on multiple factors including wind loading, heliostat location, and battery chemistry to name a few. A detailed model was created to validate power sizing assumptions over many heliostat operational regimes, scenarios, and configurations. The current requirements for the PV and battery systems are presented in Table 12.

*Table 12 Battery and PV key specifications*

Parameter	Unit	Value
PV design life	[years]	30
PV size	[W]	40
Battery usable capacity	[W-hr]	62
Battery voltage	[V]	24
Battery design life	[years]	30 (may require replacements)
Environmental	[°F]	-20 to 131

### 1.2.8 Mirror Facets

Table 13 presents the main specifications for the mirror facet which were discussed with glass suppliers. The SunRing’s facet width was chosen to maximize float glass manufacturing limits. Three millimeter glass can be supplied with a 0.5% increase in reflectivity, ~\$0.70/m<sup>2</sup> drop in cost, but it is far less rigid than typical 4mm thick glass. Therefore, 4mm glass was chosen for the baseline SunRing design.

*Table 13 Mirror facet condensed specifications*

Parameter	Unit	Value
Width	[in]	55.12
Height	[in]	126.38
Thickness	[in/mm]	.16 in / 4 mm
Glass	[--]	Low iron ultra clear glass
Solar weighted reflectivity	[%]	94.5
Focal length	[ft]	NA – flat facet
Slope error	[mrad]	0.5

## 1.3 Overall Design Down Selection

The following defends the choices made to arrive at the overall SunRing design.

### 1.3.1 Size and Optical Figure

The SunRing is an evolution of the Abengoa Solar’s ROP heliostat [5]. The ROP was 18 m<sup>2</sup>, and the decision to increase the mirror area of the SunRing was driven by:

- The ROPs elevation and azimuth drives were oversized and proved to be adequate for the SunRing’s loads.
- Fixed costs relative to size including controller, assembly, installation become amortized over a larger mirror area.

The next step was to select the larger mirror area and aspect ratio. The facet size from the ROP was held constant as discussions with mirror suppliers affirmed it was near

optimum from a manufacturing standpoint. Increasing the overall mirror area can then be achieved by adding facets. Two scenarios were explored:

- 6 facets in portrait arranged in 1 row / 6 columns (Aspect ratio = 2.6)
- 6 facets in landscape arranged in 3 rows / 2 columns (Aspect ratio = 1.5)

As aspect ratio impacts heliostat field layout and overall flux profile on the receiver, a system level impact study was performed which also looked at the impacts of facet canting and focal length. Table 14 presents the results of the system benefit study where in each case the solar field was optimized for a receiver capacity of 400 MWt.

*Table 14 System benefit study of aspect ratio, focusing, and canting*

Case #	1	2	3	7	8	9	10
Aspect Ratio	2.6	2.6	2.6	1.5	1.5	1.5	1.5
Facet Shape	Flat	Flat	Focused at slant range	Flat	Flat	Flat	Focused at slant range
Facet Canting	None	Canted on-axis	Canted on-axis	None	Canted on-axis in x and y	Canted on-axis in x only	Canted on-axis in x and y
# Heliostats	29,052	28,593	29,048	28,745	28,559	28,126	28,164
Rec Height [m]	13.40	14.00	12.59	13.30	12.49	13.81	12.86
Rec Diameter [m]	13.59	11.97	12.07	13.57	12.55	13.36	12.41
Rec Aspect Ratio	0.99	1.17	1.04	0.98	1.00	1.03	1.04
Tower Optical Height [m]	140	134	132	133	132	135	134
Total Land Area [acre]	1,232	1,268	1,318	1,244	1,229	1,190	1,185
Annual Output [GWe-hr]	436.4	429.7	429.3	428.1	424.9	427.7	425.2
Nominal LCOE [¢/kWhr]	11.95	12.00	11.97	12.10	12.08	12.11	12.07

The key findings from the system benefit study were:

- The larger 2.6 AR heliostat reduced LCOE compared to the 1.5 AR heliostat for all facet focal lengths and canting configurations. Crespo [13] and Corsi [7] also found that larger AR have positive impact on system performance.
- Relatively small differences in LCOE between flat, canted, and canted + focused.

Based on these findings, the SunRing’s mirror area was increased to 27m<sup>2</sup> by adding two facets to the sides of the ROP design for a final aspect ratio of 2.64 including mirror gaps. Additionally, flat mirrors were specified, and the baseline design allows for canting.

### 1.3.2 Stow height

It was originally hypothesized that a low-to-ground stow height would greatly reduce wind loads on the heliostat and therefore result in cost savings in materials and drives. To test this hypothesis, three stow heights were investigated:

- Low to ground stow: 3.75 ft above grade
- Mid stow: 5.5 ft above grade
- Typical stow height: 8.28 ft above grade (approximately at middle of mirror array when mirror array is vertical)

Wind load testing was carried out on each stow height (details in Section 1.4.1), and conceptual models were created for each. The only marked advantage for a low stow height is reduced wind loads at low elevation angle orientations. This is offset by the following disadvantages:

- Wind loading at 90 elevation is practically the same for all stow heights.
- Wind loading at higher elevation angles sizes nearly all components.
- Increases loading on the elevation actuator
- PV and battery size increases to cover higher energy demands from elevation actuator

For the reasons above, the typical stow height design was chosen.

## 1.4 Wind Tunnel Testing

The wind engineering firm CPP was contracted to perform atmospheric boundary layer wind tunnel testing. CPP performed the original heliostat testing in the late 1980's that culminated in the Peterka wind load report [11] which remains one of the few publicly available reports on heliostat wind load coefficients. Testing was performed in two sequential steps, isolated heliostat parametric testing followed by detailed in-field testing. Figure 4 provides the sign convention.

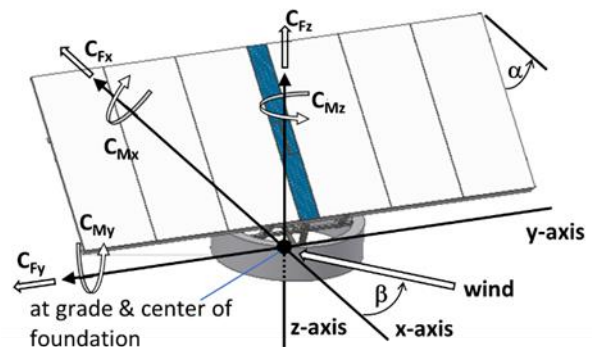


Figure 4 Sign convention for wind loading

### 1.4.1 Isolated Heliostat Parametric Testing

The first phase involved testing isolated heliostats with seven different heliostat configurations where aspect ratio, stow height, and foundation diameter were varied. As the 2.6 aspect ratio proved optimum during the system benefit study and structural analysis, the wind tunnel results for this aspect ratio were studied in detail. Table 15 presents the peak wind load coefficients at the worst-case elevation angle,  $\alpha$ , and wind direction,  $\beta$  for varying stow heights and foundation diameters.

*Table 15 Peak Coefficients from Isolated Heliostat Testing*

CPP ID	Aspect Ratio	Stow Height [ft]	Foundation OD [ft]	GCM <sub>y</sub>	GCM <sub>z</sub>	GCF <sub>x</sub>	GCM <sub>x</sub>	GCF <sub>z</sub>
1	2.6	3.75	10	-1.25	-0.60	-1.67	-0.31	0.99
2	2.6	5.5	10	-1.27	-0.58	-1.68	-0.38	-1.03
3	2.6	8.28	10	-1.24	-0.54	-1.56	-0.40	-1.19
4	2.6	3.75	12	-1.21	-0.61	-1.64	-0.30	0.91
At 90° elevation angle							At 30° elevation angle	

With the heliostat at a 90° elevation angle, its height above grade is independent of stow height. Thus, load coefficients that peak at 90° elevation angle are not influenced by stow height as shown in Table 15 for base overturning (GCM<sub>y</sub>), azimuth twisting (GCM<sub>z</sub>), and drag (GCF<sub>x</sub>) coefficients. As expected, coefficients that peak at 30° elevation angle are reduced as stow height drops.

In stow, My and Fz combine to define the required mass of a ballast type foundation, and these coefficients are correlated to stow height as shown in Table 16. My and Fz are minimized for an intermediate stow height where the lowest stow height geometry sees a larger My as its mirror plane is offset from the foundation center. The impact of stow height on foundation cost was captured between stow heights of 5.5-8.3 ft (IDs 2-3) with a material cost formula of \$2.6/(in of stow height). This function was used when optimizing the final stow height of the SunRing. Lastly, foundation diameter was not found to have a significant impact on any loading (comparing IDs 1 to 4).

*Table 16 Peak Coefficients in Stow from Isolated Heliostat Testing*

CPP ID	Stow Height [ft]	GCM <sub>y</sub>	GCM <sub>z</sub>	GCM <sub>x</sub>	GCF <sub>z</sub>	GCF <sub>x</sub>
1	3.75	-0.19	0.02	-0.13	0.20	0.14
2	5.5	0.15	-0.01	-0.16	0.17	0.17
3	8.28	0.26	-0.03	-0.17	0.22	-0.21
4	3.75	-0.14	0.02	-0.14	0.20	0.17

### 1.4.2 Detailed In-Field Testing

After down selecting to an overall heliostat configuration, detailed in-field testing was performed to determine the shielding effect of exterior solar field heliostats on interior heliostats. Additionally, of the 49 scale models, seven were instrumented with pressure taps to provide pressure distributions across the mirror surface. The heliostat geometry used for in-field testing closely mimics the final SunRing concept. A ground coverage ratio (GCR) of 0.19 was used which is the weighted average GCR for the baseline solar field. Figure 5 presents the wind tunnel test section.



Figure 5 In-field wind tunnel test set-up

Interior heliostats are defined as heliostats located in rows four and greater from the periphery, and they do see a marked reduction in wind loads as shown in Table 17. Designing interior and exterior specific SunRings will result in material cost savings, but this needs to be weighed against the increase cost in construction supervision and logistics required to successfully manage the construction and installation of at least two different heliostat designs. Additionally, the interior loading is only valid for heliostats located in a  $GCR \geq 0.19$  (e.g. where loading will be at most that from the wind tunnel). Exterior heliostats would need to be installed in approximately 50% of the solar field where  $GCR > 0.19$ . Fewer exterior specific heliostats could be installed if additional GCR configurations were run in the wind-tunnel, but the cost to do so is likely not justified until the SunRing has been deployed commercially.

Table 17 Interior heliostat wind load reduction for non-stow orientations

Load Component	Fx	Fz	Mz	My <sup>1</sup>
Maximum Interior/Exterior Gust Load	52%	72%	78%	50%
Maximum Interior/Exterior Mean Load	41%	53%	78%	61%

<sup>1</sup>Measured at center of mirror plane

The SunRing design utilizes exterior heliostat wind loads to size all structural members and drives. Interior heliostat wind loads are only used to calculate optical performance. Interior loads are appropriate here as the ultimate goal is to quantify the solar field's average optical performance where the interior wind load is a good approximation for the average wind load in the solar field.

### 1.5 FEA Analysis – methodology

A finite element model of the full heliostat was created in Dlubal RFEM analysis software and analyzed for both structural and optical performance. Dead load, wind load, thermal expansion, and pre-load from the azimuth drive spring were applied to the model for both optical and survival design cases. Wind loads were derived from the wind tunnel study described in Section 1.4. Table 18 presents the evaluation criteria and wind speed basis used for both optical and structural performance evaluations. There is not a single load case that critically stresses all structural members

simultaneously, and it is not explicitly known which load case will critically stress a member. Therefore, a multitude of load cases were analyzed where the wind direction and heliostat elevation angle vary.

*Table 18 FEA structural and optical analysis cases*

Evaluation Criteria	Wind Speed	Wind Direction	Elevation Angle [°]
<b>Optical Performance</b> Mirror surface RMS slope error, annual energy weighted. Targets: <= 1.5mrad (calm) / 2.1mrad (windy)	1-hr mean wind load seen with 3-sec gust speeds of Calm: 11.2 mph (5 m/s) Windy: 26.8 mph (12 m/s)	Front & Rear	30
			45
			60
			75
<b>Structural Performance</b> AISC design ratio <.91 in all axial members, stress ratio <.91 in non-axial members	Gust wind load during 3-sec gust speed of 40 mph	Front & Rear	30
			60
			75
			90
	Gust wind load during 3-sec gust speed of 94 mph	Front & Rear	0

Structural performance was evaluated with the AISC ratio on axial members. The AISC design ratio is the ratio of applied load vs. allowable load based on material yield and member stability. Non-axial members are evaluated with a pure maximum stress over yield stress ratio.

Optical performance requires an energy weighted calculation using the factors in Table 19. This table presents the annual energy delivered as a function of elevation angle for the baseline solar field.

*Table 19 Annual energy delivered to receiver at varying elevation angles*

Elevation Angle [°]	0-10	10-20	20-30	30-40	40-50	50-60	60-70	70-80	80-90
Annual Energy to Receiver [MWhr]	13,008	46,866	95,994	150,798	240,140	298,771	302,959	150,485	12,976
% of Total	1%	4%	7%	11%	18%	23%	23%	11%	1%

### 1.5.1 Soil Model

A linear elastic soil model was added to the FEA model to predict how loads are distributed across the foundation piles. Soil conditions from a typical Arizona site were utilized in specifying soil parameters. The soil model has a large influence on loading in the piles as shown in Table 20. On average, the soil conditions of all 6 piles will be similar and comparable to the overall project's soil conditions, and in this case the piles

see the lowest loads. However, if the soil is very stiff (i.e. rocky conditions) at just one pile, then this pile will see much higher loads. This scenario is conceivable, and the piles are designed to react the highest load condition in Table 20. A site-specific geotechnical study may find that the chance of abnormally stiff ground conditions is very low, and in this case a lower cost pile could be deployed.

*Table 20 Impacts of soil boundary condition on foundation pile loading*

Soil Boundary Condition	Max Axial Load [lbf]	Max Lateral Load [lbf]
Linear elastic model at all 6 piles	994	578
Perfectly stiff at all 6 piles	1,508	1,421
Linear elastic model at 5 piles / perfectly stiff at 1 pile	1,677	1,675

### 1.5.2 Thermal Expansion

The impact of differential thermal expansion on optical performance was evaluated as the coefficient of thermal expansion is higher for the facet's steel rib than the mirror itself. The mirror facets are fabricated at the mirror factory which can be assumed to be a climate-controlled building at a temperature of 70°F. The SunRing is designed for extreme site temperatures of -20°F and 131°F. The extreme low is likely to occur overnight; thus, a lower bound temperature of 14°F was used for thermal expansion runs.

### 1.6 Azimuth Drive Evolution

The carousel azimuth drive provides the largest SunRing cost savings compared to a pedestal heliostat. A carousel track provides a large gear reduction (54:1) enabling the use of a low-cost and relatively low-precision azimuth motor and gearbox. However, realizing these cost savings while ensuring tracking accuracy and load capacity was challenging and required a significant design and validation effort.

Two approaches to the azimuth drive were evaluated for the SunRing: friction drives and geared drives. Friction drives have the benefit of zero backlash at the track interface and are conceptually simple, but they are challenging to implement in a heliostat where wind loads must be reacted without slippage. Geared drives eliminate slippage and can react high loads but must be implemented without precision machined gears and without lubrication to be practical and cost-effective.

The following principles were constant between all azimuth drive designs:

- A spring biases a gearmotor driven wheel or gear into a track.
- Azimuth drive reacts all wind induced twisting moments on the heliostat (e.g. CMz in Figure 4).
- The spring load is sized to react above twisting moment and hold the heliostat stationary against design wind loads.
- Driven wheel/gear assembly designed to accommodate non-circular azimuth tracks (e.g. manufacturing tolerance will produce an non-ideal azimuth track)



The following outlines the azimuth drive's evolution from a friction drive into the final geared drive design.

### 1.6.1 Friction Drive

The original azimuth drive was a friction drive design which was an evolution from Abengoa's ROP friction drive. The gearmotor drove a v-groove wheel against a tubular track. A proof-of-concept azimuth drive (drive wheel, idler wheels, base triangle, and tubular track) was built at the end of BP1 as shown in Figure 6.

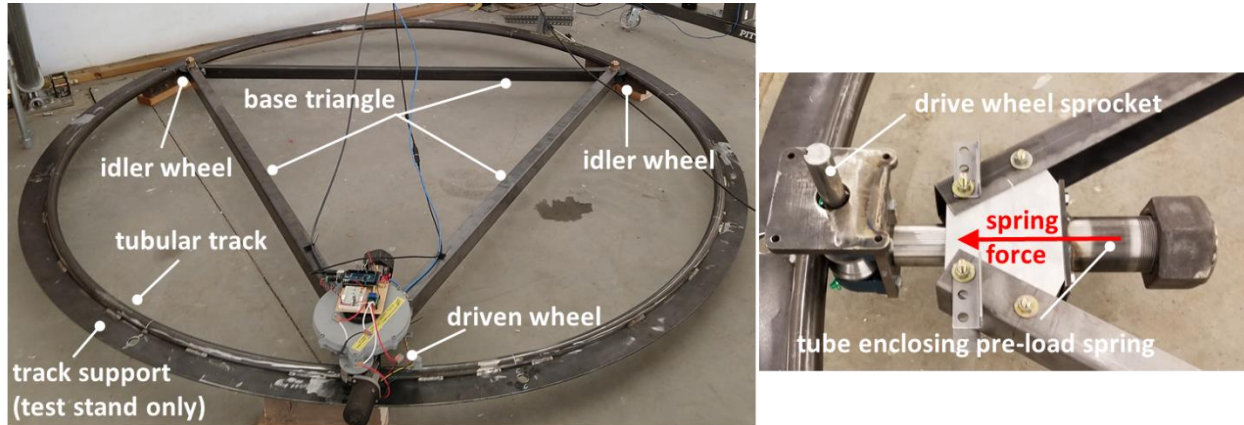


Figure 6 Friction drive proof-of-concept overall test (left), close-up of driven wheel with gearmotor removed (right)

The main goals of the test stand were to quantify the coefficient of friction (COF) between the drive wheel and track and monitor the wear of the track and wheels while accumulating 30 years of equivalent life. Early on, an average COF of 0.12 was measured, which was at the lowest end of published values. This low COF required extremely high spring pre-load (~12,000 lbf for BP1 design) to prevent slippage, which would require costly structural reinforcements and create high wear on the drive components. Thus, testing was stopped, and alternative wheel and track materials were tested with hopes to increase the COF. The following combinations were found to have COF's of 3-4X higher than the tested azimuth drive's steel wheel on steel track.

- Diamond coated steel wheel on steel track
- Polyurethane wheel on steel and concrete tracks

Using a surface coating or softer wheel has potential wear issues that must be addressed. The first measure is to use line contact between the wheel and track rather than the 2-contact point design of the tested azimuth drive as shown in Figure 7.

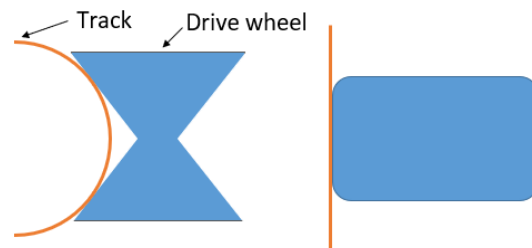


Figure 7 Drive wheel/track interfaces, proof-of-concept design (left), proposed line contact (right)

The advantage of the 2-contact point design is the ability to react uplift/downforce loads. With line contact, additional wheels need to be added to the overall azimuth drive to react vertical loads.

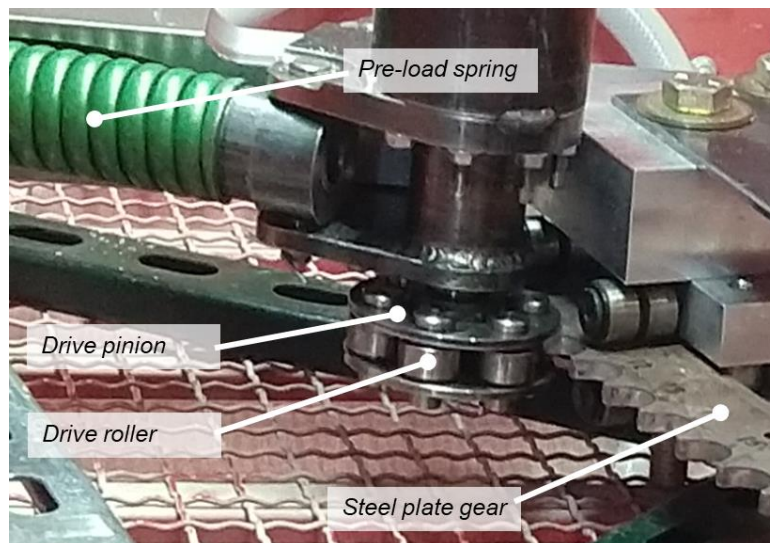
While preliminary cost analysis predicted some savings with a friction drive, the geared roller pinion design was chosen as the preferred path forward beginning in BP2 due to the lower risk of positioning errors, lower spring pre-tension force, and longevity concerns with urethane and coated wheel options.

### 1.6.2 Geared Drive

An inherent advantage of a positive drive is that a properly designed system eliminates the potential for slippage between the drive wheel and the track, which is a key deployment risk with a friction drive. However, there are several technical challenges for a geared drive system:

1. The backlash between the drive wheel and track must be minimized over the 30-year heliostat life.
2. The gear system must function without lubrication and in a dusty environment.
3. High contact stress between gear teeth typically requires hardened steels, which increase the cost especially for large track gears.

A roller pinion gear design was identified as the best candidate technology to meet these challenges. In a roller pinion gear, Figure 8 below, the drive pinion is equipped with multiple rollers that mesh to a fixed profile track gear. The inclusion of rollers eliminates sliding at the gear contact surface, which reduces wear and allows lubrication-free operation.



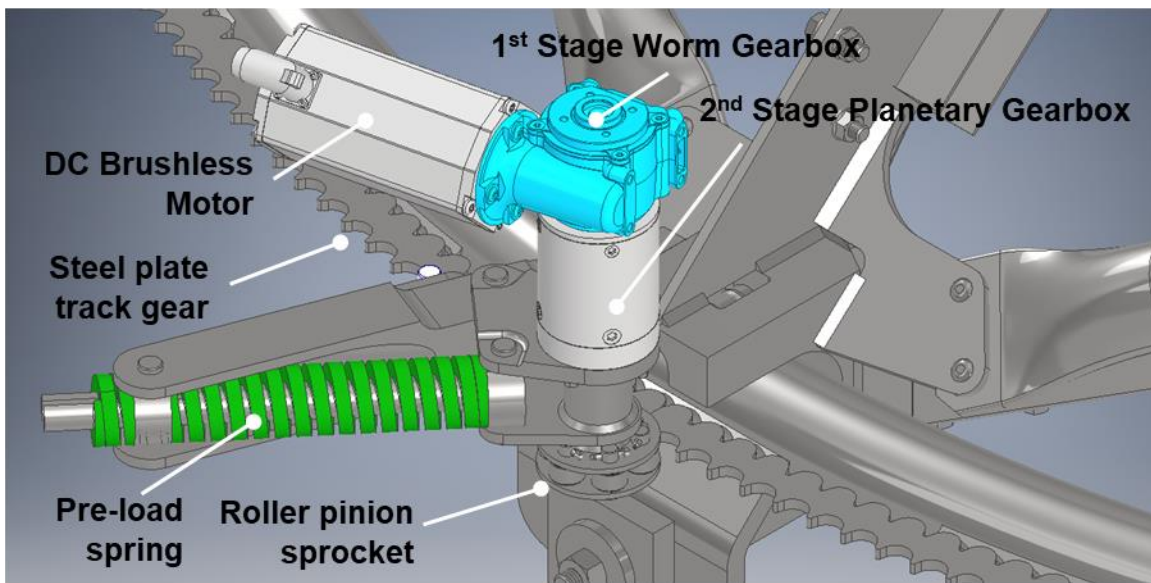
*Figure 8 Roller Pinion Gear and Track – BP2 Lifetime Test*

Typical roller pinion drive systems are designed for high-speed applications (11 m/s) and achieve low backlash with a precisely machined track with a specific tooth profile that ensures consistent meshing. The much slower speed of the SunRing (0.6 m/s) enables the use of a simplified track profile that can be cut using less expensive water jet cutting and potentially stamping at commercial scale. Low backlash is maintained with the simplified profile by spring-loading the drive wheel into the track.

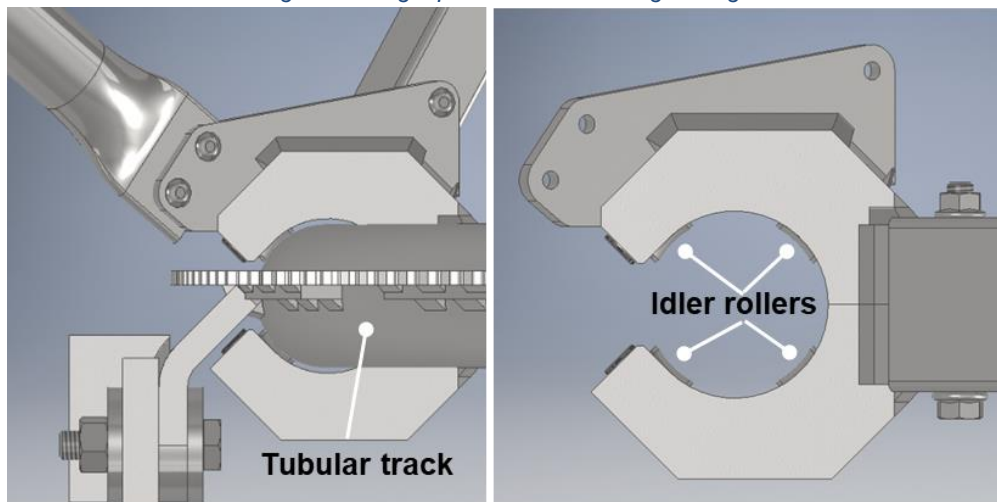
### *Pivoting Carriage Design*

The first deployed azimuth drive utilized a pivoting drive carriage as shown in Figure 9 and Figure 10. This is the design deployed on the BP2 full-scale heliostat prototypes. This and all subsequent azimuth drive designs use the following design philosophy:

- Drive hub only reacts tangential loads.
  - The drive hub has a radial degree of freedom relative to the track.
- Radial load is only reacted at the two idler hubs.
  - Idler rollers react load in both vertical (uplift and downforce) and both radial (inward and outward) directions. This change reduces deformation in the structure under wind loads since the drive pre-load spring does not compress due to twist or drag loads on the heliostat.



*Figure 9 Budget period 2 drive carriage design*

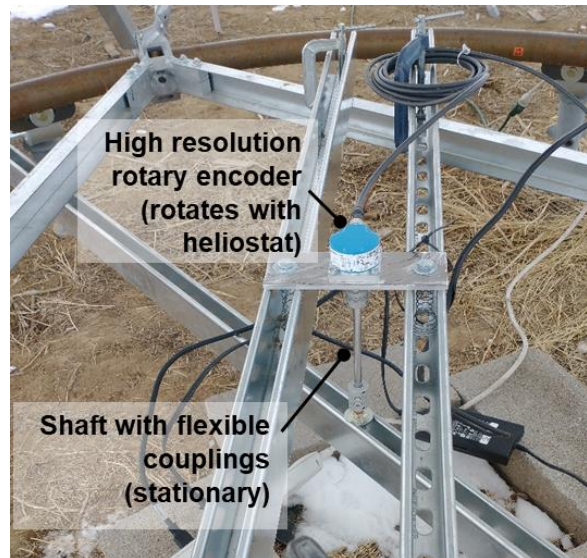


*Figure 10 Budget period 2 idler hub design (left), with track and upper struts removed for clarity (right)*

The tubular track will never be perfectly circular, and its specification allows a 0.25 inch out-of-round (OOR) tolerance (i.e. 0.25 inch maximum variation in its diameter). It was initially believed that this variation only induced tracking errors due to a change in gear reduction between the azimuth pinion and the track. This is accounted for in the tracking error allowance. However, track OOR error also causes the heliostat's center of azimuth rotation to move and not be ideally centered over the center of the track as assumed in the controller's kinematic model of the heliostat. Initial spot checks on the ring's diameter showed that offsetting the heliostat center from the track center causes a large tracking error. Thus, a dedicated azimuth position test fixture was designed and installed to quantify the error.

### *Characterizing Positional Accuracy*

An azimuth position test fixture was created to accurately measure the heliostat's azimuth position through a full 360° rotation about the azimuth track. The test fixture mounts a high-resolution rotary encoder along the heliostat's azimuth rotation axis as shown in Figure 11. The azimuth motor was controlled to perform a full 360° rotation by taking 0.5 mrad heliostat tracking steps with pauses of 2 seconds between each step. The heliostat's assumed azimuth position (based on its kinematic model) and the actual position from the high-resolution rotary encoder were used to calculate azimuth position error.



*Figure 11 Azimuth position test fixture*

Figure 12 presents the positional error over the full azimuth range of motion. There are large position errors that evolve relatively slowly as the heliostat rotates about the azimuth axis. In addition to this global azimuth error, there is a smaller cyclic error that repeats with each pin-to-pin movement of the roller pinion as seen in Figure 13.

The large global error is due to track OOR error causing the heliostat's center of rotation to not coincide with the tracks center. Correcting this error occurs through either on-sun heliostat calibration, azimuth drive calibration, or a combination of the two as discussed in Section 1.14.3. Pin-to-pin error is reduced through design updates discussed below.

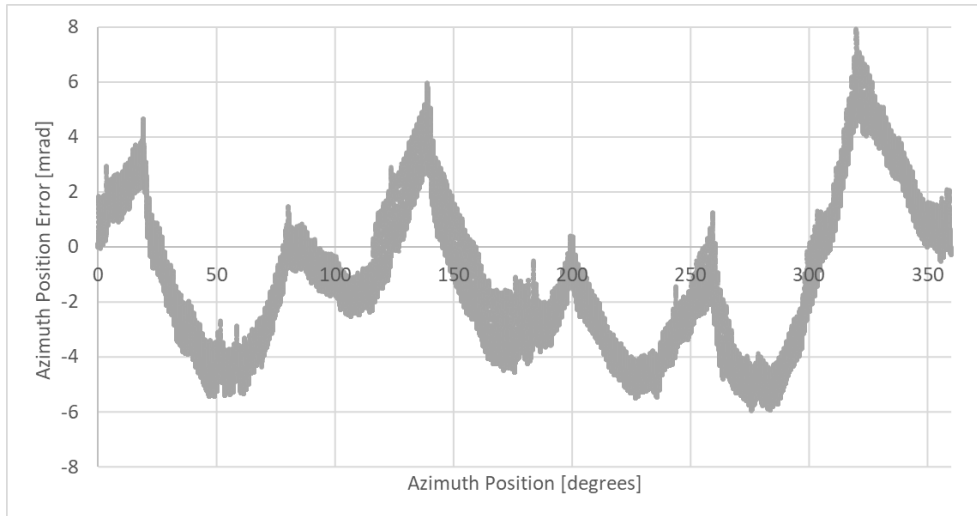


Figure 12 Azimuth position accuracy results over entire 360° track of BP2 heliostat

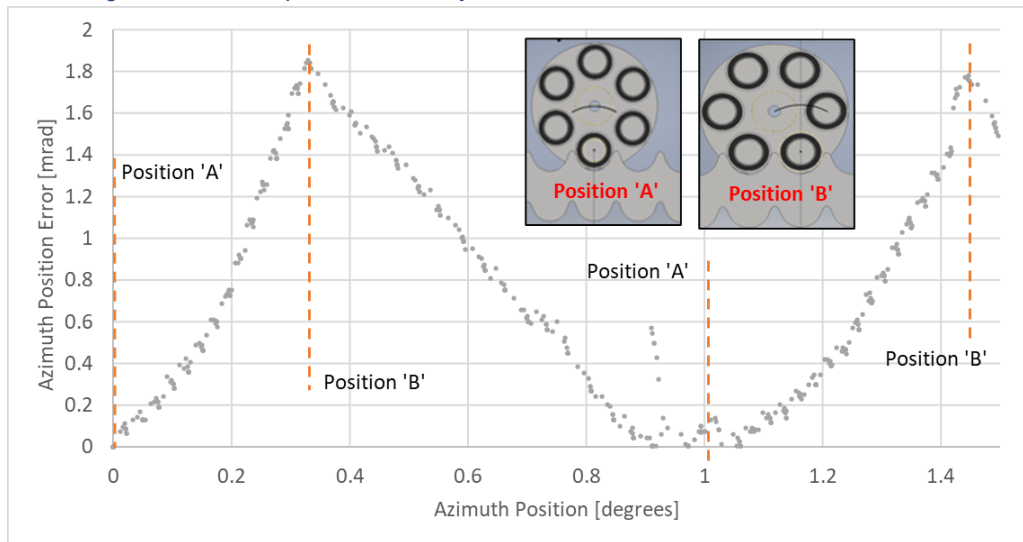


Figure 13 Azimuth position accuracy results pin-to-pin error of BP2 heliostat

### Design Issues

The BP2 design performed well overall, but there were two areas that required further design refinement.

### Pivoting Drive Carriage Introduces Tracking Error

The spring-loaded azimuth drive carriage pivots about a fixed point which allows the carriage to move relative to the track to ensure drive sprocket engagement and accommodate track diameter errors. However, the pivoting action creates a small rotation in the carriage (shown by the blue arrow in Figure 14) that adds or subtracts from the angular tracking step performed by the drive motor. Geometric analysis showed that approximately 1 mrad of cyclic pin-to-pin error is due to this effect.

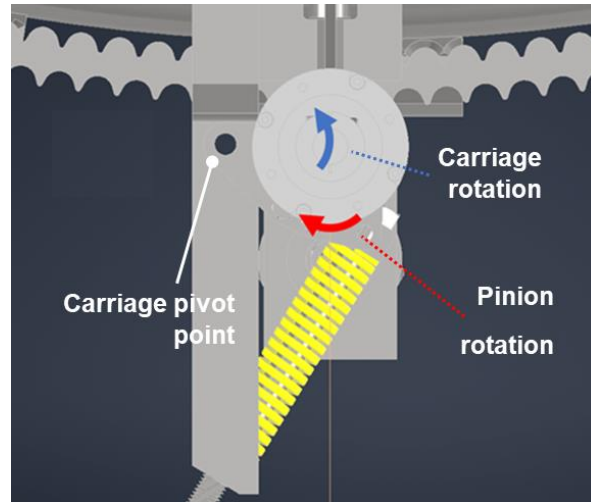


Figure 14 Pivoting Drive Carriage Angular Error Source

In addition to pin-to-pin error, this effect also contributes to global azimuth error pattern. As the effective track diameter changes (due to manufacturing tolerance in the track), the angular change in the carriage works with or against the azimuth motor and generates error.

**Mitigation:** linear spring guide developed in budget period 3

### Clearance at Idler Roller / Tubular Track Interface

Clearance between the idler rollers and the azimuth track tube was identified as another potential source for tracking errors. To account for manufacturing tolerance in the track tube and hubs, the rollers are designed to have a small amount of clearance to the track. This clearance means that at any given time only 2 of the 4 idler hub rollers, and one of the two drive hub idler rollers, are in contact with the track tube.

In low wind conditions the drive pre-compression spring and the mass of the heliostat result in the outermost idler hub rollers and the upper drive idler roller being in contact with the track. However, as external wind loads are applied the roller engagement changes.

Idler hub roller engagement remains steady through the optical windy mean load condition with a transition occurring somewhere between 12 m/s mean and 15.6 m/s gust loads. Because the spring load does not influence the engagement of the drive hub rollers, changes in roller engagement at the drive hub occur at much lower wind loads. Even a 5 m/s mean load can reverse the loading at the drive hub when the heliostat is in its worst-case drag orientation.

The optical impacts of changes in roller engagement depend on the amount of clearance between the rollers and the track, as shown in Table 21. The drive hub clearance results only in elevation angle error, while the idler hub clearance results in both azimuth and elevation error.

*Table 21 Idler roller clearance influence on pointing error*

Roller Clearance	Idler Hub Pointing Error [mrad]	Drive Hub Pointing Error [mrad]
1/64"	.36 azimuth / .10 elevation	0.0 azimuth / .25 elevation
1/32"	.45 azimuth / .17 elevation	0.0 azimuth / .50 elevation
1/16"	.85 azimuth / .35 elevation	0.0 azimuth / .99 elevation

**Mitigation:** select idler rollers have adjustable clearance set during heliostat assembly as deployed in BP3 design

## 1.7 Foundation Evolution

The following details the different foundation options explored within the project. Embedded pile foundations are the baseline and preferred option, but some sites may benefit from a ballast foundation where no ground penetration is required.

### 1.7.1 Concrete Ballast Foundation

A pre-cast concrete foundation was the original foundation design, and this overall concept was carried over from Abengoa's ROP heliostat. A ballast foundation enables the complete heliostat and foundation to be assembled and dropped as a complete unit in the solar field. The ballast foundation was developed in parallel with the friction azimuth drive, but the geared azimuth drive would be compatible with a ballast foundation too.

There are several risks related to soil movement causing foundation movement which in turn would increase tracking errors until the heliostat is re-calibrated. The engineering firm Kleinfelder was hired to perform a civil engineering review of the ballast foundation in BP2. The study quantified the risk of foundation movement due to soil movement (Table 22) and soil settlement due to heliostat loading (Table 23).

*Table 22 Soil interactions with foundation*

Soil Mechanism	Probability	Required Conditions	Mitigation Measures
Frost heave	Not likely, low levels of soil moisture at desert project locations.	<ul style="list-style-type: none"> <li>• Soil moisture</li> <li>• Freezing temperatures</li> <li>• Porous soil</li> </ul>	Embed foundation below frost depth.
Expansive soil	Low to moderate, dependent on-site soil type.	<ul style="list-style-type: none"> <li>• Soil moisture</li> <li>• Expansion soil</li> </ul>	SF drainage designed to prevent water accumulation at foundations.
Soil erosion due to water	Not likely with proper site drainage.	<ul style="list-style-type: none"> <li>• Flooding</li> </ul>	SF drainage designed to prevent floodwater from impacting foundation.

The overturning safety factor (SF) of 1.5 in Table 23 was based on the International Building Code and ASCE 7 by the American Society of Civil Engineers (ASCE). This increases the ballast foundation weight to 5300 lbm from the 3600 lbm original used by Solar Dynamics based on a 1.1 safety factor. Soil bearing capacity was checked against soil pressures, and it was found that general silt and silty sand soil types would require increasing the contact area of the ballast foundation to meet a 2.25 SF. Lastly, Kleinfelder assessed tilt in the foundation due to uneven ground settlement as a result of overturning moments imparted on the heliostat. The maximum *elastic* tilt is estimated to be 1.3 mrad of rotation, and no permanent deformation is expected.

*Table 23 Foundation movements due to external loading*

Movement Mechanism	Required Safety Factor	Mitigation Measure
Overturning	1.5	Increase foundation mass to 5300 lbm
Sliding	2.0	If needed, add protruding elements to foundation bottom
Twisting	1.5	

### 1.7.2 Embedded Pile Foundations

Discussions with commercial ground screw anchor vendors in BP2 revealed that the cost of ground screws suitable for a small heliostat have dropped significantly since 2015 when the SunRing was initially conceived, to the point where a foundation using ground screws can be cost competitive, and even achieve cost savings, over a ballast ring foundation. This is true even when factoring in the greater steel mass required in a rigid azimuth track that spans between discrete ground screw supports, and the additional installation labor required to install ground screws.

#### *Azimuth Track OD and Number of Ground Anchors*

The number of ground anchors supporting the azimuth track along with its outer diameter have a large impact on the heliostat’s optical performance. The best optical performance occurs when the drive and idler hubs are directly above ground anchors while the worst occurs when they are midway between ground anchors.

Table 24 presents the three design cases that were considered with their impact on cost. The ‘optical cost’ was calculated from a system benefit curve which defines the \$/m<sup>2</sup> savings (or penalty) for improved/ (or reduced) optical error compared to the 4 mrad SunRing baseline. The \$/m<sup>2</sup> savings/penalty were calculated by finding the required heliostat installed cost to match the LCOE of the baseline SunRing.

The difference between the two assumption cases in Table 24 is the cost for the ground screw anchors. On a commercial scale, the anchor’s unit costs (\$/lb) should approach that of the track, and this case was used for final design selection. Both 3 and 6-pile options with the larger 4.5-inch OD track have similar total costs, but the 6-pile design has better optical performance which leads to selecting 6-piles. The 6-pile design of BP2 with the smaller 2.5-inch OD track is \$1/m<sup>2</sup> less, but because of the importance of showing good optical performance with the BP3 heliostat testing, the larger 4.5-inch OD was selected. In summary, a 6-pile, 4.5-inch OD track tube is the final design.



*Table 24 Azimuth track OD and # of foundation anchor design study*

Assumption Case		BP2 Cost Estimate Baseline			Ground Anchor \$/lb = Azimuth Track \$/lb		
Design Case		6-pile, 2.5OD tube (BP2)	3-pile, 4.5OD tube	6-pile, 4.5OD tube	6-pile, 2.5OD tube (BP2)	3-pile, 4.5OD tube	6-pile, 4.5OD tube
<b>Costs [\$ /m<sup>2</sup>]</b>	<b>Piles</b>	\$7.79	\$3.89	\$7.79	\$2.50	\$1.25	\$2.50
	<b>Pile Install</b>	\$3.24	\$1.62	\$3.24	\$3.24	\$1.62	\$3.24
	<b>Ring</b>	\$5.08	\$7.42	\$7.95	\$5.08	\$7.42	\$7.95
	<b>Anchor Mount</b>	\$1.46	\$0.73	\$1.46	\$1.46	\$0.73	\$1.46
	<b>Anchor Hardware</b>	\$1.16	\$0.58	\$1.16	\$1.16	\$0.58	\$1.16
	<b>Lower Triangle</b>	\$2.01	\$1.93	\$1.96	\$2.01	\$1.93	\$1.96
	<b>Optical Cost</b>	\$4.92	\$7.74	\$3.10	\$4.92	\$7.74	\$3.10
	<b>Total</b>	<b>\$25.66</b>	<b>\$23.92</b>	<b>\$26.66</b>	<b>\$20.38</b>	<b>\$21.28</b>	<b>\$21.38</b>

## 1.8 Final Design

The SunRing’s final design is summarized in the following sections along with its predicted FEA performance, total installed cost breakdown, and measured optical performance.

### 1.8.1 Structural Design

The SunRing structure is grouped into three main categories: mirror facets, mirror support structure, and lower support structure.

### *Mirror Facets*

Two steel reinforcing ribs are adhesively bonded to the rear of 4 mm glass mirrors as shown in Figure 15. This design builds on a similar approach for large-format parabolic trough mirrors explored by Solar Dynamics under award DE-EE0007121 [6], and aligns with recent developments by other heliostat technology companies [9].

A two-component adhesive (Sika's Sikasil AS-785) bonds the steel ribs to the mirror. This adhesive is already used in the PV and building industry. Sika performed adhesion tests with Solar Dynamics provided mirror coupons. Sika concluded: "When the substrate was pre-treated using Sika® Aktivator-205 prior to the application of Sikasil® AS-785 the adhesion results were excellent with >95% cohesive failure." Cohesive failure occurs when a layer of adhesive remains on both surfaces in contrast to an adhesive failure where the bond at the substrate fails.

The steel ribs and glass mirror have varying coefficients of thermal expansion, and the relatively elastic adhesive helps to dampen out thermally induced stress when the facet temperature departs from its neutral temperature. Adhesive is applied at a 50% coverage ratio with 10-inch adhesive beads followed by 10 inches of no adhesive down the length of the rib.

### *Mirror Support Structure (MSS)*

The SunRing heliostat utilizes a torque tube supporting six mirror facets in a high 2.6:1 aspect-ratio (AR) array as shown in Figure 16. A high AR lowers wind loads by reducing the heliostat height, and it enables all assembly, installation, maintenance, and washing to be performed from ground level. To utilize existing automated manufacturing infrastructure, a two-part torque tube with a joint at the center was developed.

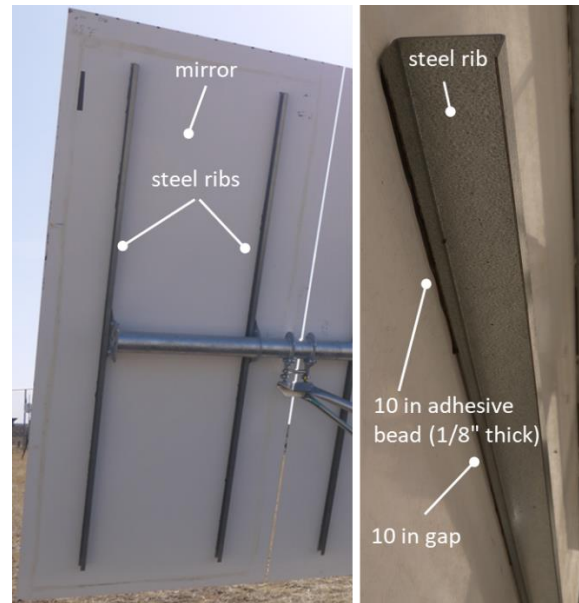


Figure 15 Mirror facet on heliostat (left) and close-up of rib (right)

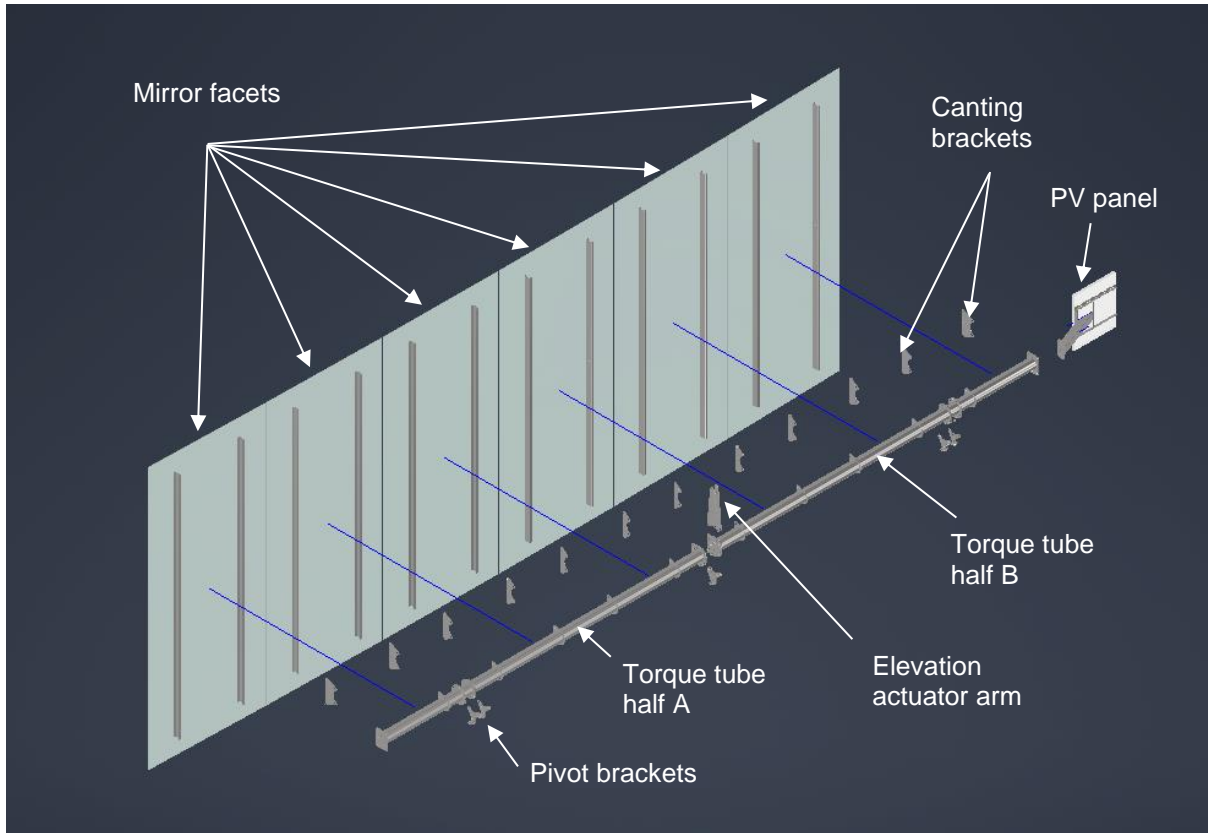


Figure 16 Mirror support structure overall design

Ribs on the mirror facets are riveted to intermediate canting brackets which are attached to welded brackets on the torque tube via slotted, bolted connections that allow the mirrors to be aligned on the assembly jig (see Figure 17). The canting brackets vary in height along the torque tube, enabling a continuous, canted mirror array surface. The focal distance can be changed by replacing the intermediate brackets with different lengths.

In addition to enabling canting, the use of intermediate brackets may enable off-site facet alignment and eliminate the tooling and labor associated with factory alignment. The bolt holes in the intermediate brackets can be aligned using a jig, rather than the jig supporting the mirrors directly. Since the brackets are small, this alignment could be performed off-site, and the torque tube plus aligned brackets assembly is shipped to the field. The mirror facets would be riveted to the aligned torque tube at the on-site factory without further adjustment.

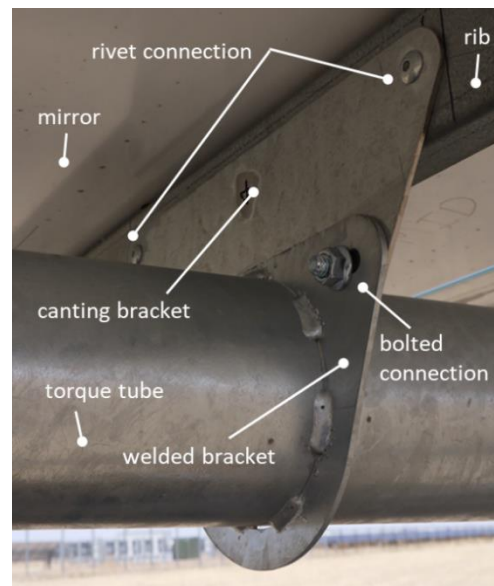
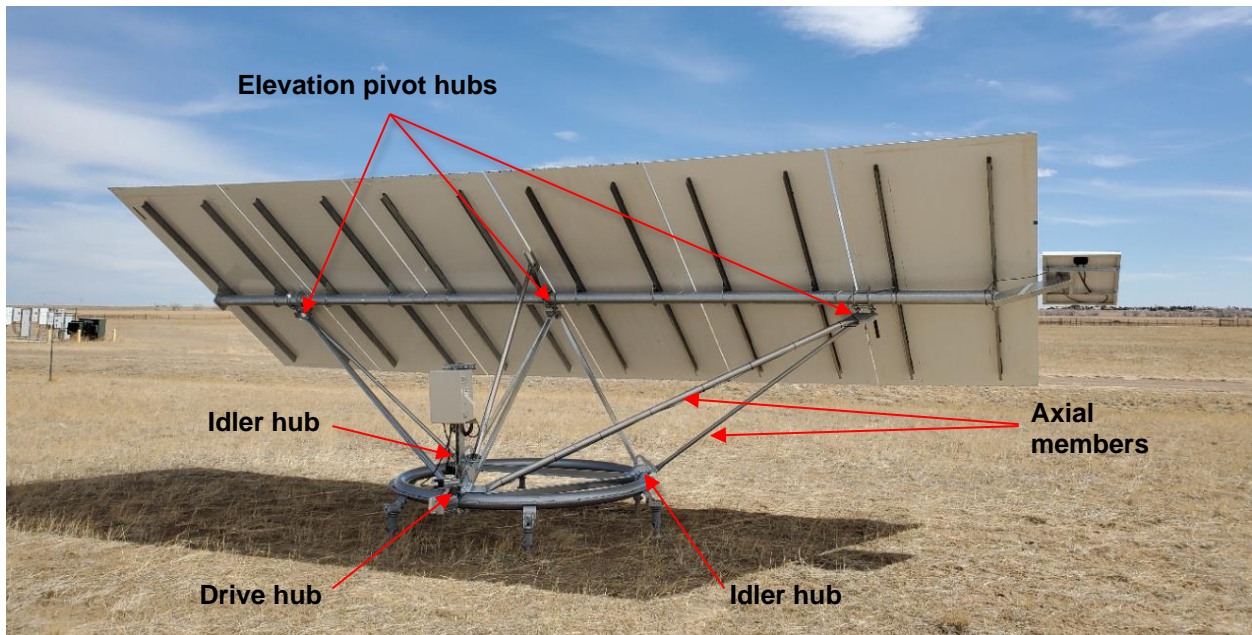


Figure 17 Canting bracket

The torque tube extends beyond the mirrors on one end to accommodate a PV panel. The torque tube connects to the heliostat's lower support structure at three elevation pivot points and one elevation actuator connection as shown in Figure 16.

### *Lower Support Structure*





Figure 18 presents the SunRing's lower support structure, which connects the mirror array to the azimuth track. The structure utilizes a novel triangulated space frame that significantly reduces the torque tube mass compared to a pedestal heliostat by supporting the tube against bending. Solar Dynamics has filed an international patent application under the Patent Cooperation Treaty (PCT) for this design as it is a key enabler of the SunRing's wide aspect ratio [16].



*Figure 18 Lower support structure overall design on 3<sup>rd</sup> prototype*

The base of the structure connects to the azimuth track via three hubs: two idler hubs and one rear drive hub. Details of the space frame are presented in Table 25.

Table 25 Space frame component details

Component	Prototype Image
<p><i>Idler Hubs</i></p> <p>Single piece idler hubs encircle the azimuth track with 4 opposing rollers. Two outer rollers (shown in picture) are mounted to eccentric shafts allowing adjustment during installation to minimize clearance to track. Two inner rollers (not shown in picture) are non-adjustable. The prototype hubs are machined and welded, but their design is well suited for casting at high volume.</p>	
<p><i>Drive Hub</i></p> <p>The drive hub engages the top and bottom of the circular track to react vertical load but allows movement in the radial direction to accommodate manufacturing errors in the track and space frame. The bottom roller is mounted to an eccentric shaft allowing adjustment during installation to minimize clearance to track. The elevation actuator, azimuth drive actuator, and control enclosure all connect to the drive hub.</p>	
<p><i>Elevation Pivot Hubs</i></p> <p>The elevation hubs connect the space frame axial members to the spherical rod end bearings. They are manufactured from simple welded steel plates. They connect to the struts with structural blind rivets and to the pivot bearings through slotted bolt holes for adjustability.</p>	
<p><i>Axial Members</i></p> <p>Two axial member types are used in the space frame. The longer and higher-load-carrying members are made from round tube sections with crimped ends, while the shorter sections utilize roll formed sheet metal channels. Both designs can utilize pre-galvanized steel to reduce corrosion protection costs, and both strut types have been proven in commercial CSP trough plants.</p>	

### **1.8.2 Elevation drive**

The main goal of the elevation actuator selection was to find an actuator that is already mass produced with a proven outdoor operation history. This eliminates the cost of a custom or low-volume drive as seen in traditional pedestal mount heliostats. Acme-screw based linear actuators meet both goals as they used within the PV-tracker industry. The main difference between a PV-tracker application is the SunRing's lower backlash requirements. This risk was mitigated through backlash testing described in Section 1.12.

A linear actuator from is the SunRing's baseline elevation drive with the following characteristics:

- \$156/unit at 40k volume
- Brushless DC motor
- 71.2:1 planetary gearbox
- TR18x4 SS spindle
- Bronze nut
- Max static load: 1572 lbf
- Rated dynamic load: 375 lbf @ 0.12 in/s

#### *Potential Ballscrew Alternative*

Ballscrew type linear actuators utilize a ball bearing at the nut/screw interface rather than sliding friction used in Acme-screw based actuators. Thus, ballscrews will see less wear at this interface and see less backlash growth over time. The main drawback to ballscrews in the past was their price premium; however, recent discussions with a new vendor have opposed this point. Ballscrew actuator samples from said vendor are being built to meet the SunRing specification with a Q2 2022 delivery. These have a similar price as the baseline Acme-screw actuator.

#### *Maintenance*

The linear actuator will likely require scheduled maintenance to regrease two areas. The first is at the nut/screw interface, and the second is the gearbox attached to the motor. Both will have grease nipples for quick application. The following is the regreasing frequency recommended by the suppliers above:

- Nut/screw: 5-10 year (Acme screw) 5-7 years (ballscrew)
- Gearbox: not needed (Acme screw) 3-5 years (ballscrew)

### **1.8.3 Azimuth drive**

The patent-pending carousel azimuth drive provides the largest SunRing cost savings compared to a pedestal heliostat [16]. A carousel track provides a large gear reduction (54:1) enabling the use of a low-cost and relatively low-precision azimuth motor and gearbox. However, realizing these cost savings while ensuring tracking accuracy and load capacity is challenging and requires a significant design and validation effort.

Several design iterations of the geared azimuth drive were analyzed throughout the project. The selected design is shown in Figure 19. The key features that make the design suitable for a low-cost heliostat are summarized Table 26.

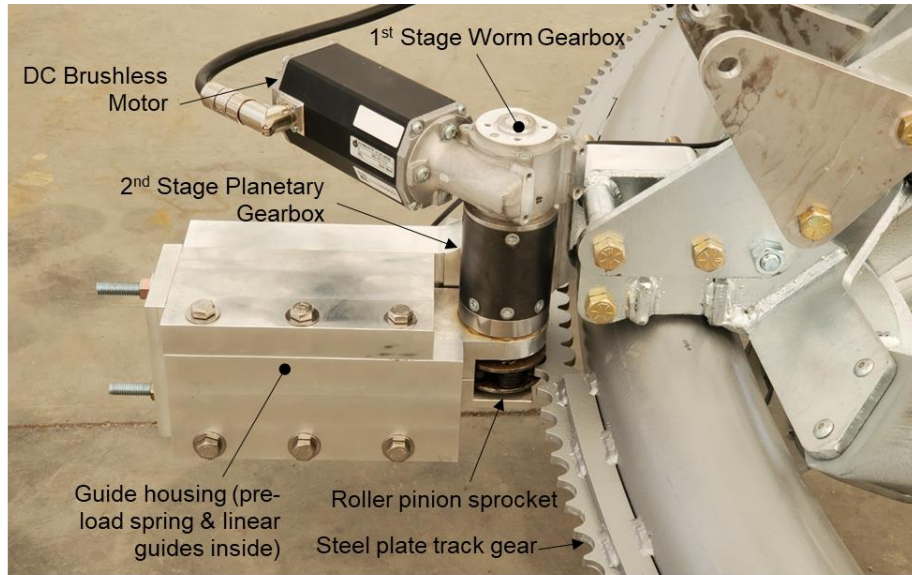


Figure 19 Baseline azimuth drive design

Table 26 Azimuth drive key cost reduction features

<p><b>Low-cost track gear manufacturing</b></p> <p>The track gear is water jet cut from hardened steel plate, making it lower cost than a large diameter machined gear. The pre-load spring and unique tooth profile allow for relatively loose manufacturing tolerance.</p>	
<p><b>Lubrication free</b></p> <p>Roller pinions work without sliding contact between the track and sprocket that requires lubrication in typical gears. The rollers utilize plastic plain bearings that also require no lubrication or maintenance.</p>	
<p><b>Low backlash</b></p> <p>The spring-loaded sprocket ensures continuous engagement between a roller and two adjacent gear teeth. This eliminates backlash regardless of manufacturing errors or wear.</p>	

*Range of motion*

The geared track is fabricated in 6x60° segments which are welded to tabs on the tubular track. The required azimuth range of motion (RoM) for a heliostat is a function of its field location where the north field requirement is ~150°. The number of 60° geared track segments installed on a given heliostat will be tailored based on its actual RoM needs. An average of 180° for the solar field is assumed.

### Accuracy Testing

The azimuth position test fixture described in Section 1.6.2 was used to isolate the accuracy of the azimuth drive. The pin-to-pin error is presented in Figure 20. The original data is offset from 0 mrad error due to the Out-of-Round error which is corrected using discretized Misalignment Parameters (Section 1.14.3). Applying this correction, pin-to-pin error oscillates about 0 mrad as shown in the right plot of Figure 20. The spread of the error is 0.65 mrad, and the average absolute tracking error is 0.17 mrad (slope basis) which is within the SunRing optical error budget.

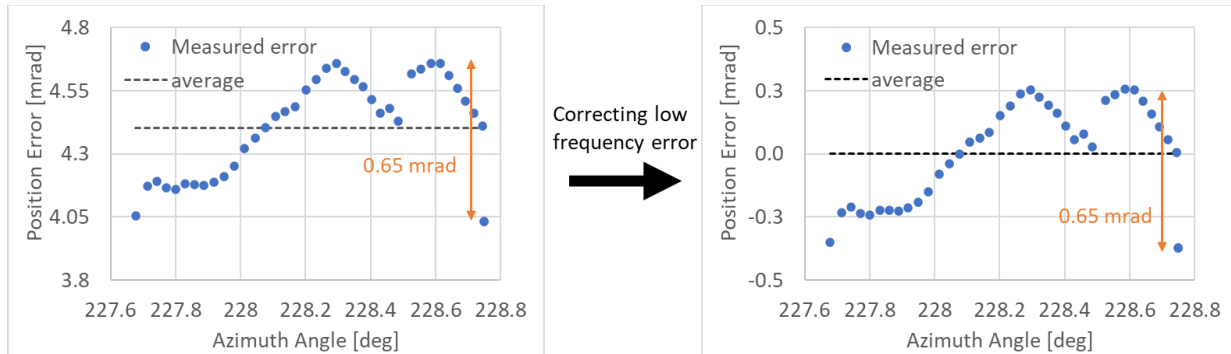


Figure 20 Azimuth position error: 1 pin-to-pin movement

### 1.8.4 Foundation

The SunRing utilizes 6X ground screws spaced 60° around the azimuth track. Ground screws are appropriate for relatively hard soils, but less expensive helical piles are a replacement when softer soils are present. Ultimately, the SunRing can accommodate the foundation type that is best suited for the given project. The baseline ground screw design is: 47” long x 3” OD x 0.147” wall thickness.

### 1.8.5 Finite Element Analysis

The detailed FEA model and evaluation criterion described in Section 1.5 was used to evaluate the SunRing heliostat design.

#### Structural Performance

Table 27 presents the structural performance results. The components highlighted in yellow are all axial members whereas the components in blue are all non-axial members. The non-axial members exceed the 0.91 design ratio slightly, but the stress ratio is likely artificially high due to mesh artifacts.



*Table 27 Structural performance of main components*

Component	Defining Stress or Load	Governing Load Case (LC)
Mirror support arms	342.6 MPa 0.97 Stress ratio	LC65 - 30° rear
Torque tube	333.1 MPa 0.94 Stress ratio	LC65 - 30° rear
Hubs	344.1 MPa 0.97 Stress ratio	Max Mz 75° front <b>and</b> Max Mz 90° front
Track	349.3 MPa 0.98 Stress ratio	Max Mz 75° rear <b>and</b> front
Outer legs	-8.09 kN 0.78 AISC ratio	Max MZ 90° rear
Inner legs	-5.25 kN 0.65 AISC ratio	Max MZ 75° rear
Diagonal struts	-10.09 kN 0.76 AISC ratio	Max Mz 75° front
Center strut	-3.93 kN 0.47 AISC ratio	LC - 0° rear
Base struts	-5.96 kN 0.61 AISC ratio	LC47 - 90° rear <b>and</b> Max MZ 75° rear

*Optical Performance*

The predicted optical performance of the SunRing is presented in Table 28. The Root-Mean Square (RMS) slope error at varying elevation angles, wind directions, and wind speeds was calculated. The annual solar field average uses the weighting factors provided in Table 19.

*Table 28 FEA model predicted RMS slope error.*

3-sec Gust Wind Speed	Elevation Angle and Wind Direction								Annual SF Energy Weighted Average
	30° rear	30° front	45° rear	45° front	60° rear	60° front	75° rear	75° front	
No wind	2.12		1.61		1.16		0.85		<b>1.38</b>
Calm, 5 m/s	2.06	2.19	1.58	1.70	1.13	1.21	0.87	0.89	<b>1.40</b>
Windy, 12 m/s	2.30	2.66	1.75	2.07	1.40	1.53	1.16	1.08	<b>1.69</b>

**Note:** RMS beam error in milestone = 2x RMS slope error

There is a single elevation angle (~60°) at which the facets and mirror support structure’s combined center of gravity is directly above the elevation pivot points. For all other elevation angles, gravity load will cause a global rotation of the facets about the elevation pivot axis. This rotation was calculated in the FEA model by iterating on an offset added to the linear actuator length until the RMS slope error was minimized. This offset is added to the nominal actuator length to minimize slope error. All optical error values in Table 28 are with the offset added to minimize slope error. If not included the no-wind field average RMS slope error increases 20%. The commercial SunRing controller will include these offsets.

*Impact of Thermal Expansion*

Table 29 presents the impact of changes in the heliostat temperature from its neutral (zero thermal load) temperature of 70°F on the overall RMS slope error. Temperature increases improve optics as they tend to make the facets concave which offsets the impact of gravity loads which make the facets convex. Temperature reductions increase optical error as they tend to make the facets convex and align with the impact of gravity loads.

Overall, the impacts (positive and negative) are relatively small, and they are not included in the final optical performance figures for the heliostat.

*Table 29 Optical Impact of Thermal Expansion*

Elevation Angle	Wind Speed	Wind Direction	Thermal Load	Change in RMS Slope Error Due to Thermal Load [mrad]
60°	Calm: 5m/s (11 mph)	Uplift	70°F → 131°F	-0.23
			70°F → 14°F	0.24
		Downforce	70°F → 131°F	-0.23
			70°F → 14°F	0.26
	Windy: 12m/s (27 mph)	Uplift	70°F → 131°F	-0.09
			70°F → 14°F	0.13
		Downforce	70°F → 131°F	-0.22
			70°F → 14°F	0.23

*Modal Analysis*

A modal analysis was performed to calculate the SunRing’s mode shapes and natural frequencies. Table 30 presents the natural frequencies for the first four modes, and it also shows that the heliostat’s elevation angle has a relatively small influence on its natural frequency.

*Table 30 Natural frequencies for modes 1-4*

Mode Number	Natural frequencies f [Hz] at Varying Elevation Angles			
	0°	30°	60°	90°
1	3.50	3.53	3.58	3.59
2	3.98	3.93	3.88	3.78
3	4.35	4.14	3.99	3.96
4	4.53	4.70	4.87	4.94

Wind loads can be broken down into the following three frequency ranges [8]:

- Mean spectrum: mean wind loads at < 0.5 Hz

- Gust spectrum: gust wind loads at ~ 1 Hz
- Vortex shedding: created by heliostat structure with frequency a function of wind speed and structure dimensions.

The SunRing’s natural frequencies are at least 3X higher than the mean and gust wind load spectrum; thus, no significant load amplification is expected from these wind loads. The vortex shedding frequency is predicted using the Strouhal number:

$$St = \frac{fL}{U}$$

Where:  $St$  = Strouhal number = 0.15 for flat plates with tilts of 10-90° [12]

$f$  = vortex frequency

$L$  = characteristic length = height of mirror facet x sin(elevation angle)

$U$  = wind speed

Figure 21 presents the predicted vortex shedding frequencies up to the SunRing’s maximum design wind speed at any orientation. The general trend is vortices are generated at higher frequencies as wind speed increases and elevation angle reduces. Vortices will approach the SunRing’s natural frequency at low elevation angles (< 10°) and at relatively low wind speeds. These two conditions result in relatively small loads on the heliostat, and the impact of dynamic load amplification is not expected to exceed the heliostat’s design wind loads. Further dynamic analysis is needed to verify these statements.

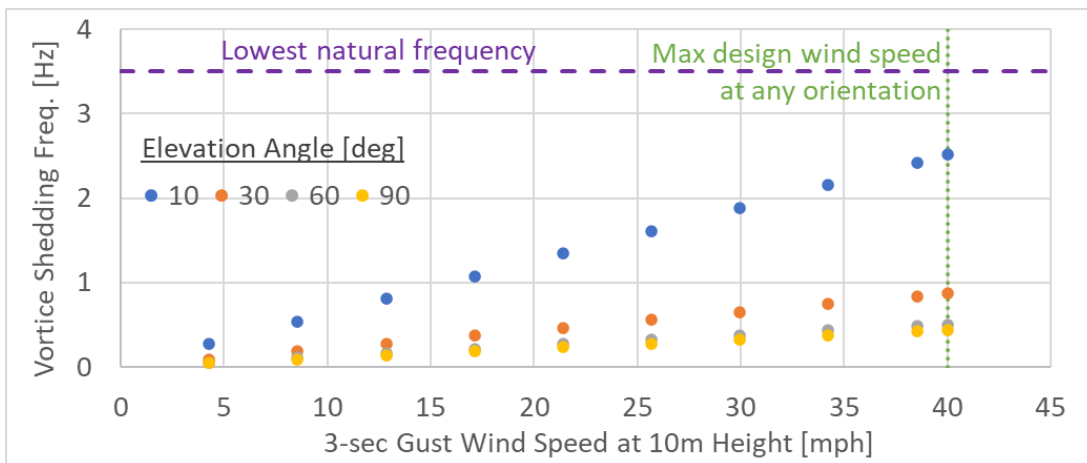


Figure 21 Heliostat induced vortex shedding frequency as function of wind speed and elevation angle

### 1.8.6 Total Installed Cost

The SunRing heliostat’s Class 2 total installed cost estimate is provided in Table 31.

**Note:** the majority of costs are in 2019 dollars; thus, the overall cost estimate is best viewed being in 2019\$.

*Table 31 Total installed cost breakdown*

Category	\$/m <sup>2</sup>	Source
Steel structure	\$19.5	\$1.65/kg cost basis based on 2019 quote from metal supplier for similar fabricated parts on Solar Dynamic's ATLAS project (DE-EE0007121).
Fasteners	\$3.2	Large volume quote from supplier.
Reflector	\$15.3	Supplier over the phone pricing for 4mm flat glass. (12.4 euro/m <sup>2</sup> )
Elevation Drive	\$5.8	Large volume quote from SAT Control.
Azimuth Drive – gearmotor	\$10.3	Large volume quote from supplier (includes shipping)
Azimuth Drive – geared track	\$2.7	Stamped track covering 180 degrees of Az drive, cost estimated as 50% of large volume quote for a waterjet fabricated gear segment.
Azimuth Drive – drive pinion, spring carriage, idler rollers, prox. sensor	\$5.3	Mixture of steel and aluminum parts using \$1.65/kg and \$3.3/kg, respectively unit costs and high quantity quotes.
Control	\$5.3	Level III controller: Cost estimate developed by Zebulon Solutions using scaled internet pricing and experience. Level II controller: Internet pricing. Level I controller: Allowance of \$0.25/m <sup>2</sup>
PV & battery	\$6.0	Volume quotes for PV panel and battery cells. Battery pack cost x 40% = cell cost (input from MPS)
Foundation	\$3.7	Large volume budgetary quote for ground screws from Chinese supplier.
Shipping	\$4.6	Structural steel: ArcelorMittal estimated 15% of material cost Mirrors, elevation drive, screw piles, controller, PV panel: based on \$2k/shipping container
Building and Tools	\$0.8	Bottoms-up cost estimate
A,I, CO labor	\$12.0	Bottoms-up cost estimate using \$35/hr labor
<b>Installed cost</b>	\$94.6	Estimate (total of component estimates)
	<b>\$96.3</b>	PERT-Beta Distribution: 68% probability

### 1.8.7 Optical Performance

The SunRing's total optical error breakdown is presented in Table 32. Structural deflection is the dominant error source, and the SunRing's measured performance exceeds FEA predictions. Achieving the FEA predicted level of performance is still obtainable, and the sources of high measured error are discussed in Section 1.14 on Full Scale Prototype Testing.

*Table 32 Total field average optical beam error [mrad]*

Component	Calm Conditions (5 m/s gust)	Windy Conditions (12 m/s gust)	Source
Reflector shape error	1.0	1.0	Conservative estimate, as flat glass should be relatively ideal in shape, supplier commented that errors would be small.
Canting error	0.28	0.28	Measured in BP3 while facets supported by canting jig using precision inclinometer (page 62).
Structural deflection (gravity + wind)	2.8 <b>4.74</b>	3.38 <b>7.74</b>	Black - FEA model results with final SunRing design, see Table 28 for details.  Red - Measured indoor Photogrammetry results used for Calm Conditions (Table 47), combined with measured increase in beam error due to wind loads for Windy Condition (page 74).
Tracking error	1.30	1.30	Results from BP3 tracking campaign (Table 50).
<b>Convolved total</b>	<b>3.26</b> <b>5.02</b>	<b>3.77</b> <b>7.92</b>	Convolved total of individual contributions  Black – with FEA structural deflection Red – with measured structural deflection

## 1.9 Assembly and Field Installation

The SunRing is installed in the field in two steps, first the pile foundations are installed followed by the remaining heliostat structure as detailed below.

### 1.9.1 Foundation Installation

The SunRing’s screw pile foundations are installed prior to attaching the heliostat structure. This relaxes the foundation installation schedule as foundations can be installed before the on-site heliostat assembly tent is erected. Foundation installation follows the following steps:

1. Pre-drill pilot hole for 6 x screw piles per heliostat
2. Drive 6 x screw piles per heliostat.

The cost basis for steps 1 and 2 are based on discussions with AP Alternatives (ground mount solar PV manufacturer and installer). AP Alternatives supplied the following typical installation rates:

- 120 holes pre-drilled per 2-man crew per day
- 120 piles installed per 1-man crew per day.

**Note:** These rates are based on rigs that install 1 pile at a time. A custom rig that simultaneously installs 6 piles would be less expensive including rig engineering and capital cost for large utility scale plants.

Meeting the baseline project’s 11-month foundation installation window requires 9 pre-drill and 9 pile driving crews working a single 8-hr shift per day. Table 33 presents the cost to pre-drill and drive the 6 x screw piles per heliostat.

*Table 33 Screw pile installation cost per heliostat*

Installation time [man-hrs]	1.73
Installation cost [\$]	\$60.38
Equipment cost <sup>1</sup> [\$]	\$22.50
Construction supervision cost <sup>2</sup> [\$]	\$4.58
Total cost [\$]	\$87.46
Total cost [\$ /m <sup>2</sup> ]	\$3.24

<sup>1</sup> Assuming \$50k per drilling and driving rig

<sup>2</sup> Assuming 2 supervisors at \$50/hr

### **1.9.2 Heliostat assembly**

The SunRing structure, drives, controller, and electrical connections are assembled in an on-site automotive style assembly line process. The assembly line unit operations (“OP”) are described in Table 34, and the assembly line flowchart is shown in Figure 22. The SunRing is assembled within an on-site tent at a rate of one SunRing every seven minutes.

After assembly, the heliostat is placed onto a field transportation trailer. Three heliostats are placed on each trailer before being transported close to their final installation location in the solar field. A telehandler or crane is then used to transport the heliostat from the trailer to the pre-installed set of screw piles. The foundation attachment tabs on the azimuth ring need to be aligned with the screw piles, and this is accomplished by connecting to the heliostat controller’s USB port and driving the azimuth drive which will rotate the azimuth ring as the heliostat structure is constrained by the telehandler. The heliostat is then lowered onto the screw piles and bolted into place. Finally, a field worker takes 10 minutes to measure initial tracking calibration parameters with a GPS, inclinometer, and digital compass.

Table 34 Heliostat assembly steps

OP #	Description
10	<b>Track and Mounts</b> Azimuth track placed on cart which moves heliostat through assembly stations. Anchor mounts and azimuth home flag installed.
20	<b>Base Triangle</b> Base struts are installed with hubs on azimuth track.
25	<b>Pre-Assembly: Hubs</b> Idler rollers installed into idler and drive hubs, moved to OP20 when complete.
26	<b>Pre-Assembly: Azimuth Drive</b> Azimuth drive is assembled, moved to OP20 when complete.
30	<b>Space Frame</b> The remaining lower support structure spanning from the hubs to the torque tube attachment points are installed.
40	<b>Torque Tube and Elevation Drive Installation</b> The torque tube and elevation actuator are installed onto the lower support structure.
45	<b>Pre-Assembly: Torque Tube</b> The two torque tube halves and elevation actuator arms are assembled. Elevation axis pivots (5x rod ends) installed, moved to OP40 when complete.
50	<b>Facet Install</b> Facets bolted to torque tube, facet alignment jig moved back to OP55.
55	<b>Facet Alignment &amp; Canting Brackets</b> Canting brackets installed on facets, and facets aligned to desired canting angles on facet alignment jig, jig with facets moved to OP50.
60	<b>Control &amp; PV Panel</b> PV panel and control box installed and all electrical connections made.
65	<b>Pre-Assembly: PV wiring &amp; mount attachment</b> PV mount and wiring installed to PV panel, moved to OP60.

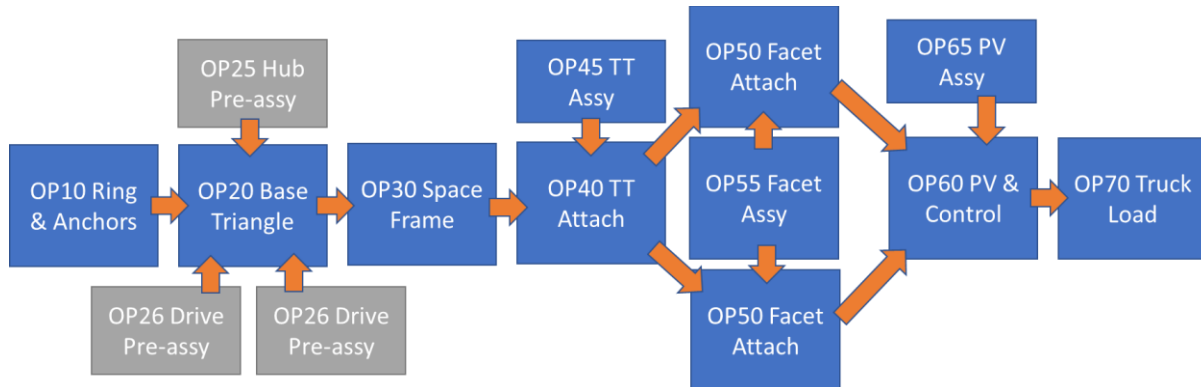


Figure 22 Heliostat assembly diagram

### Assembly Quality Control

Table 35 presents the quality control (QC) measures that would take place during heliostat assembly. The frequency of the first three measures would be variable starting with a high frequency and tapering off to a lower frequency as heliostat assembly becomes more consistent. The final heliostat slope error measurement is used to catalog each heliostat’s performance baseline when it leaves the tent.

*Table 35 Quality control steps during heliostat assembly*

QC Measure	Description	Suggested Frequency
Facet Alignment Jig	Canting angles of heliostat measured and compared to ideal values, jig adjusted to minimize difference.	Every $n^{\text{th}}$ heliostat.
Azimuth Drive	Rotate heliostat through full azimuth range of motion.	
Elevation Drive	Rotate heliostat through full azimuth range of motion.	
Heliostat Slope Error	Measure slope error of completed heliostat through deflectometry or similar methods.	Every heliostat.

**Note:** QC costs are not explicitly included in the SunRing’s assembly costs. There is a total of 0.4 man-hours of waiting time among all heliostat assembly workers, and this time could be used to perform the QC operations.

### Labor Rate

Work was performed to quantify the labor costs for the reference plant location (Harquahala Valley, Arizona) along with the Xinjiang and Qinghai regions in China where CSP plants are being built today. For an Arizona based site, the average all-in labor rate was determined to be \$35/hr using data from the US Bureau of Statistics. For a Chinese based project, the total all-in rate will be between the minimum wage of \$3.3/hr and the average wage of \$8.8/hr.

Manufacturing and operator labor hours utilize the \$35/hr rate, and staff labor hours use a \$50/hr rate in the final assembly cost.

### 1.9.3 Assembly and installation cost

A paper time study was completed for each unit operation in Table 34 and heliostat field installation. The assembly and installation cost of the SunRing heliostat excluding pile installation is \$9.60/m<sup>2</sup> as detailed in Table 36.

Adding in the pile installation cost, the total assembly and installation cost is **\$12.84/m<sup>2</sup>**.



*Table 36 SunRing assembly cost breakdown w/out screw pile installation*

		Description	Value
<b>Labor</b>		Manufacturing (man-hour/ heliostat)	4.32
		Operator (man-hour/ heliostat)	1.28
		Staff (man-hour/ heliostat)	0.70
		<b>Labor Total (\$/heliostat)</b>	<b>\$231.00</b>
<b>Infrastructure</b>		Tools (\$)	\$103,291
		Assembly Workstations (\$)	\$62,200
		Vehicles (\$)	\$196,000
		Factory Equipment (\$)	\$99,800
		Auxiliary (\$)	\$26,500
		Manufacturing Assembly Tent (\$)	\$397,066
		<b>Infrastructure Total (\$/heliostat)</b>	<b>\$22.12</b>
<b>Check-out</b>		Measure Tracking Parameters (man-hour/heliostat)	0.17
		<b>Checkout Total (\$/heliostat)</b>	<b>\$5.83</b>
<b>Total</b>	<b>Total of assembly/install steps</b>	<b>Total (\$/heliostat)</b>	<b>\$259</b>
		<b>Total (\$/m<sup>2</sup>)</b>	<b>\$9.60</b>
	<b>Using PERT-Beta Distribution: 68% probability</b>	<b>Total (\$/heliostat)</b>	<b>\$264</b>
		<b>Total (\$/m<sup>2</sup>)</b>	<b>\$9.78</b>

## 1.10 Commercial Outreach

The following details the Tech2Market activities performed throughout the project.

### 1.10.1 BP1- Industrial Advisory Board Initial Feedback

An Industrial Advisory Board (IAB) was created consisting of the following CSP professionals:

- Ryan Bowers – Advisian/Worley Parsons
- Paul Gauche – Sandia National Laboratories
- Bob Charles – Sargent and Lundy

A technical brochure on the Drop-C project along with a technical design presentation was created and distributed to the members of the board. A review meeting occurred in January 2019, and comments were collected and compiled. The main feedback from the IAB was:

- Ballast foundation has movement risks that need to be mitigated.
- Azimuth drive longevity needs to be proven out.
- Dynamic load analysis strongly encouraged.

These concerns were addressed in BP2 by the adoption of the screw pile foundation, lifetime testing of the azimuth drive, and the modal FEA analysis. Further lifetime testing and refined dynamic analysis are needed before the SunRing is commercialized.

**1.10.2 BP3 – Discussions with Potential Investor**

An IAB review was not held in BP2, as the SunRing prototype testing progressed slower than anticipated, and the IAB review was tentatively moved to early in BP3. Early in BP3, Solar Dynamics began discussions with a potential outside investor in the heliostat, and focus was shifted to support these discussions in leu of an IAB review of BP2 results.

The goal of external investment is to move the SunRing heliostat from a Technology Readiness Level (TRL) of 5 at the end of the DOE project to a bankable heliostat. Key takeaways from these discussions were:

1. One year of continuous operation at a national laboratory is desired.
  - a. Includes optical performance testing at start and end of operation period.
2. The heliostat needs to reach bankability in a period of 2 years to warrant investment.
3. The SunRing’s optical performance targets (4/5 beam mrad calm/windy) are high compared to commercial heliostats (3/4 mrad).
  - a. The SunRing’s smaller size and lower cost compared to conventional heliostats offset its poorer optical performance, but this tradeoff is not well known in industry. Optics will be improved on commercial design with additional mirror support braces described in the Path Forward section.

Based on the above feedback, an accelerated commercialization roadmap was created. The high-level summary of the roadmap is presented in Table 38 with total investment needs shown in Table 37. This schedule develops the SunRing into a commercial product within 2 years.

*Table 37 SunRing commercialization investment needed.*

Cost Category	Total Cost	
SD Labor	\$1,028,891	
3rd Party Engineering	\$356,095	
SolarTAC Hardware	\$26,720	
<b>Sandia Test: # heliostats tested</b>		
	1	4
Test services	\$143,415	\$280,559
Heliostat install + commissioning	\$95,200	\$201,600
<b>Subtotal</b>	<b>\$1,762,648</b>	<b>\$2,006,192</b>
<b>Indirects (15%)</b>	<b>\$264,397</b>	<b>\$300,929</b>
<b>Contingency(10%)</b>	<b>\$176,265</b>	<b>\$200,619</b>
<b>Total</b>	<b>\$2,203,310</b>	<b>\$2,507,740</b>

*Table 38 SunRing accelerated commercialization schedule.*

Activity	2022	2023	2024	
Continued outdoor testing at SolarTAC facility				<b>Milestone 1: Validated prototype performance. Q3/4 2022</b>
Finalize commercial heliostat engineering & analysis				
Key component accelerated lifetime testing				<b>Milestone 2: Achieve 30yr equivalent life. Q4 2023</b>
Complete control & communication design				
Construct & install heliostat at national laboratory (Sandia, PSA)				<b>Milestone 3: Begin testing at national lab. Q2 2023</b>
Performance testing at national laboratory				<b>Milestone 4: Bankable Drop-C heliostat. Q2 2024</b>

### **1.10.3 BP3 – Industrial Advisory Board Final Review**

A new set of IAB members were utilized due to combination of time constraints, retiring, and conflicts of interest with the original members. The final IAB consisted of:

- Mark Speir – Sandia National Laboratories (formerly worked for Solar Reserve)
- Kurt Drewes and Bruce Leslie – Vast Solar
- Bruce Kelly – Solar Dynamics

A technical presentation and accompanying questionnaire were distributed to the members of the board prior to a review meeting in July of 2022. The main feedback from the IAB was:

- Solar Dynamics should leverage existing expertise in roller design for the azimuth drive.
- Smart fabrication of facets themselves and canting for the facets can minimize slope error due to gravity loads. In other words, define the design such that the gravity loaded deformed structure approaches the optimum optical figure.
- Outdoor optical performance (i.e. slope error) under windy conditions is not well tested. FEA is the primary source of outdoor windy performance.
- Key overall metrics such as kg of structural steel / m<sup>2</sup> should be emphasized to show the SunRing's overall value compared against competition.

This feedback is being used to direct future SunRing development activities after the Drop-C project ends.

## 1.11 Azimuth Drive Lifetime Testing

The geared azimuth drive is one of the most novel features of the SunRing, and a robust testing campaign is needed to gain confidence that the design will survive the 30-year heliostat lifetime. Lifetime testing campaigns were carried out in both BP2 and BP3 with the goal of rotating the roller pinion through 30-years of equivalent travel.

### 1.11.1 Lifetime Testing: Budget Period 2

Lifetime testing in BP2 focused on testing the spring-loaded roller pinion / stamped gear design in a dusty environment. The test rig is shown in Figure 23.

The roller pinion is rotated at a constant 2.2 RPM clockwise and counter-clockwise, moving the gear track segment forward and backwards through its full length. This constitutes a single cycle. To reach the 30 years of equivalent heliostat life goal, the pinion rotates 531,760 revolutions or 110,783 cycles. Because the geared track is a partial arc of the full ring track, 30-years of track life occurs every 8,863 cycles.

Testing was unable to reach 30-years of equivalent life due to a failure in the non-commercial coupling between the gearmotor and the roller pinion's drive sprocket. Testing ended at 0.5 years of pinion life equal to 6.5 years of track life.

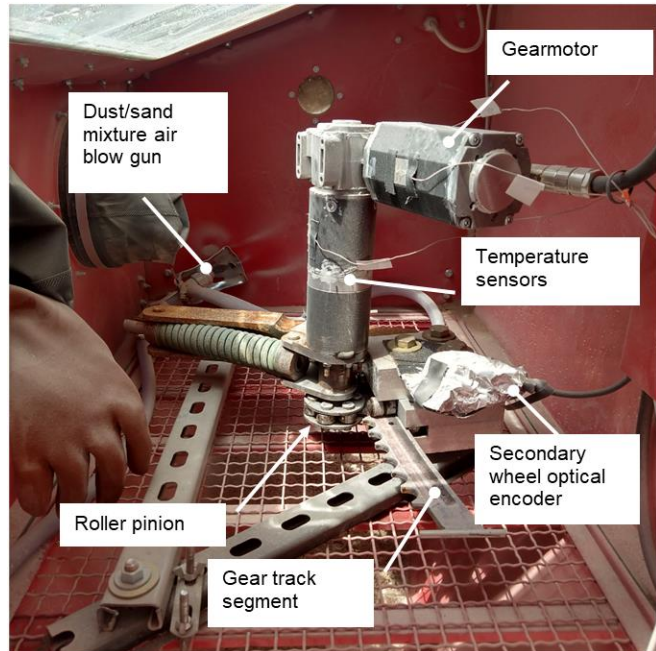


Figure 23 BP2 azimuth lifetime test stand

### *Geared Track Wear Test*

The geared track is designed to eliminate backlash between the track and pinion rollers by ensuring contact between a roller and two adjacent gear teeth. This is true if a clearance exists between the gear root and roller. This clearance can decrease with wear over time, and backlash will not be present if a clearance is present. The track to roller clearance was measured with calipers through the testing campaign with results presented in Figure 24.

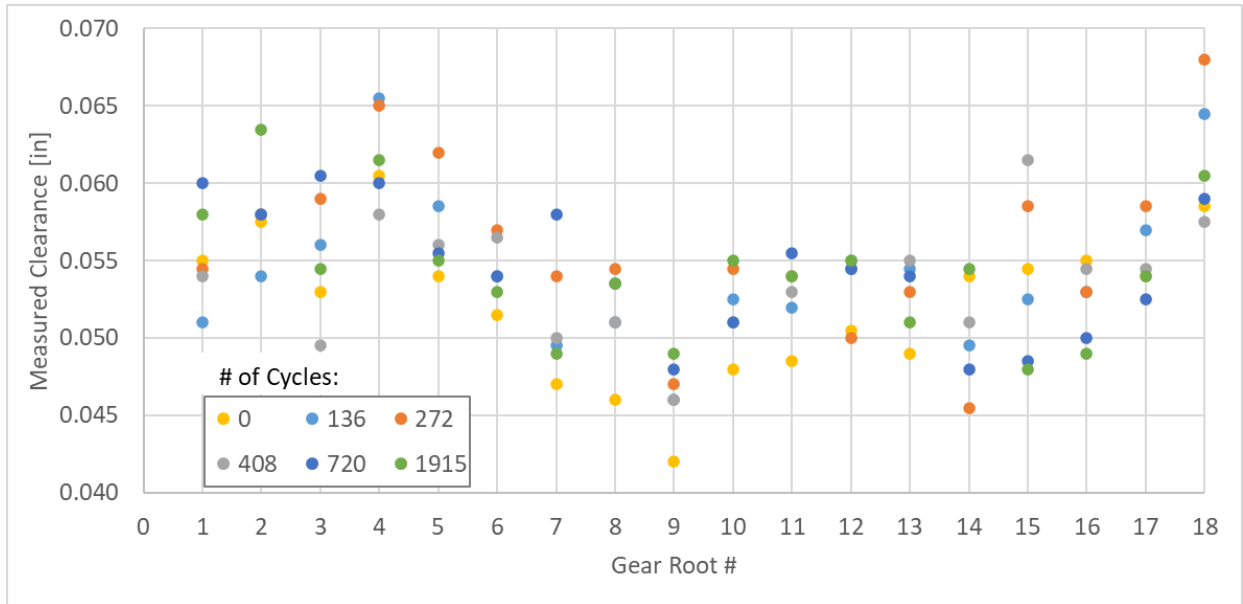


Figure 24 – BP2 Geared Azimuth Lifetime Test gear track wear plot.

With an estimated measurement uncertainty of 0.01 in, as of 1915 cycles (6.5 years equivalent track life), there is no clear decrease in measured clearance. This result indicates that the hardened steel gear track is a viable commercial track option.

#### Pinion roller wear test

The outer diameter of all 6 x rollers was measured throughout the test regime. With 1915 cycles (0.5 years equivalent roller life) to date, there is no indication of roller wear.

#### Pinion Roller Bushing Wear Test Results

After 720 cycles, cracks in the bushing flanges have developed. This was not expected based on published bushing specifications and is further discussed in the BP3 lifetime testing section.

#### Positional Accuracy Test Results

The positional accuracy test is based on ISO standard 230-2: Determination of Positioning Accuracy. This standard specifies test procedures to determine the accuracy and repeatability of positioning numerically controlled axes. For travel lengths less than 2 meters, the standard defines 5 target positions which are approached 5 times from both directions. The measured position of the pinion is compared to the actual target position. The external rotary encoder labeled in Figure 23 provides the true position basis.

Positional accuracy was translated to equivalent tracking error on the heliostat as presented in Figure 25. Tracking error is presented in terms of heliostat slope error where the goal is 0.5 mrad (1.0 mrad beam error from convolution of non-circular track, encoder resolution, and backlash error sources). The average tracking error stayed below 0.9 mrad until backlash developed in the system.

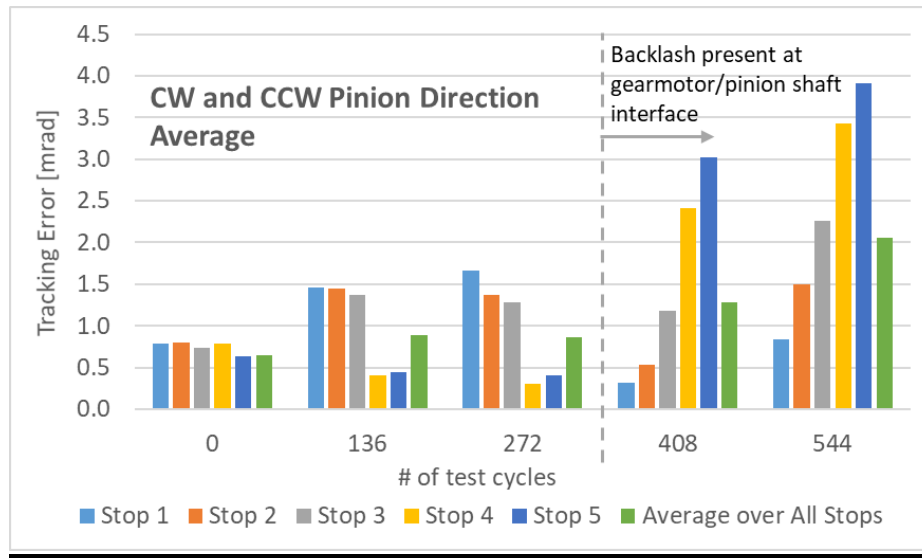


Figure 25 Lifetime azimuth drive positional accuracy results

*Commercial design changes*

Table 39 presents the recommended design changes prompted by results of this testing and if they were achieved in the final BP3 design.

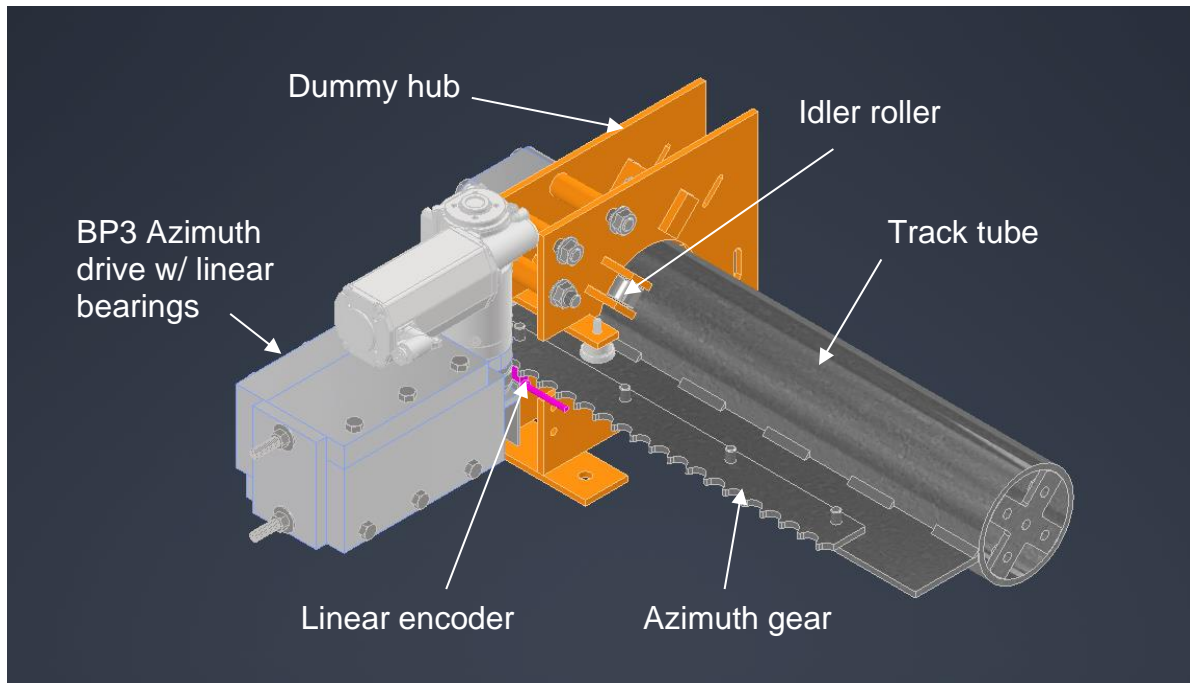
Table 39 Azimuth drive changes resulting from lifetime testing

Component	Design Change	Achieved on BP3 Heliostat
Gearbox output shaft	Work with gearbox manufacturer(s) to develop a custom output shaft design to eliminate backlash at shaft interface.	Yes
Drive hub	Center spring force about the roller pinion & track to keep pinion planar to geared track.	Yes
Spring force	Reduce required spring force by reacting portion of wind Mz load outside of drive pinion.	No, conceptual Mz brake design found to be unviable.
Bushings	Discuss bushing failures with manufacturer and determine viability for future use.	Bushings continued to be issue in BP3 design.

**1.11.2 Lifetime Testing: Budget Period 3**

Lifetime testing in BP3 extended the scope to include the idler roller/tubular track interface in addition to the spring-loaded roller pinion / stamped gear. Due to the early bushing failures in BP2, BP3 testing started without dust being introduced to the test chamber. A 3D model of the new test fixture is shown in Figure 26. A linear track tube and azimuth gear are used in place of the circular azimuth track in order to fit into the

chamber. A linear encoder is included to quantify any changes in azimuth tracking accuracy over the lifetime of the heliostat.



*Figure 26 Azimuth Accelerated Lifetime Test Fixture*

Evaluating wear on the idler and drive sprocket rollers, the gear tooth surfaces, and the track tube surface is of particular importance since surface fatigue is the most likely failure mode of these components. Analytical evaluation of surface fatigue, especially in dusty environments, is not well covered by engineering literature, so direct evaluation in a representative environment is critical. The test design allows the gear plate, track tube, and rollers to be easily replaced so that multiple material options can be evaluated. BP3 testing focused initially on a low-cost, higher-risk combination: carbon steel rollers without heat treatment, galvanized carbon steel track tube, and a galvanized hardened steel plate gear.

With the same cycle definition as BP2 testing, the BP2 test rig requires 101,636 and 8,863 cycles to reach 30 years of equivalent heliostat life on the roller pinion and azimuth tracks (geared and tubular), respectively.


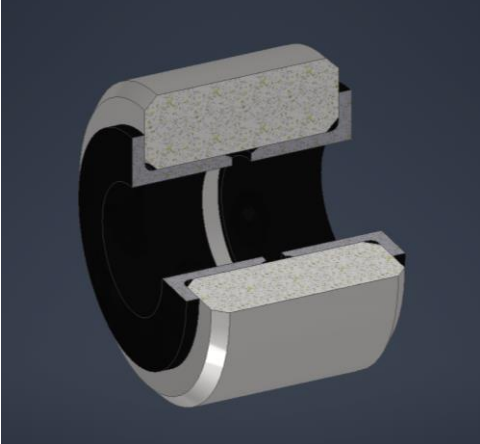
#### *Pinion Roller Bushing Failures*

The lifetime testing was performed with carbon steel drive pinion rollers with plastic plain bearings. Specialty plastic bearings were selected that have a much higher static pressure capacity than oil-impregnated bronze bearings. A higher allowable pressure enables the shaft and roller diameter to be minimized, which reduces the required diameter of the drive sprocket and the holding torque of the azimuth gearmotor. The rollers used on the azimuth test had an outside diameter (OD) of  $\frac{3}{4}$ -inch and run on a  $\frac{5}{16}$ -inch shaft. These rollers match the OD of the commercial-off-the-shelf roller-bearing cam followers that were used on the 2<sup>nd</sup> heliostat prototype. The custom rollers and plain bearings do not require lubrication and are lower cost than the cam followers. The plain bearings must be run at a lower speed and have a higher wear rate, but

neither is an issue for the heliostat since its tracking speed is slow and the total lifetime travel of the rollers is relatively low.

Table 40 compares the roller cam followers and the custom plain bearing rollers.

*Table 40 Roller Cam Follower vs BP3 Lifetime Test Roller*

Roller-Bearing Cam Follower	BP3 Lifetime Test Plain Bearing Roller
	
<ul style="list-style-type: none"> <li>• Roller bearings</li> <li>• Hardened steel housing and inner race</li> <li>• Lubricated</li> <li>• Seals used to contain lubrication</li> <li>• \$15-20 low-volume cost</li> </ul>	<ul style="list-style-type: none"> <li>• Plain bearing, runs on ground internal shaft (not shown)</li> <li>• Carbon steel roller w/out heat treatment</li> <li>• Hard chrome plating for corrosion resistance</li> <li>• Lubrication-free operation w/ plastic bushings</li> <li>• Bushings &lt;\$.80 each low-volume cost</li> <li>• Roller &lt;\$1 at commercial volume</li> </ul>

The plain bearings were designed with a load safety factor of 1.2, and it was anticipated that wear against the internal shaft would be the limiting factor on their service life. However, the lifetime testing resulted in pre-mature failures of the bushings due to crack propagation beginning at the top inside corner of the bearings and ultimately splitting the bearings, as shown in Figure 27. Failures were observed early at cycle 270 after which testing was stopped due to schedule and budget constraints. The same failure was observed on multiple rollers. The bushings were also tested against multiple shaft sizes and surface finishes, but no combination had a meaningful impact on the bushing life.



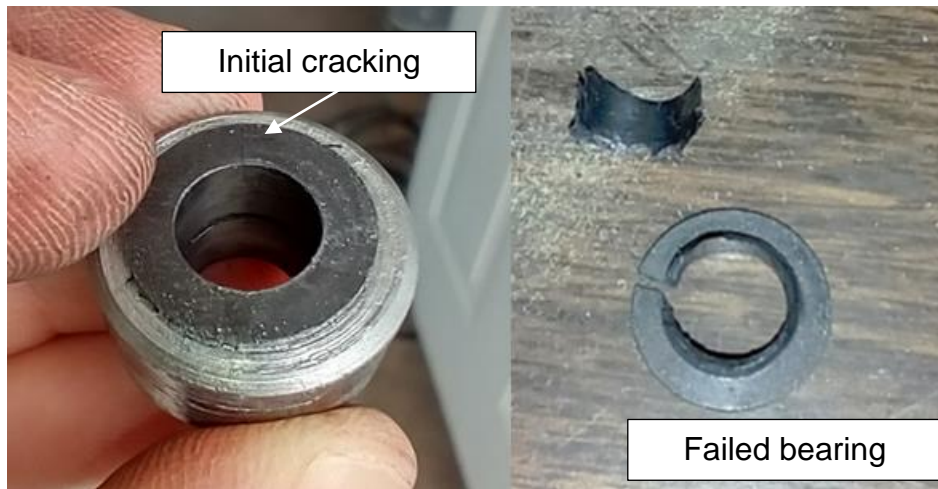


Figure 27 Drive Roller Plain Bearing Failure

The most likely cause of this failure is un-even load distribution on the drive rollers due to their rotation axis being mis-aligned with the geared tooth profile. The misalignment is caused by a combination of the taper of the waterjet cut tooth profile (due to the natural spread of the water jet as it passed through the material) and misalignment of the track and gear due to manufacturing tolerance. The angular offset between the roller and the gear creates a moment in the roller that results in a stress concentration at the top and bottom edges of the roller.

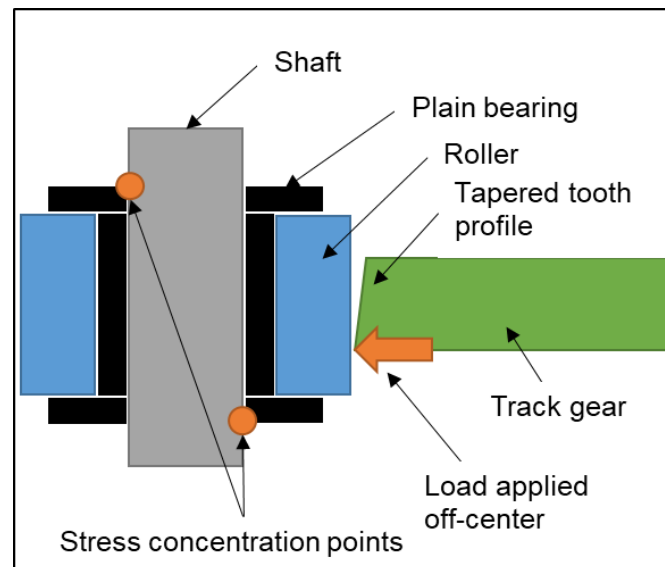


Figure 28 Plain Bearing Stress Concentration

This was anticipated, but it was believed that the compliance of the plastic bearing material would be sufficient to accommodate the small amount of misalignment. However, in practice the bushing material has very limited compliance and tended to crack rather than elastically deform. Figure 28 illustrates the issue.

This issue was not observed in the BP2 heliostat when using the roller bearing cam followers for two reasons. First, the cam followers are slightly crowned on their outer diameter, which reduces the impact of misalignment between the follower and the mating part. Second, the cam followers have a rated load more than twice that of the plain bearings, so increased stress would not necessarily result in failure.

For future development (outside of this project), Solar Dynamics anticipates working with a cam follower manufacturer to develop a custom solution for this application. The anticipated commercial design will match the size and function of the cam follower used in the BP2 prototype with two customized features:

1. A solid lubricant or long-life grease will be used in place of the standard lubricant to allow maintenance-free operation over the full heliostat lifetime. Cam followers with solid lubricant are commercially available, but do not match the size of the current drive pinion rollers. Either a custom roller will need to be developed, or the size of the gear and drive sprocket will need to be adjusted to accommodate the commercially available options.
2. A hard-chrome or other surface finish will be used to limit corrosion of the cam followers. Commercially available cam followers are either bare steel (suitable for low-moisture or oiled environments) or stainless steel for high corrosion environments. Stainless steel is not preferable for the heliostat due to its higher cost and lower load capacity than carbon steel.

The cost impact of using roller cam followers is not fully understood since the combination of customization but high volume will have an unknown effect on the final cost. However, an upper bound of \$2.75/m<sup>2</sup> can be established based on the difference between the low-volume cost of the BP2 cam follower (\$15 each) and the anticipated commercial cost of the plain bearing design (\$2.60 each) for the six drive rollers.

#### *Geared Track Wear Test*

A galvanized tubular track was used in BP2 unlike the plain steel track in BP2. The galvanization zinc layer was removed between the test start and cycle 270 when the bearing failures above caused the test to stop. Based on BP2 results, no further wear is expected.

#### *Pinion roller wear test*

Similar to BP2 testing, no signs of roller wear were noticed during the short 270 cycle BP3 lifetime test.

#### *Positional Accuracy Test Results*

As in BP2, positional accuracy was translated to equivalent tracking error on the heliostat as presented in Figure 29. Tracking error remained relatively consistent with an average of 0.80 mrad over the short test window which is not far from the 0.5 mrad goal. Slop in the test stand contributes to tracking error and will not be present on the heliostat.

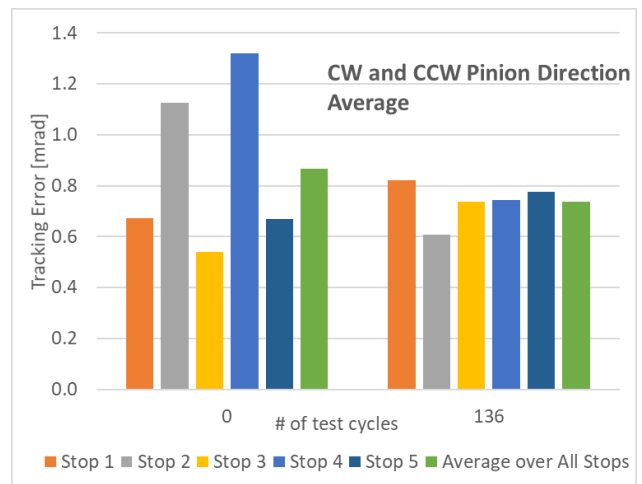


Figure 29 BP3 lifetime azimuth drive positional accuracy

## 1.12 Elevation Drive Lifetime Testing

The main goal of elevation drive testing is to quantify the increase in backlash over the 30 years of heliostat travel. Backlash growth is primarily a function of wear at the nut/screw interface in the Acme screw based linear actuator. Wear is proportional to the product of speed and load. The load on the actuator in service is a function of elevation angle and wind speed/direction. A histogram of mean wind speeds for a

potential Arizona commercial site was used to inform the percentage of cycles to perform at each wind speed. The resulting load profiles are shown in Figure 30.

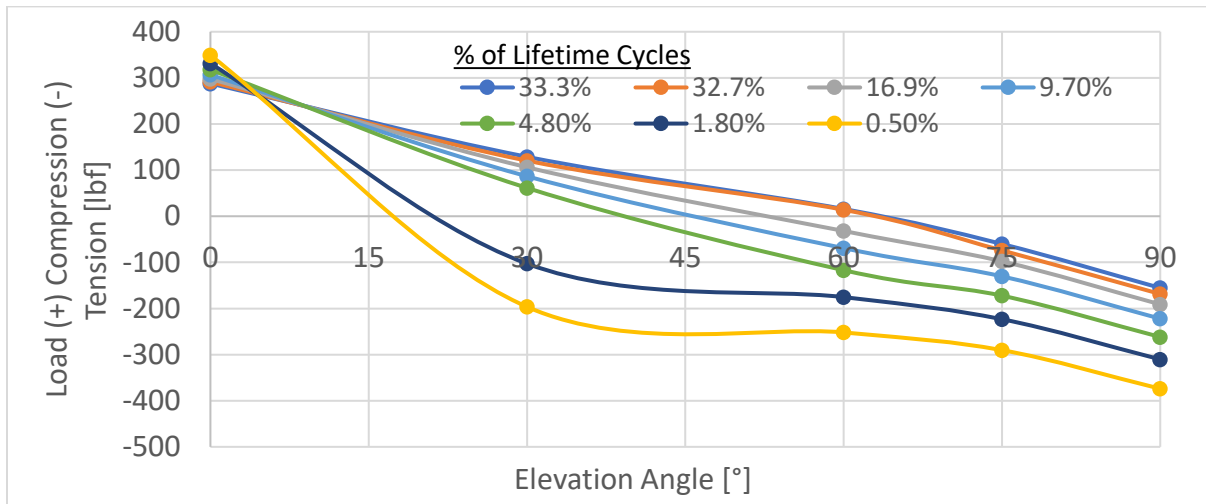


Figure 30 Elevation actuator loads during lifetime testing

The test stand used to apply the variable load above is shown in Figure 31. The linear actuator is coupled to an air cylinder which moves on a linear track. An automated control valve regulates air cylinder pressure such that the load on the actuator measured by a load cell matches the profiles above. The test stand includes a linear magnetic encoder that enables accurate backlash measurements along the actuator's full stroke.

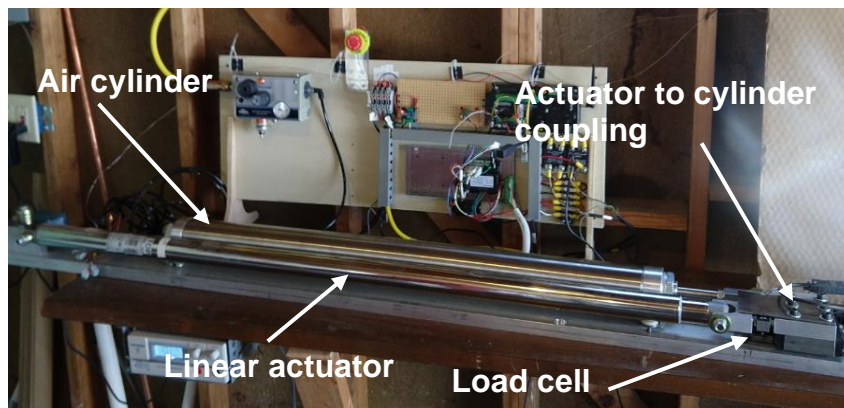


Figure 31 Elevation drive lifetime test stand

Figure 32 presents the backlash averaged over the actuators stroke during the BP2 test campaign. The test was paused at 17 years of equivalent heliostat life because the actuator under testing was needed for the SunRing outdoor heliostat prototype. Backlash was relatively stable at 0.024 inches until the last measurement of 0.027 inches was recorded. The current lifetime average is 0.023 inches which is acceptable, but further testing was not possible due to procurement delays of additional actuators.

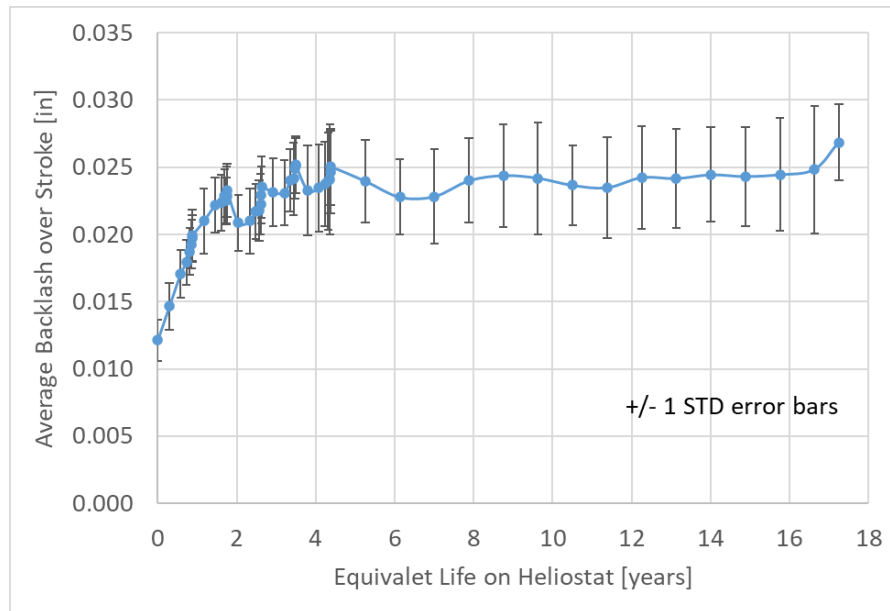


Figure 32 Elevation drive lifetime backlash test results

### 1.13 Battery Testing

The goal of battery testing was to quantify the expected capacity loss per battery cycle [mAh/cycle] at the combinations of the following independent variables:

- Depth of discharge (DoD): 20,40, and 80%
  - 20-40% represent typical daily DoD on heliostat
  - 80% represents DoD for a worst-case high wind stow event
- Ambient temperatures: 80, 122, 140°F
  - 80°F represents average annual control box internal temperature
  - 122°F maximum ambient temperature for reference AZ site and maximum charging temperature for LTO battery
  - 140°F maximum charging/discharging temperature for A123 battery

Testing was performed by Mobile Power Solutions (MPS) on the three different battery cells, one Lithium Titanate Oxide (LTO) and two Lithium Iron Phosphate (LiFePO<sub>4</sub>). The test was to continue until battery capacity reached 80% of new capacity or until linear trends of capacity loss per cycle were reached. There were several testing challenges. First, testing requires long test periods due to battery cell current limits specified by manufactures to protect lifetime. Second, the small capacity loss at non-extreme conditions (i.e. 80°F and 20-40% DoD) makes capacity loss measurement difficult without performing many cycles (which increases test period). After three months of testing, the average battery capacity dropped to 91% of new, and the testing was paused due to budget constraints. Table 41 presents the number of expected cycles at each condition to reach 80% of new capacity. There are relatively large error bars around the data, but the general trends are as expected with decreased cycle life as temperature and DoD increase.

Table 41 Lifetime battery testing results

Ambient Temperature	Depth of Discharge	Estimated # of Cycles to Reach 80% of New Capacity (Vendor Spec in Red)		
		Vendor: LTO Type: LTO	Vendor: A123 Type: LiFePO <sub>4</sub>	Vendor: K2 Type: LiFePO <sub>4</sub>
80°F	80%	2,874 (>10k)	2,502 (> 7k)	1,743 (> 2k)
	40%	2,429	8,424	7,108
	20%	4,489	11,759	15,133
122°F	80%	1,737	1,941	305
	40%	715	2,343	1,920
	20%	Bad Data	Bad Data	3,279
140°F	80%	147	92	151
	40%	289	1,204	620
	20%	2,045	1,517	2,479

From historical 1-min wind speed data of a representative AZ project site, it was found that an average of 50 high wind stow events (80% DoD events) occur annually for a total of 1,500 events over the 30-year life. This is in addition to the 365x30 = 10,950 typical daily cycles (20-40% DoD events) in the heliostat lifetime. Table 42 presents the expected battery lifetime based on this distribution of cycles. The SunRing baseline assumes K2 LeFePO<sub>4</sub> battery cells with 2 scheduled lifetime replacements.

Table 42 Expected battery lifetime

Typical Daily Cycle DoD	Expected Lifetime [years]		
	LTO	A123	K2
20%	5.4	9.3	9.3
40%	3.4	8.3	6.1

\*Assumes 80% cycles at 80°F, 15% at 122°F, 5% at 140°F

### 1.14 Full Scale Prototype Testing

Three full-scale SunRing heliostats were built within the project as outlined in Table 43. The following sections detail the testing results on each.

Table 43 Heliostat prototype builds

Prototype #	Heliostat Design	Tests Performed
1	BP2 final design	<ul style="list-style-type: none"> <li>Structural</li> </ul>
2	BP2 final design	<ul style="list-style-type: none"> <li>Indoor optical assessment</li> <li>Outdoor tracking</li> </ul>
2a	BP2 final design w/ BP3 azimuth drive carriage	<ul style="list-style-type: none"> <li>Outdoor tracking</li> </ul>
3	BP3 final design	<ul style="list-style-type: none"> <li>Indoor optical assessment</li> <li>Outdoor optical assessment</li> <li>Outdoor tracking</li> </ul>

### 1.14.1 Structural Testing

The 1<sup>st</sup> SunRing prototype was constructed solely for structural testing. The objective was to subject the heliostat to its maximum design loads to ensure no failures occurred in the structure. There is not a single orientation and wind direction that subjects all components to their maximum loads; thus, a test rig was constructed that allowed loading the heliostat at multiple elevation angles and simulated wind loads into the rear or front of the heliostat.

Figure 33 presents the load fixture which encases the entire heliostat with exception to the glass facets which are replaced with equal weight steel plates. A cantilever arm is attached to each plate with a load point above and below the torque tube allowing the application of moment and axial loads that matched those applied in the FEA model.

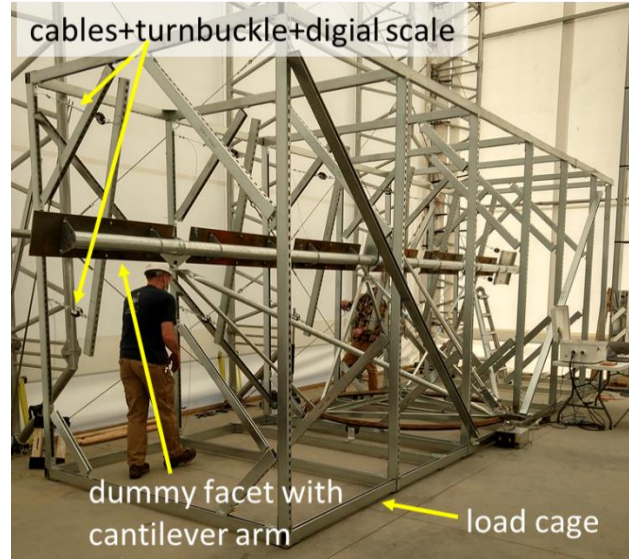


Figure 33 Structural load test fixture

A total of 14 load points [2 x (6 facets + 1 PV panel)] were applied through a set of cables, a turnbuckle, and a digital load scale at each load point. The compliance in the heliostat structure and stretch in the cables required repeated adjustment of each load point until loads settled near the goal magnitudes. Table 44 presents the achieved vs goal overall loads for the three load cases simulated which produce the highest AISC load ratios. No component failures or movement in joints were observed yielding a successful load test.

Table 44 Structural load test achieved loads

Load Case	Achieved Load (% of Goal)			
	Fx [lbf]	Fz [lbf]	My [lbf-ft]	Mz [lbf-ft]
75 Max Mz Front	1,801 (101%)	483 (101%)	417 (96%)	6,663 (90%)
75 Max Mz Rear	-1,759 (99%)	-471 (99%)	-388 (89%)	-6,673 (90%)
90 Max Mz Rear	-1,243 (100%)	-333 (100%)	-480 (68%)	-6,668 (98%)

Strain gauges were installed with the intent on comparing stress values to FEA predictions; however, strain measurements were inconsistent, and this comparison was not realized. This was likely due to inexperience in using strain gauges and not discrepancy between the test and the FEA model.

### 1.14.2 Indoor Optical Testing

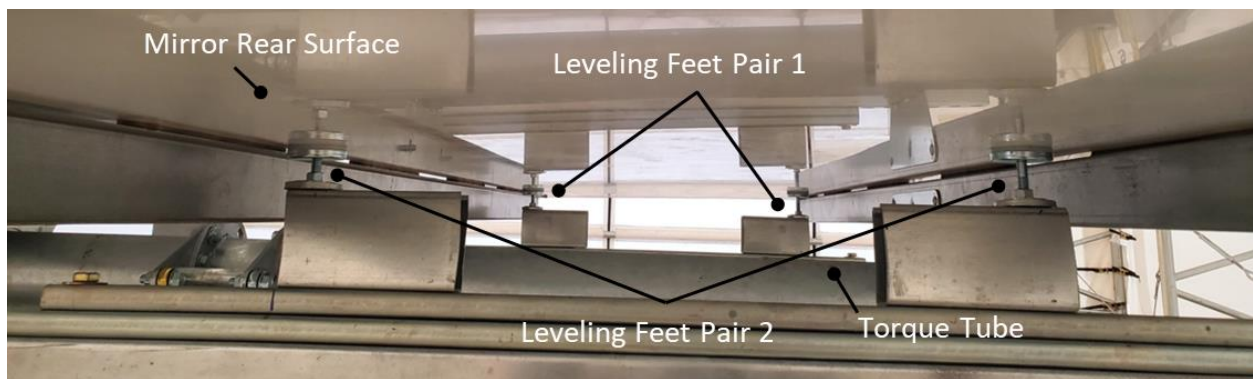
Both the 2<sup>nd</sup> and 3<sup>rd</sup> SunRing prototypes were first installed indoors for optical testing following the SolarPaces Guideline for Heliostat Performance Testing [17]. Indoors the SunRing is subjected to both gravity and thermal expansion loads.

**Note:** The facets are numbered in order starting with facet #1 at the PV panel.

### *Mirror Alignment*

The commercial SunRing uses an assembly jig to precisely align the mirror facets when installing onto the torque tube (TT). A commercial intent jig was prototyped for the 3<sup>rd</sup> SunRing as shown in Figure 34. The mirror alignment process is summarized here:

1. Move/roll the SunRing's lower support structure plus TT into the jig
2. Loosely bolt each mirror facet onto the TT
3. Precisely align each mirror to desired canting angle using at least 4 leveling feet supporting each mirror facet.
4. Securely fasten mirror facet to TT via bolted connection at canting brackets.



*Figure 34 Close-up of one facet on canting jig*

For the 3<sup>rd</sup> SunRing prototype, Step #3 was performed manually with a precision digital inclinometer. The 2 x pairs of leveling feet (1 pair above and 1 pair below the TT) were adjusted until the canting angle at both the upper and lower mirror edges agreed with a maximum deviation of 0.18 mrad. The resulting canting error with the facets bolted to the TT but still supported by the leveling feet was 0.14 mrad (slope basis). This meets the canting error budget of 0.5 mrad (slope basis).

### *Optical Error due to Gravity and Thermal Expansion*

Photogrammetry (PG) was used to quantify optical error due to gravity and thermal expansion loads. A grid of 3,024 retroreflective targets were placed on the glass surface of the facets yielding a density of 112 targets/m<sup>2</sup> which meets the SolarPACES guideline of  $\geq 100$  targets/m<sup>2</sup>. PG yields a 3D point cloud of the targets. PG was performed over a range of heliostat orientations and structure temperatures.

Optical error can be broken down into two categories: global facet rotation and local deformation induced slope error on the facet. Both were measured as discussed below.

### *Facet Rotation Error*

Facet rotation error is calculated by finding the best fit plane for each facet and comparing its normal vector to the facet's ideal normal vector. Facet rotation error includes any canting error introduced when facets are installed plus rotation caused by external loads on the heliostat.

The 2<sup>nd</sup> SunRing prototype results are compared against FEA predictions in Table 45. Measured facet rotation error is lowest at 0° where facets were aligned and installed on the TT. Measured facet rotation error increases at higher elevation errors which is inverse of the predicted FEA performance. This was attributed to longitudinal slop in the elevation pivot bearings, and this was addressed in the 3<sup>rd</sup> SunRing prototype by adopting rod-end type bearings as shown in Figure 35.

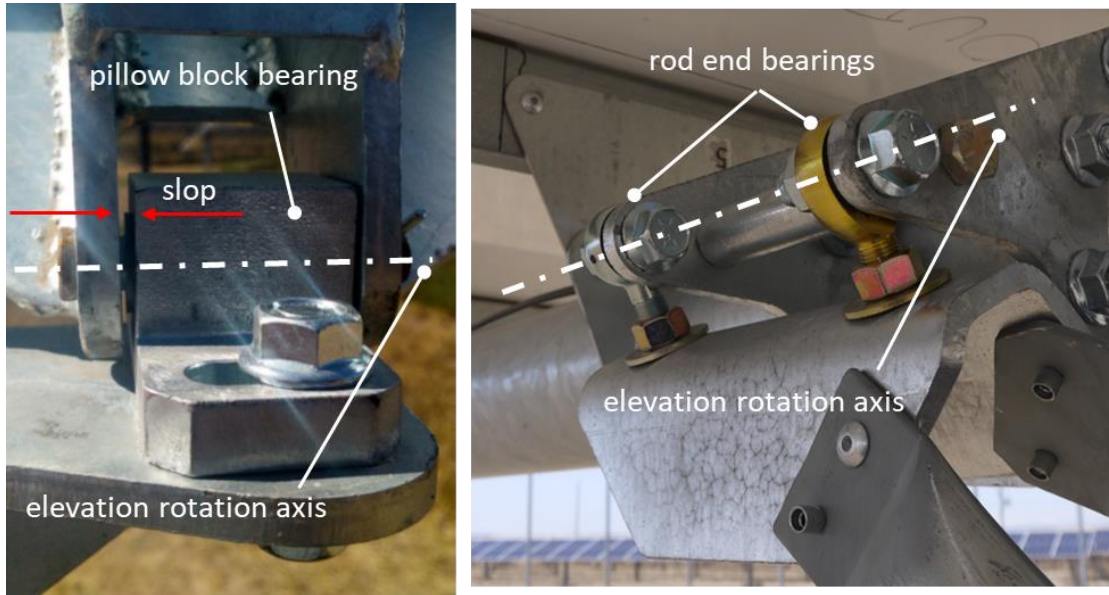


Figure 35 Elevation axis pivot bearings, 2<sup>nd</sup> SunRing prototype (left) and 3<sup>rd</sup> SunRing prototype (right)

Table 45 2<sup>nd</sup> Prototype: Measured vs FEA predicted facet rotation error (slope basis)

Elevation Angle [°]		0	30	45	60	75	90	Annual Energy Weighted Avg
Avg. Rotation Error [mrad]	FEA Model	1.2	0.7	No Data	0.3	0.7	0.4	0.5
	Measured w/ Alignment at 0°	1.2	1.9	2.7	3.7	4.6	5.4	3.3

\*At azimuth angle = 0° and T<sub>low</sub> average = 67.7°F

The 3<sup>rd</sup> SunRing prototype exhibited more favorable results as shown in Table 46. There is very good agreement at 0 and 30°. The measured error at 90° is higher than expected but likely not a cause for concern when factoring in the uncertainty of the PG measurements.

Table 46 3<sup>rd</sup> Prototype: Measured vs FEA predicted facet rotation error (slope basis)

Elevation Angle [°]		0	30	60	75	90
Avg. Rotation Error [mrad]	FEA Model	1.29	0.84	0.33	0.44	0.75
	Measured	1.31	0.86	0.68	0.77	1.07



It is possible to minimize facet rotation error by setting the facets' canting angles to compensate for gravity induced facet rotation. The canting angles on the canting jig would be set such that the gravity deformed structure yields ideal canting angles. This requires open loop feedback between PG and facet canting to set up the canting jig. While not realized during the Drop-C project, the optical benefits of this outweigh the setup cost on a commercial scale.

Lastly, facet rotation error was found to be insensitive to azimuth angle and ambient temperature as a maximum difference of 0.06 mrad was found between the different conditions on the 2<sup>nd</sup> SunRing prototype which is within the error bounds of the PG analysis.

### Local Slope Error

Calculating slope error requires further post processing of the 3D PG point cloud. The point cloud was triangulated to create surfaces from which normal vectors are derived. Slope error is the angle between each triangulated surface's normal and the normal for each facet's best fit plane.

Figure 36 presents the measured slope error on the 2<sup>nd</sup> SunRing prototype at difference combinations of elevation angle, azimuth angle, and temperature. There is little change in slope error with azimuth position and temperature. The largest change in slope error with temperature is 0.2 mrad with the average being 0.1 mrad. The elevation angle does have a marked impact as shown in both measured and FEA predictions.

The high slope error at high elevation angles was thought to be due to the twist imparted into the facet when installing onto the torque tube as a commercial intent facet alignment jig was not used for the 2<sup>nd</sup> SunRing prototype. However, this high slope error is again present on the 3<sup>rd</sup> SunRing prototype which used the commercial intent jig. The 3<sup>rd</sup> SunRing prototype results are shown in Figure 37.

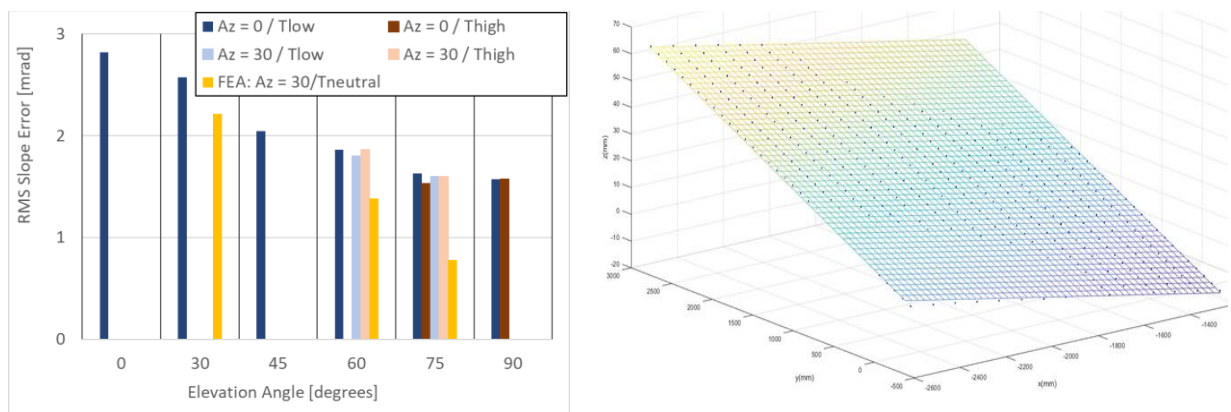


Figure 36 2<sup>nd</sup> Prototype: Measured facet slope error (left) and facet #2 point cloud with fitted plan (right)<sup>1,2</sup>

<sup>1</sup> Tlow average = 68°F, Thigh average = 84°F

<sup>2</sup> FEA results include convolution of 0.5 mrad mirror slope error

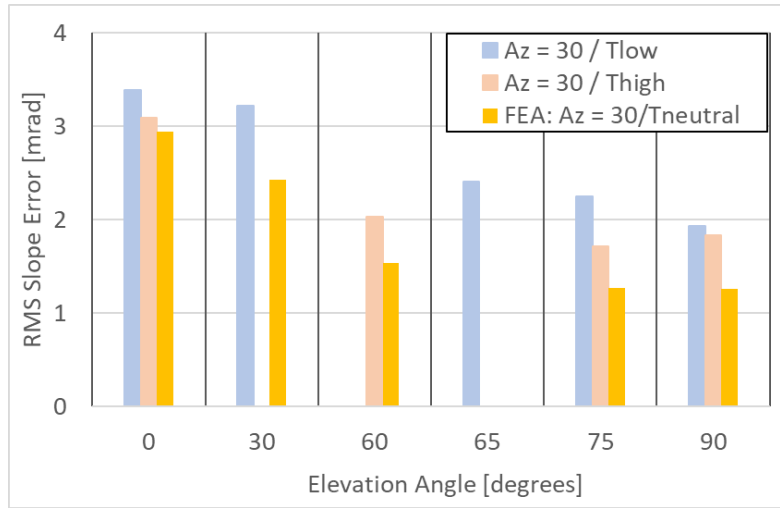


Figure 37 3<sup>rd</sup> Prototype: Measured facet slope error compared to FEA <sup>2, 3</sup>

Reviewing the PG point cloud shows that the measured mirror facets consistently have a “hump” at their center. The source(s) of high slope error at high elevation angles is believed to be:

- The adhesive could be more flexible than what FEA predicts, or the variable height of the glue beads could allow more “shear” movement between the mirror and the rib.
  - Next step: run parametric study on adhesive properties in FEA model
- The ribs could consistently be wider than the mounting flanges on the torque tube, which would tend to pull the ribs “in” and try to bow the mirror.
  - Next step: precision measurement of rib spacing and TT flange spacing, will require removal of the facet to perform.

### Total Error

The total optical error due to gravity loads is summarized Table 47. The total slope error is higher than FEA predictions because of the high local slope error described above.

Table 47 3<sup>rd</sup> Prototype: Measured total slope error due to gravity loads.

Elevation Angle [°]		0	30	45	60	75	90	Annual Energy Weighted AVG
Total Slope Error [mrad]	FEA Model <sup>1</sup>	3.71	2.12	1.61	1.16	0.85	Not Calculated	1.38
	Measured <sup>2</sup>	3.40	3.24	Not Measured	2.05	2.28	1.87	2.37

<sup>1</sup> Convolved with 0.5 mrad mirror slope error

<sup>2</sup> At azimuth angle = 30° and Taverage = 42°F

<sup>3</sup> Tlow average = 34°F, Thigh average = 55°F

### 1.14.3 Outdoor Optical Testing

#### Installation Location and Targets

The 2<sup>nd</sup> and 3<sup>rd</sup> heliostat prototypes were installed outdoors for on-sun testing where the heliostats tracked an aimpoint on a target. The heliostats were installed in different locations as detailed in Table 48.

Table 48 Outdoor heliostat installation locations

Heliostat Prototype	Heliostat Location Relative to Aimpoint		
	North/South <sup>1</sup>	West/East <sup>1</sup>	Vertical <sup>2</sup>
2	3.6 ft S	116 ft W	0.6 ft above
2a and 3	224.3 ft N	2.7 ft E	5.9 ft below

<sup>1</sup>To center of azimuth track, <sup>2</sup>To center of mirror surface

Different targets were also used for each heliostat prototype. The 2<sup>nd</sup> prototype utilized a relatively small 44 x 44 inch target which was solely intended to be used for tracking accuracy testing. The 3<sup>rd</sup> prototype utilized a larger 16 ft wide x 20 ft tall target which was able to capture the full projected sun image which allowed for both tracking accuracy and image quality testing. Both targets are shown in Figure 38.

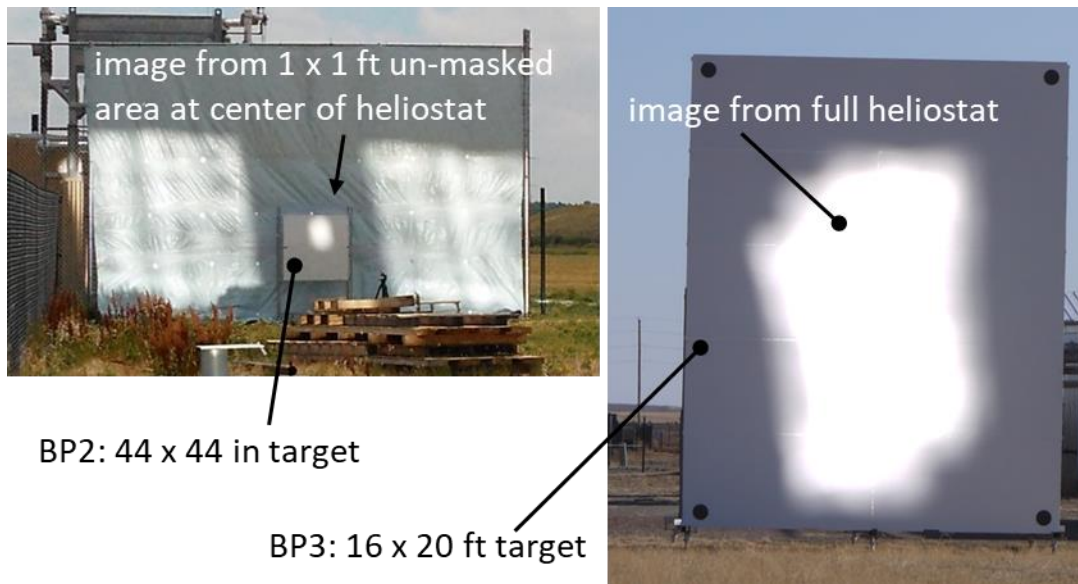


Figure 38 Outdoor targets, BP2 target for 2<sup>nd</sup> prototype (left) / BP3 target for 3<sup>rd</sup> prototype (right)

#### Image Characterization and Remote Operation Station

A Matlab developed algorithm in conjunction with a machine vision camera is used to characterize the heliostat's image on the target. Both the centroid of the image and the area containing a specified % of total image power are calculated. The laptop which runs the image characterization is housed in an industrial cabinet installed approximately midway between the target and the heliostat. The laptop also enables off-site operation and monitoring of the heliostat and imaging characterization system. A schematic of the communication system is shown in Figure 39

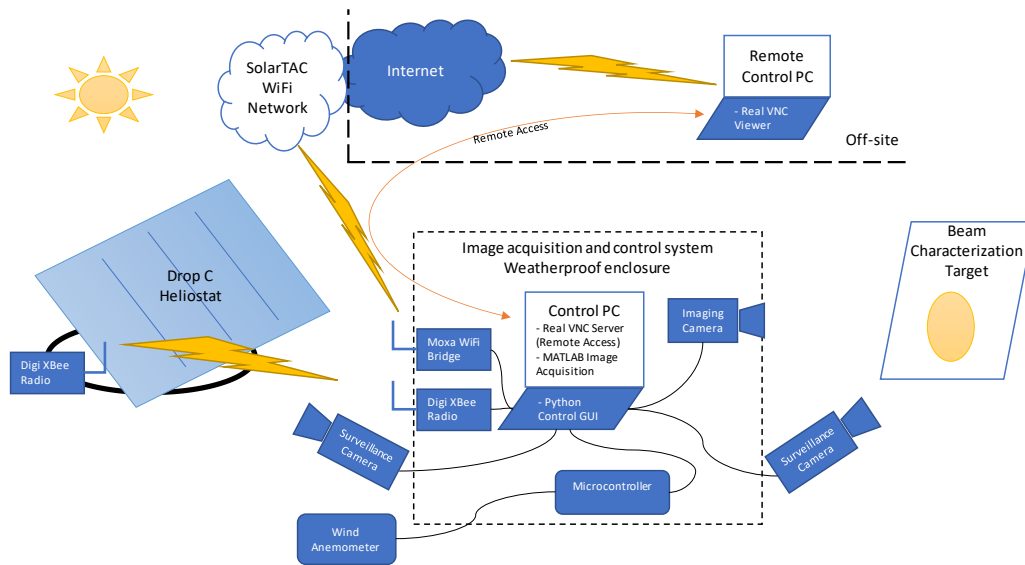


Figure 39 Remote control communication schematic

### Tracking Algorithm and Misalignment Parameters

The SunRing's tracking algorithm incorporates 6 misalignment parameters (MPs) as shown in Table 49. Once installed, initial measurements are made with simple tools which provides sufficient accuracy to get the heliostat's image on the target. These parameters get progressively refined through the two-step process below.

- Image centroid position is measured throughout the day.
- Calibrate misalignment parameters with the data above using Python algorithm.

This process is repeated until tracking error is minimized.

*Table 49 Misalignment parameters within tracking algorithm*

Misalignment Parameter	Description	Initial Value [°]		Initial Measurement Method
		2 <sup>nd</sup> Prototype	3 <sup>rd</sup> Prototype	
Azimuth home	Degrees from North	122.5	-61.2	GPS phone app
Elevation home	Degrees from heliostat normal with mirror plane perpendicular to base triangle to heliostat normal when elevation actuator at home (ie. fully retracted)	91.8	91.25	Inclinometer
East-West tilt	East/west tilt of azimuth track	-0.18	0.64	Inclinometer
North-South tilt	North/south tilt of azimuth track	0.24	-0.55	
Elevation tilt	Rotation of the elevation axis due to non-square frame	0.0	0.0	Assumed to be 0
Bore sight	Rotation of the heliostat normal from its ideal orientation orthogonal to the elevation axis	0.0	0.0	

The SunRing can track the target with this set of initial misalignment parameters, and there is tracking error as expected before any calibration steps. Tracking tests in BP2 revealed the SunRing’s image would drift throughout the day, and that no single set of MPs could minimize the tracking error to within acceptable bounds. Image drift is caused by the azimuth track being out-of-round (OOR) and non-planar. These manufacturing/installation imperfections will always be present; thus, finding a robust approach to minimize their impacts on tracking accuracy is critical. Solar Dynamics has identified four overall approaches:

1. Discretized Misalignment Parameters (MPs): use unique set of the 6 x MPs based on heliostat orientation. For example, discretize the azimuth track into 10-degree bins leading to 36 sets of 6xMPs. This captures the impact of local deviations from the idealized kinematic model.
2. Positional Sensors on Heliostat: use rotary encoder to measure absolute azimuth position along with a precision 2-axis inclinometer to measure elevation angle and elevation tilt. These sensors provide the necessary information to locate the heliostat’s normal vector.
3. Characterize Azimuth Track: similar to #2, but rather than permanently installing sensors on heliostat, use temporary sensors to characterize influence of azimuth track. Results can be used in approach #1, or used to formulate a new kinematic model that more closely matches the actual heliostat movement profile.
4. Realtime Centroid Feedback: the rapid calibration system being developed under Task 9 along with similar systems being developed by other CSP companies can

be used to provide real time feedback on image centroid. This can either be used as true closed-loop control, or it can be used to create correction factors to the idealized kinematic model.

### *Tracking Accuracy Tests – Masked-Off Facets*

For both heliostat prototypes, a portion of their mirror surfaces were masked off to facilitate on-sun tracking accuracy testing. The small target used with the 2<sup>nd</sup> prototype required a small 1x1 ft square unmasked area at the center of the heliostat. The 3<sup>rd</sup> prototype had the middle two facets un-masked to reduce peak flux as a safety precaution during the remote tracking test campaign.

### *2<sup>nd</sup> Prototype Tracking Results*

Option #1 (discretized MPs) was successfully proven with the 2a (2<sup>nd</sup> prototype with final azimuth drive carriage design) SunRing prototype. The heliostat's orientation was discretized into 10° bins using both elevation and azimuth position yielding 324 bins. An MP lookup table is stored on the heliostat's local controller where the correct MP set is found based on the heliostat's orientation.

The overall approach within the heliostat controller works as follows:

1. Every ~1 sec the controller looks up which MP bin should be used based on current orientation.
2. MP values are updated based on MP bin from Step 1.
  - If MP values are all zeros in target MP bin (occurs when heliostat tracks to new orientation due to changing sun positions), then the controller tries the following:
    - Looks for neighboring MP bins that are populated with MP values
    - If no neighbors found, continues to use previously used MP values
    - If this occurs when tracking first starts and no previous MP values are available, a set of default MP values is used

Figure 40 presents the tracking error starting on Oct 7<sup>th</sup> and ending on Nov 5<sup>th</sup> of 2021. The MPs went through 3 rounds of calibration (Oct 7<sup>th</sup>, Oct 29<sup>th</sup>, Oct 30<sup>th</sup>) to realize a full days 1-sigma tracking error of 1.34 mrad (beam basis). This is 22% better than the goal tracking error.

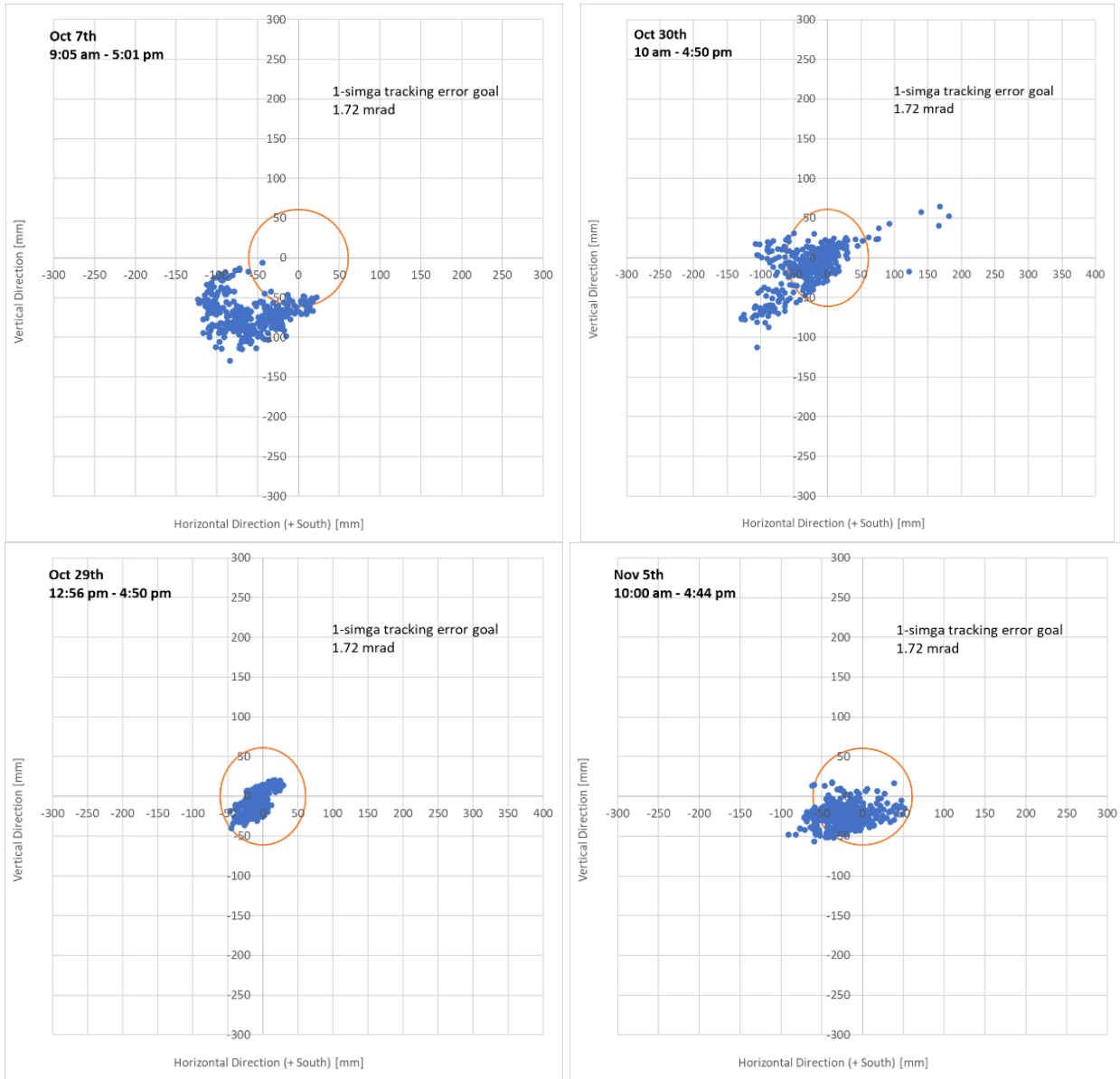


Figure 40 Tracking error minimization through calibration of 2a prototype

### 3<sup>rd</sup> Prototype Tracking Results

The discretized MP approach was used on the 3<sup>rd</sup> SunRing prototype as well. After 2 sequential days of tracking with calibration of MPs, the 3<sup>rd</sup> day of tracking resulted in tracking errors beating the accuracy goal. The measured centroid for the first three days of tracking is shown in Figure 41.

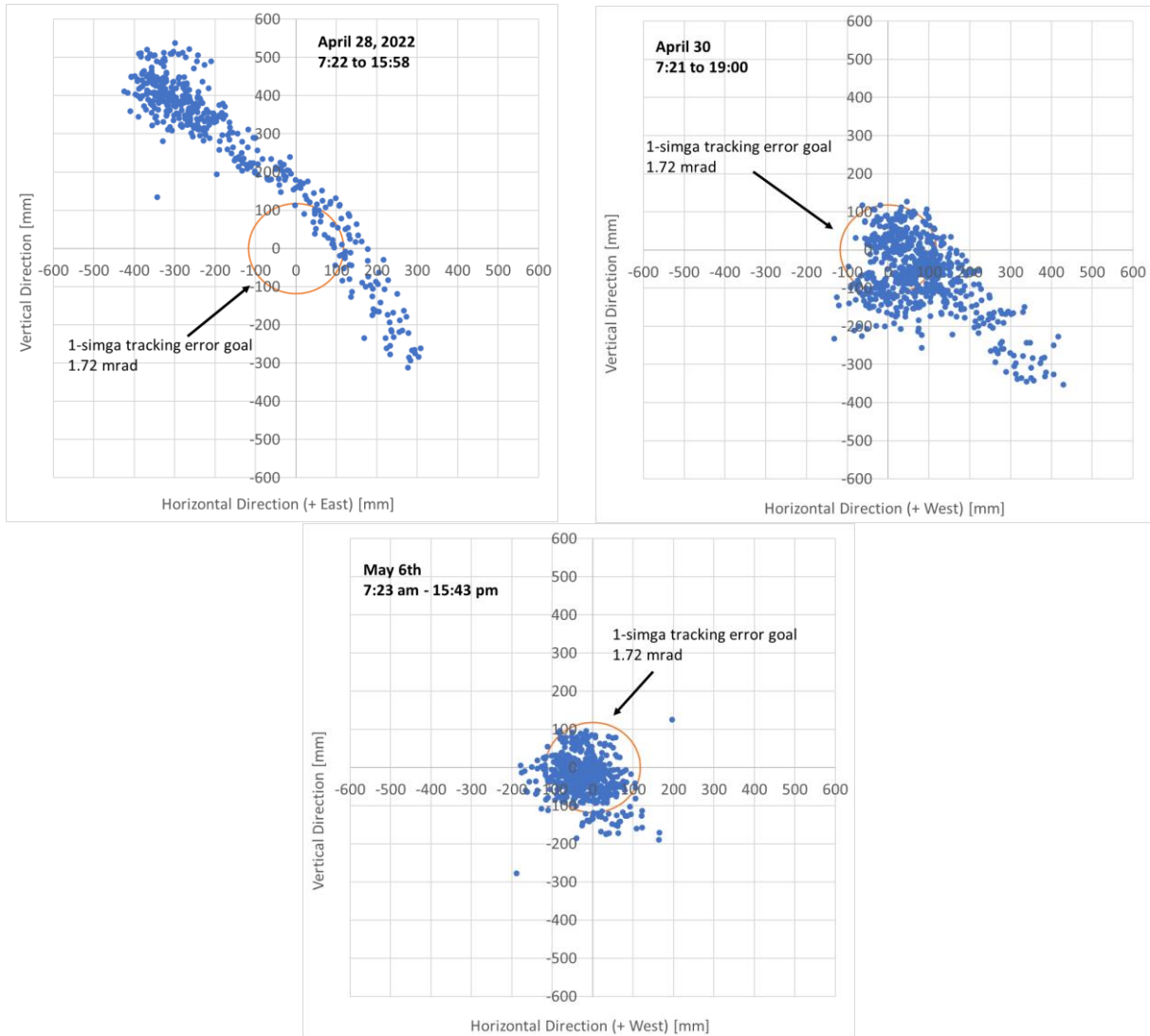


Figure 41 Tracking error minimization through calibration of 3<sup>rd</sup> prototype

Table 50 presents the progression of 1-sigma tracking beam error. After surpassing the accuracy goal on 5/6, the SunRing continued to use the same set of MPs. This yielded relatively stable tracking performance on 5/18 and 5/27. The higher tracking error on 5/27 is likely due to the presence of intermittent clouds which decrease the accuracy of the centroid measurements.



*Table 50 Measured tracking error on 3<sup>rd</sup> prototype*

Tracking Date	1-sigma tracking beam error [mrad]	MP set used during tracking
4/28/22	7.2	Initial values from Table 49
4/30/22	2.1	MP calibration set from 4/28
5/6/22	1.27	MP calibration set from 4/30
5/18/22	1.37	
5/26/22	1.41	
5/27/22	1.83 <sup>1</sup>	

<sup>1</sup> Intermittent clouds on 5/27 likely decreased accuracy of centroid measurements

The SunRing continued tracking in June; but with two issues not related to the heliostat structure itself. First, the heliostat controller’s Real Time Clock (RTC) drifted causing a mismatch between the RTC and the true time. This caused a visual offset in the SunRing’s beam centroid on the target. Second, the centroiding camera’s aperture and focus were perturbed, and this ultimately caused the Matlab image processing algorithm to hang up which prevented centroid logging. The SunRing continued tracking the target despite these issues, and visually the image appeared to remain stable albeit shifted due to the RTC offset. In total, 141 hrs of tracking have been logged to date.

### *3rd Prototype Beam Quality Setup*

The goal of beam quality testing was to quantify the SunRing’s optical performance as a function of wind loads. Duplicating the wind load profiles from the wind tunnel testing which were used in the FEA model is nearly impossible; thus, the goal of this testing is to see if the relative change in image size and its corresponding change in slope error is similar to that predicted by the FEA model.

A Matlab algorithm was developed to accomplish this using the same machine vision camera used to calculate the image centroid; the algorithm finds the physical area containing a set % of the total image power. First, the total image power is calculated by summing the pixel intensities inside the area calibrated region of interest (ROI). The area of the ROI is also divided by the number of pixels within the ROI to find the area/pixel value. The image pixel intensity array is ordered from highest value to lowest and a running power sum is calculated from highest pixel intensity to lowest until the sum equals or just exceeds the percentage total power value. The number of pixels summed to arrive at this percentage is multiplied by the area/pixel value to find the image area.

Images were captured at a rate of 10 frames/sec and post-processed with the above algorithm to determine the image area for each frame at 68% of the total power. This value was chosen assuming normal distribution statistics. This time-stamped data is overlaid with the wind speed/direction data from the anemometer located next to the image quality cabinet.

### 3rd Prototype Beam Quality Results

Figure 42 presents the results from a moderately windy day (4/1/22 with 11.3 mph average) and a very windy day (4/6/22 with 23.5 mph average). An approximate average value of 8300 in<sup>2</sup> at 68% of total power was calculated for the moderately windy day. This value increased to 10,500 in<sup>2</sup> for the high wind day.

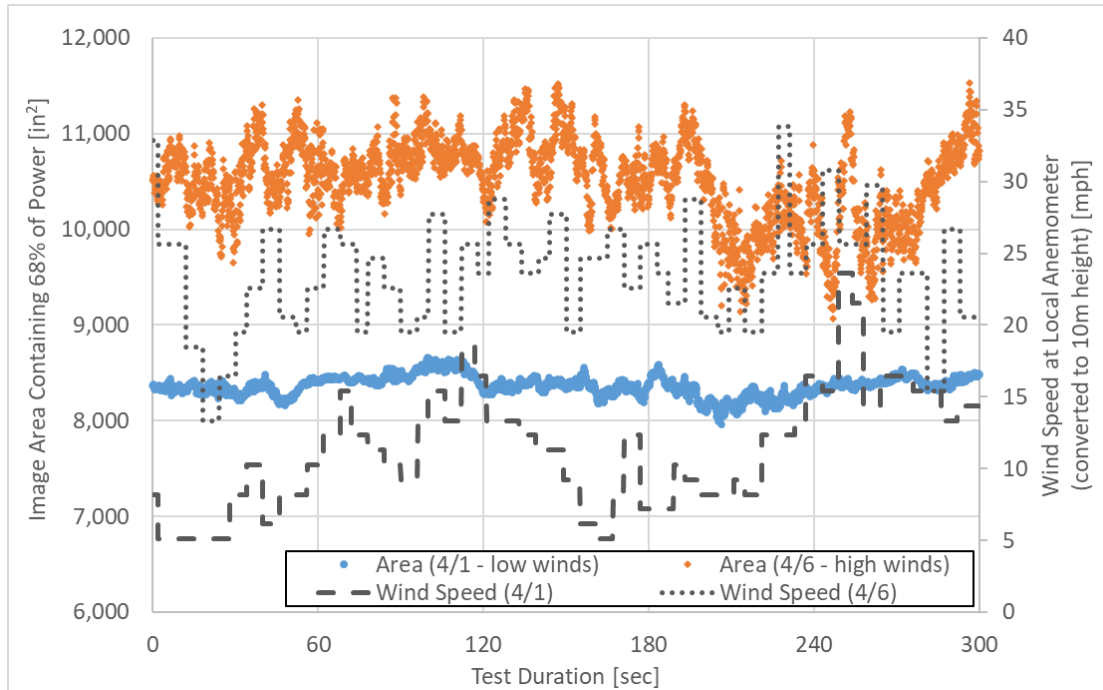


Figure 42 Image area and wind speed for 4/1 and 4/6 recordings

A model of the 3<sup>rd</sup> prototype heliostat was developed using the SolTrace optical modeling code. The model was run for the location, days and times the beam quality data were acquired. The same algorithm used in the image analysis above was applied to the flux map generated by the SolTrace model. The SolTrace slope error input value was adjusted until the area within the ROI at 68% of total power equaled that of the actual image processing results for both the moderately windy day and the high wind day. While the slope error in SolTrace is characterized by a normal distribution, the actual wind effects on the heliostat shape are not normally distributed. However, this represents a reasonable figure of merit for the relative difference between the two days.

For the moderately windy day, a slope error of 4.0 mrad R.M.S. yielded 8300 in<sup>2</sup> of area at 68% of total power metric. For the high wind day, a slope error of 5.5 mrad R.M.S. resulted in 10,500 in<sup>2</sup> of area. Thus, the increase in wind speed from 11.3 mph to 23.5 mph increased the optical error by approximately 1.5 mrad R.M.S. slope basis. This increase is high compared to the FEA prediction (at 60° elevation) of 0.3 mrad increase between calm (11.2 mph) and windy (26.8 mph) conditions. The high wind induced slope error may be caused by the same source that is creating high local slope error in facets. Lastly, the wind conditions during the experiment do not perfectly match

those in the wind tunnel from which FEA loading is derived thus making comparisons challenging.

## **2 Solar Field Communication and Control (Tasks 2,5, and 8)**

The relatively small size of the SunRing necessitates a wireless control system as the cost of a fully wired control system on a \$/m<sup>2</sup> basis would be prohibitive. A commercial Wireless Mesh Network (WMN) technology was selected and tested in a limited 30-node test in BP1. Testing was scaled to a 498 node WMN test in BP2, and the design for the complete solar field communication network was completed. Refinements to the commercial hardware selections were made in BP3. In addition to the WMN, the heliostat's local controller was conceptualized in BP1 and further detailed in BP2 resulting in two functional prototype controllers. Progress made toward SF communication and control milestones and go/no-go metrics is presented in Table 51.

*Table 51 Solar Field Communication Milestones and Final Deliverable*

Title	Metric	Success Value	Measured Value	Support Data
<b>M (ST-2.1)</b> Validation of selected WMN platform	Wireless control cost: Wireless tracking controller + Solar field control backbone	Success ≤\$100 / Reach ≤\$70 per heliostat Constraint: Affirmed by vendor to meet technical specification requirements	\$143/heliostat includes complete solar field communication network	Pages 80 & 94
<b>M (ST-5.2)</b> Expert validation of WMN integrity and security	Security fail-safes	Certified by 3rd party expert engineer	FMEA reviewed by Vanteon.	Page 88
<b>FD-4</b> Detailed design of WMN and SFCB including local heliostat controller.	Command / response	≤10 seconds, to 90% of heliostats ≤30 seconds, to 100% of heliostats	<ul style="list-style-type: none"> <li>• Passed 1/6 tests</li> <li>• 99.8% response ≤48s in 4/6 tests.</li> <li>• &lt;1.3% un-responsive in 2/6 tests</li> </ul>	Page 86
	Controller cost	Success threshold: ≤\$100 / heliostat Reach objective: ≤\$70 / heliostat	\$143/heliostat includes complete solar field communication network	Pages 80 & 94
	Update parameters / firmware	Firmware and parameters can be updated by wireless transmission	Passed in 30-node testing.	Page 81
	Security fail-safes	Predicted response to M5.2 FMEA conditions achieved experimentally	Did not perform, testing no longer needed after moving to wired SFCB.	NA

## 2.1 Overall Architecture Introduction

The overall communication network is broken down into three levels:

- Level 1 (LI): overall solar field controller housed in central control room
- Level 2 (LII): multiple units distributed throughout the solar field, relays communication between single LI controller and hundreds of LIII controllers
- Level 3 (LIII): heliostat's local controller

The communication network between the LI and LII controllers is referred to as the Solar Field Communication Backbone (SFCB) in the following. Figure 43 provides the final solar field network topology which will be detailed in the following sections.

### 2.1.1 Specifications

Table 52 summarizes the key functional and non-functional requirements that have been defined for the SunRing's controller and wireless communication system.

*Table 52 Wireless controller key requirements*

Parameter	Unit	Value
Lifetime	[years]	30
Controller Mean Time To Failure	[hours]	200,000
LIII Controller field replacement	[minutes]	10
LIII Controller enclosure	[-]	IP65 / UV resistant / Passive cooling
Wireless roundtrip broadcast command latency	[seconds]	10 ( $\geq$ 90% of heliostats) 30 (all heliostats)
Wireless roundtrip unicast command latency	[seconds]	10
Wireless heliostat status update rate	[seconds]	30
Wireless heliostat over-the-air-programming update	[hours]	1 (per heliostat) / 72 (all heliostats)
Wireless security	[-]	Access Control List / End-to-end encryption / Frequency hopping / Interference tolerant

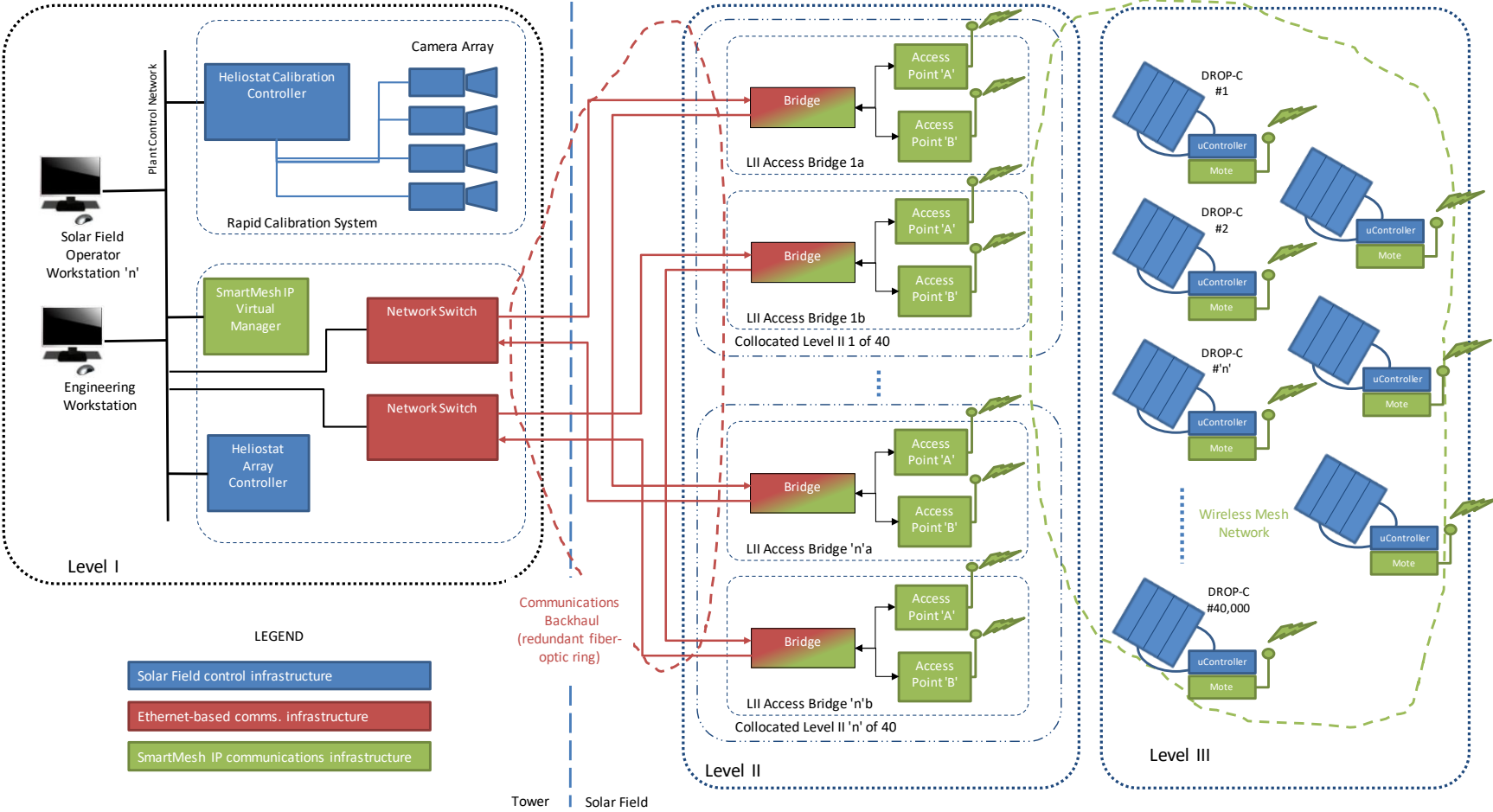


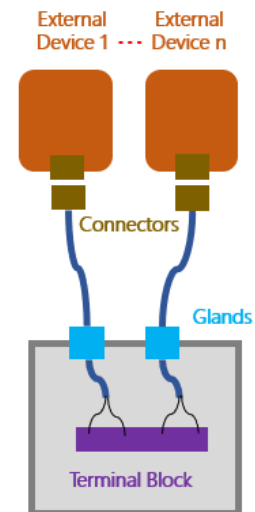
Figure 43 Solar field communication architecture

## 2.2 Heliostat Local Controller

While larger heliostats can utilize off-the-shelf PLCs, the relatively small SunRing necessitates use of a custom integrated circuit for its local controller to be cost competitive. After Solar Dynamics created a conceptual local controller in BP1, electronics design firm Zebulon was hired in BP2 to refine the controller design. Zebulon’s preliminary design resulted in a Bill of Materials and cost model along with two functional prototypes with one used to run the SunRing prototype. The main hardware used in the local controller is detailed in Table 53.

Table 53 Core controller hardware selection.

Hardware	Make/Model	Functionality
Microcontroller	ST STM32 F401RE	<ul style="list-style-type: none"> <li>• Solar vector calculations</li> <li>• Heliostat positioning calcs.</li> <li>• Dual servo motor control</li> <li>• Operation mode state machine</li> <li>• Alarms and event logging</li> <li>• Battery balancing logic</li> </ul>
Wireless Radio	Analog Devices SmartMesh IP	<ul style="list-style-type: none"> <li>• WMN interface to SFCB</li> </ul>
2 x BLDC Motor Driver	Texas Instruments DRV8304H	<ul style="list-style-type: none"> <li>• Bi-directional and variable-speed 3-phase brushless DC motor driver with 3x hall sensor inputs</li> </ul>
Battery Charge Controller	Analog Devices LT8491	<ul style="list-style-type: none"> <li>• Battery charge control</li> <li>• Photovoltaic panel Maximum Power Point Tracking (MPPT)</li> <li>• I2C telemetry to host controller</li> </ul>
Battery Management	Intersil ISL94208	<ul style="list-style-type: none"> <li>• Passive battery cell balancing hardware</li> </ul>



*\*connector on actuator side  
 either at actuator or on pigtail*

*Figure 44 Controller external connections type*

The controller’s cost as a function of volume and country of origin is shown in Table 54. The Drop-C project reference is 200k production in China. The cost model assumes the connection type shown in Figure 44 where a DEUTSCH quick connector is used, the controller BOM includes the DEUTSCH connectors on the controller side only.

*Table 54 Controller cost estimate*

Production Volume	Country of Fabrication		
	USA	Mexico	China
40k	\$162.95	\$155.64	\$149.38
200k	\$113.58	\$106.69	\$101.77

## 2.3 Wireless

### Mesh Network (L2-L3 communication)

#### 2.3.1 Technology Down Selection

A Wireless Feasibility Analysis was conducted to assess the landscape of commercial-off-the-shelf (COTS) wireless technologies. Extensive studying of wireless security challenges, best practices, and limitations aims to ensure the selected wireless technology will operate securely given the ever-present threat of wireless transgression. Finally, commercial outreach to wireless technology experts and integrators helped to provide adequate understanding of the science behind the technology as well as to ensure no technology was overlooked during the analysis. In total, 8 contacts were made with commercial wireless companies and 18 wireless technologies analyzed for feasibility. Table 55 lists the technologies analyzed and companies contacted.

*Table 55 Wireless technologies and commercial companies contacted.*

COTS Wireless Technologies Reviewed		Companies Contacted
ISA100.11a	SmartMesh IP	DUST Networks
WirelessHART	ZigBee PRO	Vanteon
ANT+	Bluetooth LE	Digi International
DASH7	DigiMesh	Twin Eagles Consulting
Sigfox	THREAD	Ingenu
WiSUN	Zumlink	Laird
Z-wave	802.11 (WiFi)	Freewave
802.15.4	HaLow	Control Data Systems
WIA-PI	LoRA	

Driven by requirements of low power operation and low cost, radio technology categorized built upon the IEEE 802.15.4 standard and marketed as “Internet of Things”



(IoT) lends relevance to this application. Of the 18 technologies studied, only four technologies – namely ISA100.11a, SmartMesh IP, WirelessHART, and ZigBee PRO – were deemed suitable for industrial applications and proceeded with a detailed comparison study with emphasis placed on industrialization, redundancy, security, over-the-air-programming, and scalability factors. The mesh network technology SmartMesh IP emerged as the best wireless solution for this application primarily based on scalability to 10s of thousands of nodes, suitability for operating in a dense network, ease of testing, system-wide redundancy features, plethora of developer resources, and support service.

Solar Dynamics contracted with the wireless development company Vanteon as an objective 3<sup>rd</sup> party to review the proposed wireless mesh network. Vanteon proposed using a star network based wireless topology as the tall central solar tower could provide unobstructed line-of-site to every heliostat in the solar field. However, a custom protocol would be required to support the 40 to 100 thousand wireless nodes.

Vanteon performed a Wireless Technology Comparison study to determine if a custom star network held enough advantages to warrant the large development costs associated with a custom protocol. The results of this study once again narrowly concluded that the SmartMesh IP technology is the best candidate for a wireless heliostat; not because of best performance, but mainly driven by ability to rapidly test, lower development costs, and proven industrial track record.

### **2.3.2 SmartMesh IP Introduction**

Developed by Dust Networks, and subsequently acquired and marketed by Analog Devices, SmartMesh IP is an industrial grade wireless mesh networking technology that consists of hundreds or thousands of wireless nodes, known as motes, along with a network manager and multiple access points. The mote's self-form a mesh network allowing for communication redundancy, adaptability to changing Radio Frequency (RF) environments, and high reliability due to multiple paths a communication packet can be routed, ensuring successful packet delivery. Additionally, the SmartMesh IP technology utilizes frequency hopping per transmission, adding another layer of robustness in congested RF spaces. Finally, all motes are time synchronized and each is given a small slice of time to perform communication transmissions. This feature eliminates the chances of a communication transmission being stepped on and lost by another mote transmission.

A drawback of wireless mesh technology is that it inherently increases communication traffic to form and maintain the mesh network routing tables, leading to increased application communication latency. However, a heliostat solar field wireless communication application does not necessarily require sub-second latency, so this drawback is of limited concern. Testing throughout this project verified that the technology met the network latency requirements.

### **2.3.3 30-Node Test**

In BP1, wireless network testing took place November 7-9, 2018 at Sandia Laboratories National Solar Thermal Test Facility (NSTTF) in Albuquerque, New Mexico. A 30-node

(also called motes) SmartMesh IP network was created within the NSTTF's heliostat field. Figure 45 shows where the nodes were placed on the heliostats and on which heliostats within the solar field. The network's performance was tracked throughout a solar tracking day to understand if changes in heliostat orientation impacted network performance. Table 56 summarizes the performed tests and results.

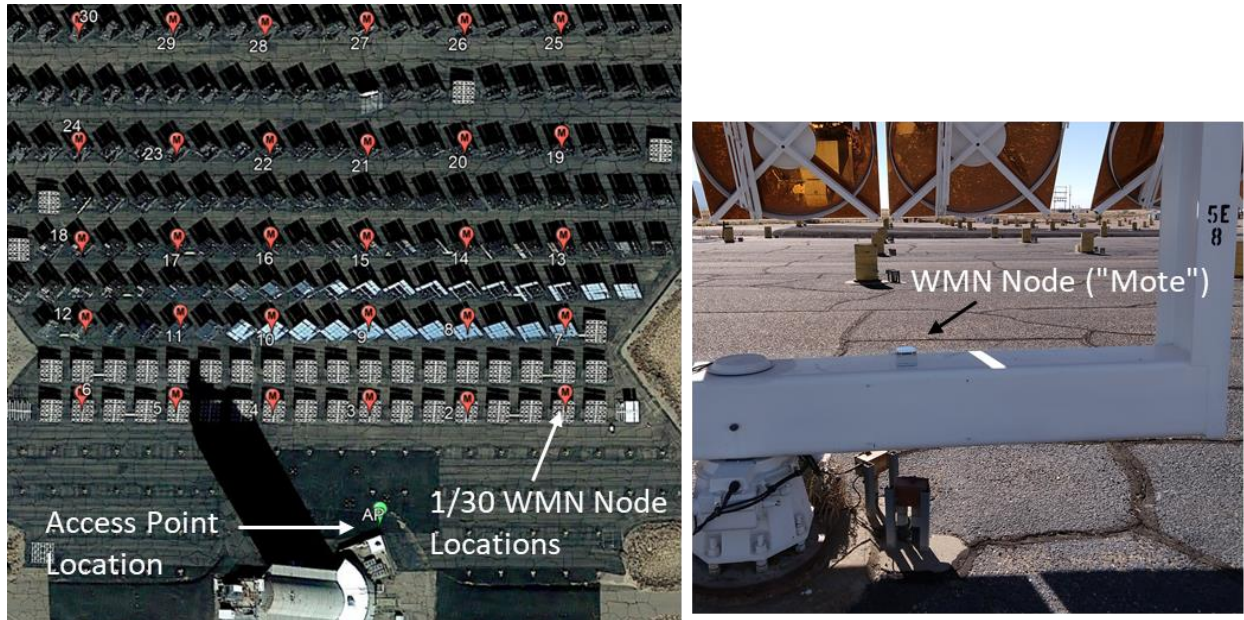


Figure 45 Aerial view of NSTTF field with node locations (left), location of nodes on heliostat (right)

*Table 56 30-node SmartMesh IP testing summary*

Use-case Test	Description	GNG-2 Success Value	Results
Command / Response (repeated 4 times)	Broadcast command to all motes to toggle onboard LED. Measure round-trip time for each mote to acknowledge command.	<ul style="list-style-type: none"> <li>• 90% of motes (27) acknowledge ≤ 10 seconds.</li> <li>• 100% of motes acknowledge ≤ 30 seconds.</li> </ul>	Worse case <ul style="list-style-type: none"> <li>• 27 motes acknowledge ≤ 10 seconds.</li> <li>• All motes acknowledge ≤ 13.2 seconds</li> </ul>
Update Parameter (repeated multiple times)	Send a unicast command to single mote to get/set a parameter. Measure the round-trip time to acquire the parameter.	<ul style="list-style-type: none"> <li>• Parameter update / received within 30 seconds.</li> </ul>	Worse case – mote with worse latency <ul style="list-style-type: none"> <li>• Get = 2.5 seconds</li> <li>• Set = 4 seconds</li> </ul>
Update Firmware	Send a new firmware image to the mote microcontroller over the wireless mesh network. After reset, mote will operate on new firmware.	<ul style="list-style-type: none"> <li>• Over the Air Programming (OtAP) process successfully completes - no time duration set</li> </ul>	2-hop deep mote. 146 Kbyte image file size <ul style="list-style-type: none"> <li>• OtAP duration = 1.83 hour</li> </ul>

*Maximum Range of Single Hops*

Additional quantitative information was collected during the testing. Every SmatMesh IP mote generates a Health Report (HR) every 15 minutes which includes RSSI<sup>1</sup> and PSR<sup>2</sup> values from/to neighboring motes. HRs are sent to the network manager and used to build and optimize the mesh network. Collecting these HR over time helps to understand the wireless operation in a changing RF space with the moving heliostats. Figure 46 presents a scatter plot of PSR vs Distance showing a significant ‘knee’ at around the 300-foot distance where PSR falls to < 50%, indicating unreliable communications beyond. The Solar Field Level II layout is based on a single hop range of 300 ft.

---

<sup>1</sup> RSSI - Radio Signal Strength Indicator. Measure of the received RF energy from the transmission of another mote.

<sup>2</sup> PSR – Packet Success Ratio. The ratio of successfully transmitted packets versus the number of packets sent. PSR > 50% if generally considered adequate for reliable communications.

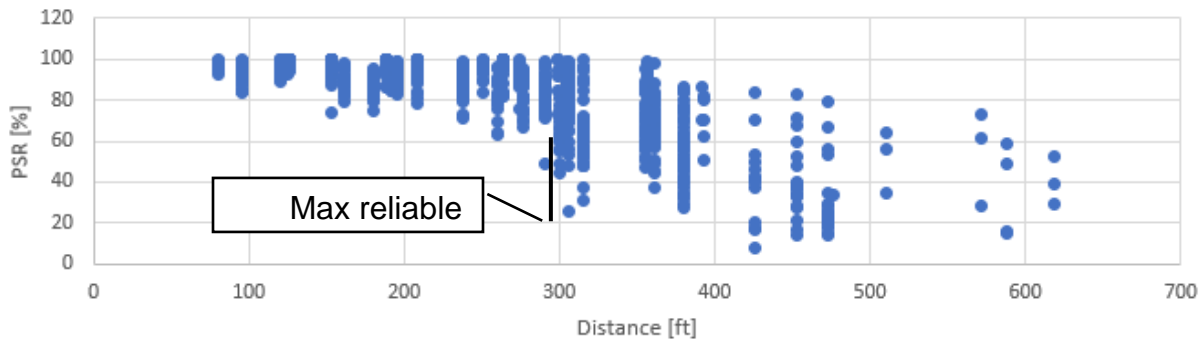
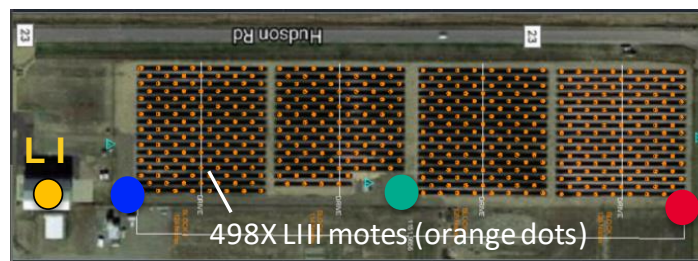
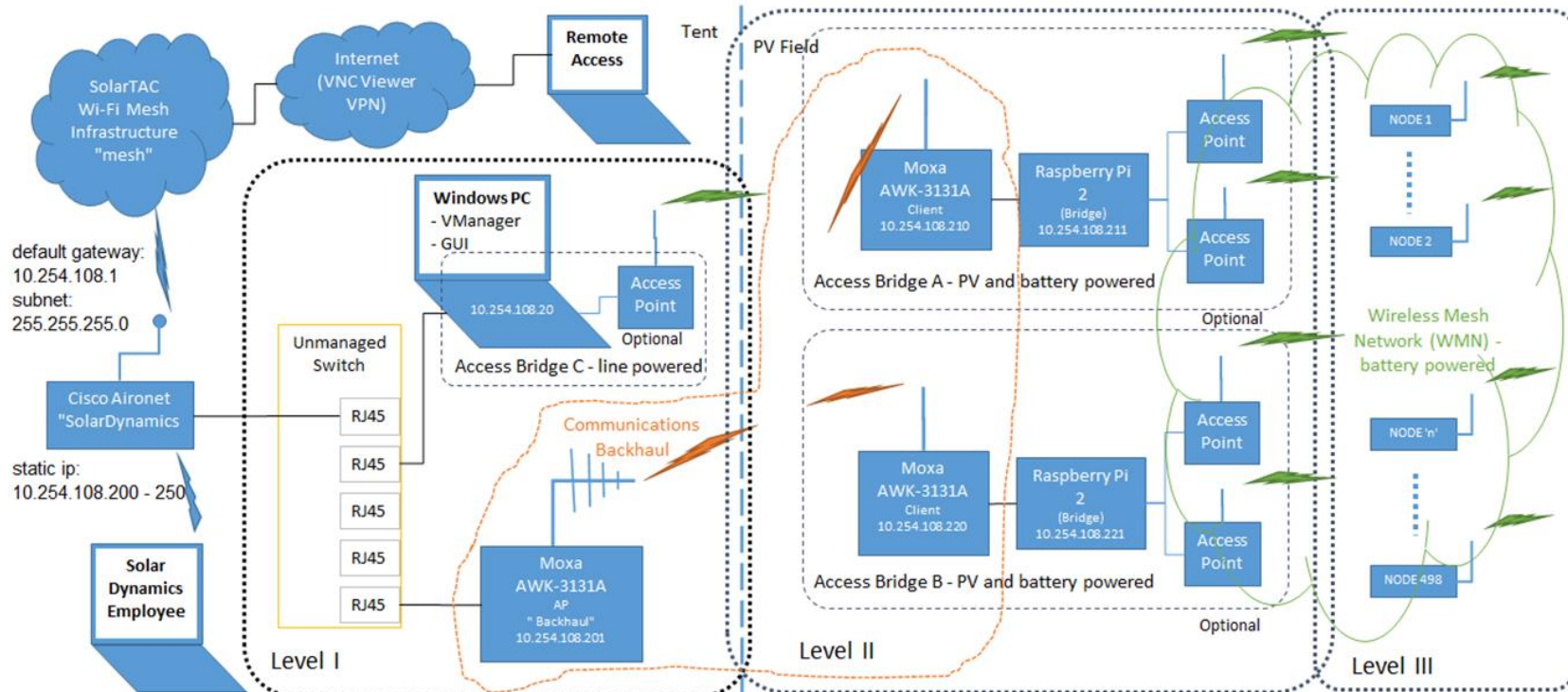


Figure 46. Packet Success Rate vs. distance between motes captured during heliostat tracking from 10am to 4pm.

### 2.3.4 498 Node Test

In BP2, a 2 MW Photovoltaic array at the SolarTAC facility was used to test a 498-node SmartMesh IP wireless network. Figure 47 shows the communication system architecture and mote layout map. A wireless SFCB communicates between the LII controllers and the central LI controller. A Python-based Graphical User Interface (GUI) was developed for the wireless network. This GUI serves as the starting point for the commercial SunRing solar field GUI that will be used within the plant's control room.



**LII Location Key**

**Placement Test Setup**

- Setup A: 1 x LII
- ● Setup B: 2 x LII
- ● Setup B0: 2 x LII
- Setup C: 1 x LII

Figure 47 Wireless communication system architecture and mote layout map

### 2.3.5 Command Response Test

Command-response testing began with Level II Setup ‘C’, followed by Setup ‘A’, and then ‘B’. Unfortunately, the battery in approximately half the motes drained between testing different setups, resulting in only 207 operating motes for testing of Setup ‘B’. Fortunately, data resulting from wireless Level II Setup ‘B\_0’ (combination of Setup ‘A’ and ‘C’ used during commissioning) provides a more extreme test setup than Setup ‘B’. Table 57 summarizes the test results with the different LII configuration setups and two different PV field tilts.

*Table 57 WMN Command/Response test results*

Trial # / PV Tilt	Test Metrics		Setup ‘A’	Setup ‘B’	Setup ‘B_0’	Setup ‘C’
			1 LII: centered in PV field. Represents a normal operating heliostat field.	2 LII: 1 at North end & 1 at South end of PV field. Represents a normal operating heliostat field.	2 LII: 1 centered & 1 South end of PV field. <i>Used for test system commissioning.</i>	1 LII: South end of PV field. Represents the loss of an adjacent Level II.
Trial 1 /0° tilt	# nodes in network		464	207	NA, did not test.	462
	# of node responses received	t ≤ 10s	347 (74.8%)	207 (100%)		397 (85.9%)
		t ≤ 30s	464 (100%)	207 (100%)		455 (98.5%)
	Additional responses at t > 30s		NA	NA		1 (0.2%) by 39s
	# nodes with no response		0 (0.0%)	0 (0.0%)		6 (1.3%)
Trial 2 /60° tilt	# nodes in network		477	207	477	Did not test. <sup>6</sup>
	# of node responses received	t ≤ 10s	425 (89.1%)	192 (92.8%)	456 (95.6%)	
		t ≤ 30s	473 (99.2%)	205 (99%)	473 (99.2%)	
	Additional responses at t > 30s		4 (0.8%) by 42s	0	4 (0.8%) by 48s	
	# nodes with no response		1 (0.2%)	2 (1.0%)	NA	

#### *Main conclusions*

1. Compared to GNG-5 criteria (90% of heliostats respond ≤ 10s, 100% respond ≤ 30s)
  - a. Setup B/Trial 1: Passed
  - b. Remaining tests: Failed, *however*:
    - i. The worst response had 98.5% of nodes responding by 30s and 4/6 tests had 99.8% of nodes reporting by 48s.
    - ii. Typical molten salt inlet vessel on receiver sized for 60s of flow, thus above results do not require modification.

---

<sup>6</sup> Data discounted as it was later discovered that a previous ‘Path Stability’ test caused over half the wireless motes to become lost and not connected to the network.

2. A node’s non-response at the LI controller does not mean the message was not received by the LIII node. The likelihood of successful transmission is much higher for the LI to LIII broadcast than the LIII to LI unicast message reply from each node.
3. A node with no response is the result of the testing protocol. A more robust set-up of the LI broadcast and LIII unicast protocol needs to be developed to address these situations.
4. Performing under Setup B with the full set of motes would likely see similar results as the 207-mote test. The primary metric effecting latency is Network Path Stability<sup>7</sup> and initial Path Stability testing shows near 100% stability in all configurations.

*Additional Conclusions*

Table 58 shows the average mote latency for a given number of hops in the mesh network. The latency generally increases in a linear fashion for an increasing number of hops except for the first hop, as there is a set minimum overhead for network communications. This data is the basis for plant solar field wireless network planning. Compared to a network planning tool provided by the vendor, this data is within 30% of the tool estimated values, validating the accuracy of the tool.

*Table 58 WMN communication latency results*

Number of Hops	Communications Latency [msec]	
	Data	Network Planning Tool
1	637	480
2	982	1340
3	1754	2200
4	2526	3060
5	3015	3920

**2.3.6 Update Parameter/Firmware Update Test**

These tests were not performed with the 498-node network; these tests were scheduled as the final testing, and by this time most motes batteries were drained. However, there is little doubt that these tests will pass as both were shown to work in 30-node testing.

The remaining question is how long it takes to update the firmware of the entire solar field. With the current controller firmware size of 147.82 Kbytes, a single heliostat is calculated to take at most 5.4 hours to update. A total of 338 heliostats can be updated simultaneously from each LII-pair (discussed in Section 2.5), and with 41 LII-pairs, a total of 13,858 heliostats can be updated simultaneously. The baseline 30,000 heliostat solar field will take at most 11.7 hours for a firmware update which is acceptable for this rare firmware update event.

---

<sup>7</sup> Path Stability is primarily based on simultaneous transmissions colliding. Since SmartMesh IP is a Time-synchronized protocol with only one network in operation, the chances of this are mostly negligible.

### **2.3.7 Level II Fail Test**

Hundreds of motes were lost during the simulated failure of one Level II Access Bridge, and it took 40-100 minutes for the network to rebuild, which is unacceptable for a solar field network. The cause was explained upon review with Analog Devices' application engineer. Each mote has two parent motes in the mesh that are used to 'hop' transmissions between it and the LII Access Bridge. A failure at the LII leads to loss of all subsequent motes connected to it through its two parents. Refer to Section 2.5 for the updated LII commercial design that mitigates this risk.

### **2.3.8 Network Coexistence**

One of the main requirements of the wireless communication system is that it operates in the 2.4GHz ISM band which has no licensing or permitting requirements worldwide. The SmartMesh IP mesh network operates at 2.4 GHz, and there will be additional 2.4 GHz traffic from the SFCB if wireless is chosen over fiber-optic, cell phones, and other wireless communication systems used in the plant. One key trait of SmartMesh IP is that it has dynamic frequency hopping for every wireless transmission.

A Vector Signal Analyzer (VSA) was used to measure the radio transmission in the 2.4GHz frequency space. This method provides a qualitative measure of how the SmartMesh IP mesh network accommodates other wireless systems. The VSA identified three other 2.4 GHz wireless networks co-existing with the SmartMesh IP network, and it showed the SmartMesh IP was able to find available spectrum (time and frequency) to transmit data. Based on these results and those from command/response testing, it is concluded that the SmartMesh IP wireless mesh technology can adequately operate within a congested 2.4GHz frequency space.

## **2.4 FMEA of Solar Field Communication Network**

A Failure Modes Effects Analysis (FMEA) was performed on the solar field communication network with review from Vanteon Corporation. Below are the key risks.

### **2.4.1 Wireless signal jamming**

The FMEA found that jamming of the SFCB presents the highest security risk. The SFCB funnels communication to all heliostats through the 80 LII controllers back to the central LI controller. Jamming the backhaul at a single LII controller would disrupt communication to potentially 1,600 heliostats, and jamming the backhaul at one of the L1 antenna arrays on the tower would disrupt communication to approximately 25% of the solar field. The worst-case scenario is that these heliostats go to their fail safe stow position which rapidly changes the flux profile on the receiver.

Vanteon was tasked with identifying countermeasures to jamming of the SFCB. The most effective technique with moderate development costs was a custom Direct Sequence Spread Spectrum (DSSS) protocol integrated into the backhaul signal. With DSSS, the original data signal is multiplied with a pseudo random noise spreading code, and by using a custom DSSS protocol the random noise code would be proprietary.

It was realized later in BP2, that a backhaul with a custom DSSS protocol can still be jammed with a jamming signal of significant strength. The goal was then to define a 'typical' jamming signal's source power level and distance from the SFCB radios. A



‘typical’ malicious jamming signal was constrained by the size of equipment that could be contained in a standard sized van and parked at the edge of the solar field.

At a distance of 1,150m (max radius of baseline solar field) and with a 10-100W power source (100W power amplifier is ~40lb and 1x1ft), a jamming signal directed at a LII controller in the field or antenna array on the tower would prevent communication even with DSSS implemented.

The baseline SFCB will use a wired connection due to the malicious jamming threat. However, if a project site has low security risks or for smaller demonstration sites, a COTS wireless backhaul with DSSS can be deployed (similar to system used in 498-node testing).

### 2.4.2 Wireless signal spoofing

Second in severity to jamming, spoofing or the ability to inject false communications into the wireless communication system is another security risk. The biggest offense to thwart spoofing is deploying a custom wireless protocol (security through obscurity). The SmartMesh IP heliostat network is proprietary to Analog Devices which is essence a custom protocol to attackers. With a wired SFCB, there is no additional spoofing countermeasures needed.

## 2.5 Detailed Solar Field Communication Design

The following summarizes the commercial design of the solar field communication network. The wireless mesh network design assumptions remain unchanged from BP1 and are summarized in Table 59.

*Table 59 – Solar Field wireless mesh network design assumptions.*

Design Assumption	Value	Units
Number of heliostats:	30,000	-
Max reliable mesh radio communication range:	300 [90] <sup>8</sup>	ft [m]
Max number of mesh radiocommunication hops:	3	-
Emergency stow communication bandwidth:	2,700	Packets <sup>9</sup> / sec
Heliostat status update communication bandwidth:	1,000	Packets /sec

<sup>8</sup> Based on reliable range measured in Sandia heliostat field in BP1

<sup>9</sup> 1 Packet = 90 Bytes of data.

Section 2.3.7 described the network interruption due to the loss of a LII which prompted the following design change. Two LII's will be collocated as pairs in the solar field, but they will be physically separated by ~10 feet and be totally independent in operation. This arrangement promotes motes having a parent link to two distinct LII Access Bridges; thus, if one LII Access Bridge fails, the mote will remain in the network. This new Level II Access Bridge pair arrangement is now referred to as Level II Access Bridge Pair, or LII-pair for short. Figure 43 presented earlier shows the revised Solar Field communication network high-level architecture with collocated LII-pairs.

LII-pairs are distributed throughout the solar field, and their placement is governed by two criteria: 1.) limit # of hops to  $\leq 3$  and 2.) ensure LII-pair design can handle bandwidth requirement for all heliostats served. First, the 3-hop constraint is used to place the LII-pairs as shown in Figure 48. Each white dot represents a single heliostat, and the concentric circles define the number of hops from a central LII-pair. The green circle is 1-hop, yellow is 2-hop, and red is 3-hops from LII-pair. The 3-hop deep space around a LII-pair is call a 'cell' in the following. All heliostats are within a 3-hop communication distance from a LII-pair except for a small percentage at the field's outer periphery.

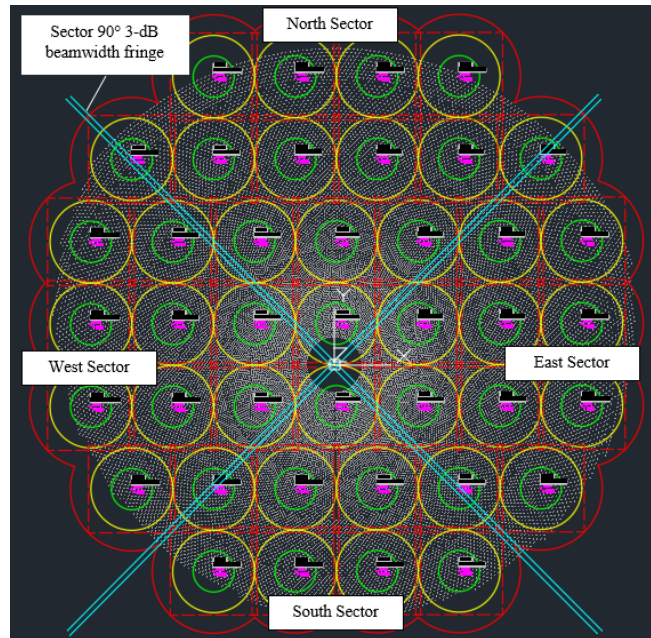


Figure 48 Level II placement in solar field with mesh network hop rings

With LII-pairs placed, the LII-pair is designed to have sufficient bandwidth to support an emergency stow event where the requirement is a command/response latency of  $\leq 10$  seconds for 90% of heliostats and  $\leq 30$  seconds for all heliostats. The SmartMesh IP Access Point (AP) motes located at the LIIs transmit all communication between LI and LIII controllers, and they have a 40 packet / sec limit. There are 2 AP motes per LII and 2 LII per LII-pair, so a maximum bandwidth of 160 packets / sec for the LII-pair. Each heliostat sends one packet to Level I during an emergency stow event. Therefore, a theoretical maximum of 1,760 heliostats can be accommodated by the LII-pair. No LII-pair exceeds this threshold; thus, the proposed LII-pair layout meets all requirements.

Final wireless communications network specifications are presented in Table 60.

*Table 60 – Solar Field wireless mesh network specifications.*

Specification	Value	Units
Number of LII per solar field <sup>10</sup> :	82	-
Wireless mesh Access Point motes per LII:	2	-
Max LII communications bandwidth:	80	Packets / sec
Total solar field LII communications bandwidth:	6,560	Packets / sec
Estimated mote command/response latency <sup>11</sup> :	<10	seconds

### 2.5.1 Solar Field Communication Backbone

A redundant fiber-optic ring network is the baseline SFCB mainly due to the cyber security risks uncovered during the FMEA study outlined above. Table 61 summarizes the trade-offs between the wired and wireless backhaul network.

*Table 61 Wired vs wireless backhaul tradeoffs of 30k heliostat field*

	Wired Backhaul	Wireless Backhaul
<b>Description:</b>	<ul style="list-style-type: none"> <li>- 3x redundant fiber optic ring networks</li> <li>- Direct buried fiber optic cable</li> </ul>	<ul style="list-style-type: none"> <li>- Wireless COTS radios with OFDM protocol at 5.0 GHz</li> <li>- Directional antennas</li> </ul>
<b>Pros:</b>	<ul style="list-style-type: none"> <li>- Lowest risk</li> <li>- Immune to jamming and interference</li> <li>- High data rates allows for additional sensors/hardware in solar field</li> </ul>	<ul style="list-style-type: none"> <li>- Quicker installation</li> <li>- No trenching needed</li> </ul>
<b>Cons:</b>	<ul style="list-style-type: none"> <li>- Installation method and costs depend on site soil conditions</li> </ul>	<ul style="list-style-type: none"> <li>- Susceptible to malicious jamming</li> </ul>
<b>Costs:</b>	<ul style="list-style-type: none"> <li>• Fiber optic cable + install: \$300-\$780k</li> <li>• Hardware: \$250K</li> <li>• Total: \$0.67-1.27/m<sup>2</sup></li> </ul>	<ul style="list-style-type: none"> <li>• Hardware: \$260K</li> <li>• Total: \$0.52/m<sup>2</sup></li> </ul>

#### *Optional Wireless Backhaul*

A wireless SFCB may be preferred at select sites where the benefit of quicker installation, no ground trenching outweighs cyber security threats. A wireless SFCB can operate either in the 2.4 GHz or 5.0 GHz. Although testing with the 498-node network did not reveal any 2.4 GHz co-existence issues with SmartMesh IP, a full solar field will see higher network traffic, and this is the primary motivation to use the 5.0 GHz frequency for the SFCB.

<sup>10</sup> Arranged in collocated groups of two called a LII-pair. 40 LII-pairs in total.

<sup>11</sup> From SmartMesh “Power and Performance Estimator” network planning tool from Analog Devices. Calculated as follows: 99% US Latency = 8.89s + Mean Broadcast DS Latency = 0.13s + 1 s of backhaul network overhead.

With this change, COTS Wi-Fi radios operating at 5.0 GHz use OFDM modulation, not the DSSS modulation that was cited as the most jamming resistant from the wireless FMEA. However, there are many critical infrastructure sites using 5.0 GHz radios that are secure and reliable, so this change is assumed to be acceptable given industrial adoption and usage.

5.0 GHz wireless communication does not have the range of 2.4 GHz. Therefore, a detailed Link Budget / Fade Margin model was created to analyze each Level II Access Bridge wireless backhaul connection, considering reference radios, antennas, cable losses, lightning suppression / RF filter losses, and the wireless antenna radiation patterns and location in the solar field. Starting at the central tower, there will be four sector antennas with a 90-degree radiation pattern in the azimuthal (horizontal) plane and a 5.5-degree radiation pattern in the elevation (vertical) plane. The Level II Access Bridge will use a directional panel antenna.

Next, the optimal height of the tower and Level II backhaul antennas must also be considered when developing the Link Budget / Fade Margin model, as to ensure all Level II antennas are in the very narrow 5.5-degree elevation radiation pattern, for optimal sensitivity. The optimal height of the tower antennas is 20 meters [65.6 feet] and for the Level II antennas is 8.7 meter [28.5 feet] to provide clear line of site and to avoid heliostat RF interference. This is illustrated in Figure 49.

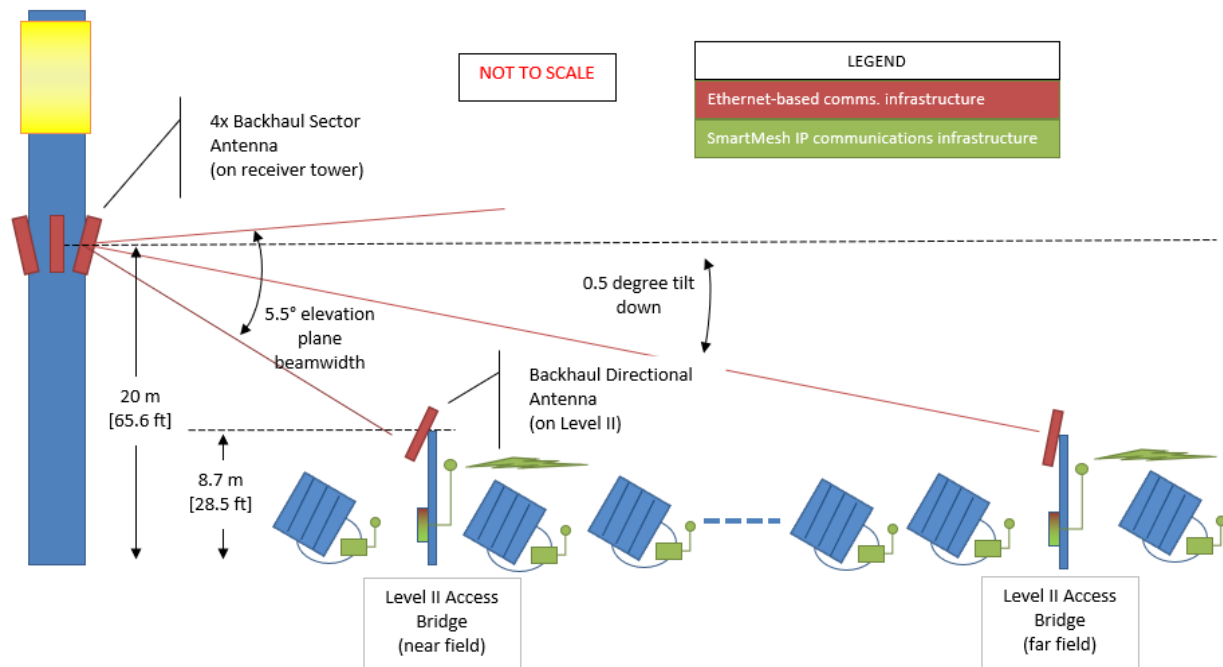


Figure 49 Installation of backhaul sector antenna on tower

With the physical hardware and layout of the wireless backhaul system detailed, the Link Budget / Fade Margin of the wireless backhaul can be calculated for each Level II Access Bridge. Table 62 summarizes the results.

*Table 62 Link budget / fade margin for optional wireless SFCB*

	<b>LII-101</b>	<b>LII-103</b>	<b>LII-205</b>	<b>LII-208</b>	<b>LII-305</b>	<b>LII-317</b>
Distance [m]	643.5	654.6	908.0	770.8	1,279.9	1,265.7
Transmitter Antenna Gain [dB]	12.0	12.0	8.0	8.0	8.0	8.0
Free Space Loss at Distance [dB]	103.41	103.56	106.4	104.97	109.38	109.28
Received Signal Power [dBm]	-59.7	-59.9	-66.7	-65.3	-69.7	-69.6
Fade Margin [dB]	28.3	28.1	21.3	22.7	18.3	18.4

Calculation Hardware Constants

- Reference radios: Moxa AWK3131A. 802.11b protocol. 11.0 Mbps Data Rate.
- Transmitter power: 25 dBm [0.32 Watt].
- Transmitter cable losses: 2.1 dB.
- Transmitter antenna: Cisco Aironet ANT5117S-N 90 deg sector. 16.5 dBm gain.
- Non-Line-of-Sight Fade Margin: 3.0 dB (for a Safety Margin).
- Receiver antenna: Moxa ANT-WSB5-PNF-16 directional. 16 dBm gain.
- Receiver cable losses: 4.2 dB.
- Receiver sensitivity: -88.0 dBm (Moxa AWK3131A)

For mission critical RF telemetry links, a wireless connection should target a minimum Fade Margin of between 20 and 30 dB. From the summary of results, there are a few Level II's with a Fade Margin less than the recommended 20 dB. These are located farthest away from the tower and on the fringes of the tower sector antenna's 90-degree horizontal radiation pattern. This does not indicate the wireless link will not work. It suggests that if other environmental factors occur that are not accounted for in the model, that the reliability may suffer. However, the calculations are made with a conservative Non-Line-Of-Site fade margin of 3 dB for a margin of safety, when in fact it should be 0 dB because of the non-obstructed line of site between tower and Level II antennas.

*Total Cost*

The complete cost for the 30,000-heliostat reference heliostat field's communication system is shown in Figure 43.

*Table 63 – Solar field wireless communication system summarized cost estimate.*

<b>SF Level</b>	<b>Description</b>	<b>Quantity / S.F.</b>	<b>Estimated Cost</b>	<b>Total S.F Cost</b>
LI	Supervisory control system and fiber-optic installation	1	\$796,798	\$796,798
LII	Access Bridge	82	\$5,337	\$437,649
LIII	Heliostat Wireless controller (w/o battery and PV)	30,000	\$94.72	\$2,841,600
Total:				\$4,376,047
				\$5.40 /m <sup>2</sup>

### 3 Rapid Calibration System (Tasks 3, 6, and 9)

The state-of-the-art heliostat tracking calibration requires taking a single heliostat off the receiver and pointing it at a calibration target in a continuous calibration cycle throughout the year. The time required to initially calibrate the solar field followed by the long interval between recalibrations is a drawback for smaller scale heliostats where the number of heliostats in a field is 5-6x higher than 140m<sup>2</sup> large heliostats. In Task 3 a Rapid Calibration System (RCS) was developed aided by a numerical RayCasting software program. The RCS is a multiscope photometry method where images of the heliostat field are simultaneously taken from spatially separated cameras surrounding the receiver. These images are used to estimate the location of a heliostat’s reflected sun image. Bench-scale testing under Task 3 in BP1 was unable to meet the target accuracy of 0.5 mrad, and bench-scale testing continued into Task 6 and 9 within BP2 and BP3, respectively. Midway into BP3, a new centroid calculation algorithm was developed, and bench-scale testing is now showing accuracy levels below the 0.5 mrad target.

*Table 64 Rapid Calibration System Final Deliverable*

Milestone Number and Title	Metric	Success Value	Measured Value	Support Data
<b>FD-5</b> Validation of feasibility through mock-up testing outdoors	Error detection sensitivity	≤ 0.5mrad	0.54 mrad	Page 97
	Practical calibration rate	≥ 1000 heliostats/day	Scalable to full field per day.	Page 98
	Operable throughout range of typical solar field layouts and heliostat orientations	100% of heliostats can be measured to within ≤0.5mrad error detection any day of year	Conceptually yes.	Page 98
	Compatible with surround receiver	Yes	Yes	Page 98

#### 3.1 Analytical Model

A detailed ray casting simulation model was developed to analytically simulate the images captured by the cameras mounted around the receiver. This tool casts rays from each pixel in the camera array through the camera’s pinhole to the field, determines what rays intercept either heliostats or the ground and then by Snell’s Law of reflection determines if that pixel ray which intercepts a heliostat sees either the sky or the sun disk with circumsolar radiation.

#### 3.2 RCS overall design

The RCS utilizes a group of four cameras at or near the receiver looking back toward the heliostat field and capturing images of the sun/sky as seen in each heliostat mirror surface. The position of the four cameras shown in Figure 50 is known relative to the

receiver area they surround. The cameras' images are analyzed to determine the brightness of the heliostat's surface within each camera array's field of view (FOV). The annular region surrounding the sun produces diffuse radiation that gradually diminishes with distance from the sun's disk. It is the reflection of this diffuse radiation that is captured by each of the four cameras and used to determine the center of the heliostat's reflected image on the target. Figure 50 presents the simulated camera images using the ray casting model.

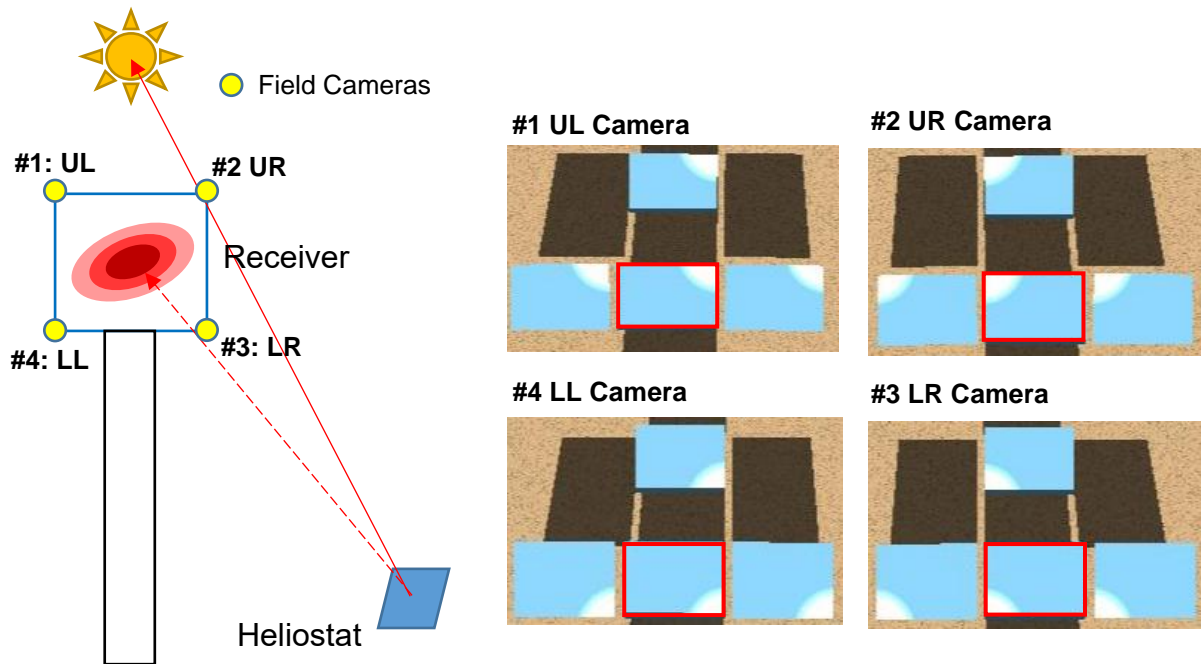


Figure 50 Simulated images taken from RCS cameras

### 3.2.1 Centroid Algorithm 1: Pixel Intensity Gradient Vector

The original centroid algorithm was developed and refined starting in BP1 through mid BP3. First, a pixel intensity vector field and its average vector is determined. When transformed to the global coordinate system of the receiver/cameras, the intersections of these intensity average vectors ultimately yield a location for the sun image centroid on the receiver. The analytical model shows that this method has the potential to hit the 0.5 mrad accuracy target.

### 3.2.2 Centroid Algorithm 2: Total Intensity Weighted Average

In mid BP3, a new approach was developed where the total image intensity is used to estimate the centroid location. This approach is based on work done by Google directed at developing a closed-loop heliostat tracking control [10]. The relative total brightness of the heliostat as seen by each of the four cameras is different depending on the location of the image's centroid. Spatial interpolation using the equation in Figure 51 between these total intensities estimates the centroid. Figure 51 also shows actual images of the test mirror as seen by the four cameras during bench scale testing.



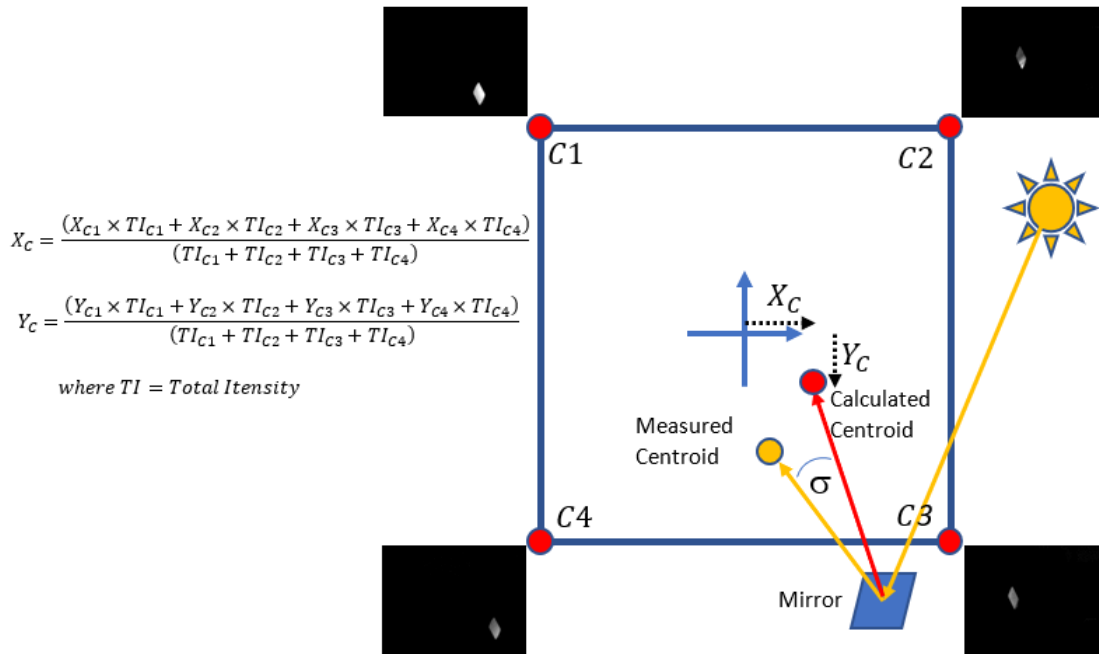


Figure 51 Total intensity weighted average formulation and example images of mirror from cameras

### 3.3 Bench scale testing

The following details the bench scale testing performed with both centroid algorithms.

#### 3.3.1 Pixel Intensity Gradient Vector

A bench scale outdoor test was built in BP1 using the Pixel Intensity Gradient Vector centroid algorithm. Centroid accuracy was poor in BP1, and testing was kept at the bench scale level in BP2 with the goal of hitting the 0.5 mrad accuracy target. Accuracy improved in BP2 due to refinement in the centroid algorithm and image processing, but centroid accuracy was never consistently better than ~2.0 mrad.

#### 3.3.2 Total Intensity Weighted Average

Results from several days of testing in BP3 are shown in Figure 52. Over the course of testing, the image location was moved around the target covering all four quadrants. After filtering out data for windy time periods, the average error between measured and calculated centroids = 0.54 mrad, very close to the 0.5 mrad goal.

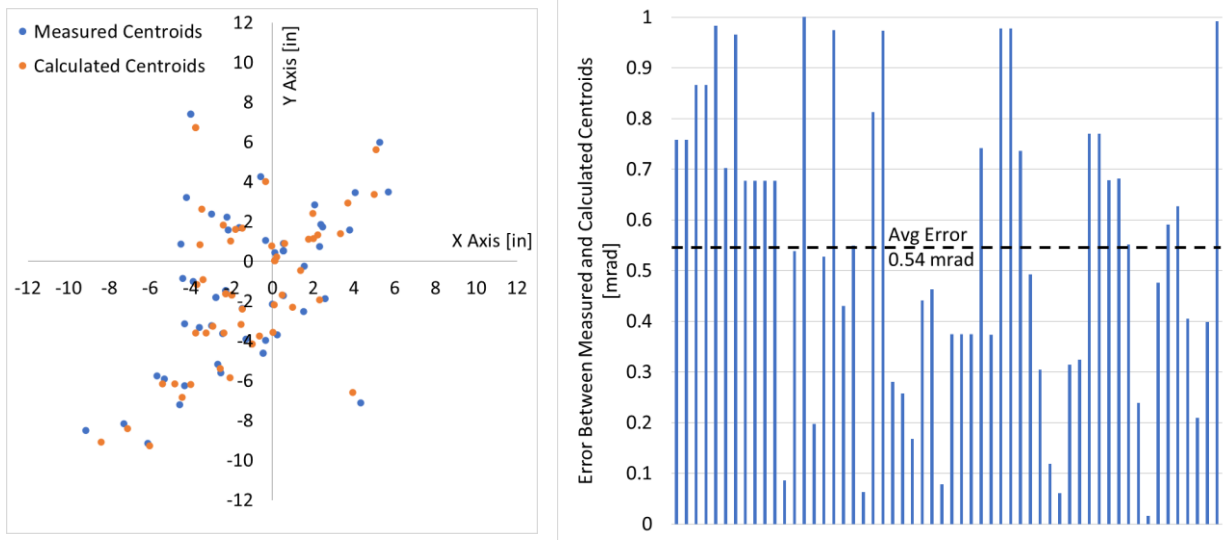


Figure 52 X-Y Position of Measured and Calculated Centroid Pairs with Varying Image Locations. (left), Corresponding Centroid Error with Higher Wind speed Datapoint Removed (right)

### 3.4 Commercialization

At commercial scale, there will be multiple camera arrays (i.e. 1 array = 4 cameras) where each array's field of view covers a specific portion of the heliostat field. The RCS is compatible with cavity and surround external receivers as the field cameras may be mounted above and below the receiver or even integrated into the receiver absorbing surface itself. These cameras are of a pinhole design which protects the sensitive CCD arrays from the high solar flux, but active cooling will still likely be required.

#### 3.4.1 Next Steps

The following identifies issues/steps that need to be addressed with scale-up to a full heliostat and eventually to a commercial solar field installation.

- Protecting cameras from high flux.
- Identifying cameras with auto gain and auto aperture adjustment capabilities.
- Define the minimum required image size of any one heliostat within FOV.
  - This determines the number of camera arrays for full field.
- Heliostat identification using actual solar field images.
  - This should be straightforward with image analysis and field installation maps.
- Assessing effects of image movement due to wind, tracking motion.
  - If an issue, develop an approach to handle.
- Assessing impact of clouds on calibration, can RCS be performed under slightly overcast or passing cloud conditions?
- Can closed-loop or hybrid open/closed-loop tracking be possible with the RCS?

## Significant Accomplishments and Conclusions

The Drop-C project has delivered the low-cost SunRing heliostat which progressed from a conceptual design to a nearly commercial ready product. Component level and full-scale heliostat testing has proven the soundness of the SunRing's novel design. Unforeseen mirror slope error in the facets and industrialization of the azimuth drive pinion remain the only technical barriers to overcome before commercialization. With an installed cost of \$96.3/m<sup>2</sup>, the SunRing is 20-40% lower in cost than the commercial competition. Future developments will improve the competitive position of the SunRing through identified cost saving azimuth drive design changes and optical performance improvements with additional facet support members.

In addition to the SunRing heliostat design, large scale testing of the wireless mesh network has proven its technical and economic feasibility. Bench scale testing of the Rapid Calibration System has shown its ability in measuring centroids with 0.54 mrad accuracy.

## Inventions, Patents, Publications, and Other Results

The Drop-C project has resulted in the following patent which protects the SunRing's azimuth drive and lower support structure:

- N. Stegall, K. Kattke, R. Sommers, Systems and Methods for Mounting a Helisotat, WIPO Patent No. WO 2021/231453, Nov. 18, 2021.

The Drop-C project has been presented at every SolarPaces conference through both poster and oral sessions from 2018-2021 with the following:

- SolarPaces 2018: poster – *Drop-C: The Drop-In, Ring-of-Power Heliostat*
- SolarPaces 2019: poster – *Drop-C: The Drop-In, Ring-of-Power Heliostat. Azimuth Drive and Foundation Testing and Selection*
- SolarPaces 2020: oral – *Drop-C Heliostat Full-Scale Performance Testing*
- SolarPaces 2021: poster – *SunRing™ Heliostat Refinement and Performance Testing*

## Path Forward

Solar Dynamics is actively looking for investment in the SunRing heliostat to move it from its current TRL of 5 to a bankable project with a TRL of 7. The overall pathway and investment needed is provided in Section 1.10.2. Additionally, there are two main design enhancements which have been identified for the azimuth drive carriage and the mirror support structure. Proposals to active FOAs have been submitted regarding these improvements.

## References

- [1] A. Kribus, I. Vishnevetsky, A. Yogeve, T. Rubinov, Closed loop control for heliostats, *Energy*, Vol. 29, p 905-913, 2004.
- [2] A. Pfahl, J. Coventry, M. Roger, F. Wolfertstetter, J.P. Vasquez-Arango, F. Gross, M. Arjomandi, P. Schwarzbozl, M. Geiger, P. Liedke, Progress in heliostat development, *Solar Energy*, Vol. 152, p 3-37, 2017.
- [3] A. Pfahl, J. Rheinlander, A. Krause, R. Buck, S. Giuliano, J. Hertel, K. Blume, T. Schlichting, N. Janotte, First lay-down heliostat with monolithic mirror-panel, closed loop control, and cleaning system, *SolarPaces 2018*.
- [4] A. Pfahl, M. Randt, S. Kubisch, C. Holze, H. Bruggen, Autonomous Light-Weight Heliostat with Rim Drives, *SolarPaces 2012*.
- [5] Award DE-EE0003596, Baseload Nitrate Salt Central Receiver Power Plant Design, Research Performance Progress Report. Recipient: Abengoa Solar LLC
- [6] Award DE-EE0007121, ATLAS: Advanced Trough with Low-cost System-architecture. Recipient: Solar Dynamics LLC
- [7] C. Corsi, V. Grigoriev, M. Blanco, Far-field optimization of heliostat shape and spacings, *Asia-Pacific Solar Research Conference 2015*.
- [8] C. Ho, D. Griffith, J. Sment, A. Moya, J. Christian, J. Yuan, P. Hunter, Dynamic Testing and Analysis of Heliostats to Evaluate Impacts of Wind on Optical Performance and Structural Fatigue, *SolarPaces 2021*, SAND2021-8380C.
- [9] E. Toister. Flexible Assembly Solar Technology (FAST) Final Technical Report. United States: N. p., 2014. <https://www.osti.gov/servlets/purl/1167013>.
- [10] J. Fitch, et. al., Heliostat Control System Using Cameras, United States Patent Application Publication No. US 2011/0120448 A1, May 26,2011
- [11] J.A. Peterka, R.G. Derickson, Wind Load Design Methods for Ground-Based Heliostats and Parabolic Dish Collectors, SAND92-7009, 1992.
- [12] K. Strobel, D. Banks, Effects of vortex shedding in arrays of long inclined flat plates and ramifications for ground-mounted photovoltaic arrays, *Journal of Wind Engineering and Industrial Aerodynamic*. Vol. 113, p 146-149, 2014.
- [13] L. Crespo, F. Ramos, F. Martinez, Questions and answers on solar central receiver plan design by NSPOC. *SolarPaces 2011*.
- [14] M. Collins, M. Rae, M. McKinnon, M. Dunn, J. Oorloff, Camera array concept for simultaneous calibration of multiple heliostats, *SolarPaces 2018*.
- [15] N. Goldberg, G. Kroyzer, R. Hayut, J. Schwarzbach, A. Eitan, S. Pekarsky, Embedding a visual range camera in a solar receiver, *SolarPaces 2014*
- [16] N. Stegall, K. Kattke, R. Sommers, Systems and Methods for Mounting a Heliostat, WIPO Patent No. WO 2021/231453, Nov. 18, 2021.

- [17] Roger M., SolarPACES Guideline for Heliostat Performance Testing, Draft Version 0.991. August 8<sup>th</sup> 2018.
- [18] S. Unterschütz, Methodologies and Protocols for Wireless Communication in Large-Scale, Dense Mesh Networks, Hamburg University of Technology, PhD Thesis, 2014.